Coherent Ion Transport in a Multi-electrode Trap Array

by

Ryan Bowler

B.S., Physics, University of Washington, 2008

B.A., Mathematics, University of Washington, 2008

A thesis submitted to the

Faculty of the Graduate School of the

University of Colorado in partial fulfillment

of the requirements for the degree of

Doctor of Philosophy

Department of Physics

2015

This thesis entitled:
Coherent Ion Transport in a Multi-electrode Trap Array
written by Ryan Bowler
has been approved for the Department of Physics

David J. Wineland

Cindy Regal

Date

The final copy of this thesis has been examined by the signatories, and we find that both the content and the form meet acceptable presentation standards of scholarly work in the above mentioned discipline.

Bowler, Ryan (Ph.D., Physics)

Coherent Ion Transport in a Multi-electrode Trap Array

Thesis directed by Dr. David J. Wineland

Quantum information processors are predicted to enable a significant speedup in solving certain classes of problems compared to their classical counterparts. For one scheme of a processor implementation, required elements include qubits with long coherence times, laser-induced universal gates, information transport, and motional-state initialization using a second coolant ion species. Techniques described in this thesis include the use of a multiple electrode segmented trap, wherein information transport is achieved through the transport of qubit ions between spatially distinct locations. While experiment timescales had previously been dominated by ion transport and re-cooling of motional states, I have achieved transport and separation of qubit ions on timescales comparable to quantum logic gates. This work has been extended to achieve fast transport of qubit and coolant two-species ion chains. The developed techniques for ion transport result in low motional excitations, reducing the need for re-initialization of ion motional states. This can enable significant improvement in the operation time of an ion-based quantum information processor.

Dedication

This thesis is dedicated to my parents.

Acknowledgements

The work described in this thesis is the culmination of years of work carried out with the support of many people. It is impossible to give a special thanks to each person who had played an important role during my time in graduate school, though I trust that many people know that they've played an important role even if not mentioned here. When I had first joined the ion storage group, I had been given the great opportunity to work with John Jost, David Hanneke, and Jonathan Home, from whom I had learned a great deal about physics and operating complex experiments. Didi Leibfried has an enormous enthusiasm for the physics going on in the ion storage group, and I've greatly appreciated his enthusiasm for the experiments I had worked on during my time with the group. I have also had the privilege of working closely with John Gaebler, Ting Rei Tan, and Yiheng Lin, who have all had diverse and useful input over the years. I consider the support I've had from many friends invaluable during graduate school, and I'd like to thank Geoff White, Paul Pham, Adam Wagner, Nathan Morrison, Cecily Nicewicz, and Justin Kneip for sustained support over the years through the tough ups and downs. Most importantly, I'd like to thank my adviser Dave Wineland, who has a vast amount of knowledge and experience in research. His guidance is a driving force for the preeminent research I've had the privilege of being involved in during my time with the group.

Contents

Chapter

1 Introduction 1

2 ^{9}Be$^+$ Qubit 7

2.1 ^{9}Be$^+$Atomic Structure 7

2.2 Hyperfine Structure and Magnetic Fields 8

2.3 Doppler Cooling 11

2.4 State Initialization 15

2.5 Stimulated Raman Transitions 18

2.6 State Detection 23

3 Motional Dynamics of Trapped Ions 26

3.1 Linear RF Paul Trap 27

3.1.1 Idealized System 27

3.1.2 Nulling Micromotion 32

3.1.3 Normal Modes of Multiple Trapped Ions 32

3.1.4 Harmonic Oscillator States 35

3.1.5 Re-ordering Ions 37

3.2 Non-classical States of Motion 38

3.2.1 Coherent Distribution 38

3.2.2 Thermal Distribution 40

3.2.3 Squeezed Distribution 42
3.3 Laser-Motion Interactions 43
3.3.1 Motional-Sideband Laser Interactions 43
3.3.2 Interactions in the Presence of Multiple Normal Modes 46
3.3.3 Doppler Cooling on Normal Modes 48
3.3.4 Sideband Cooling of Normal Modes 49
3.4 Analyzing Motional States 51
3.5 Sympathetic Cooling with ^{24}Mg^{+} and ^{25}Mg^{+} 54

4 Apparatus 56
4.1 Multiple Electrode Wafer Trap 57
4.2 Trap Geometries 58
4.2.1 Quantum Logic Trap 58
4.2.2 X-junction Trap 63
4.3 Containment System 67
4.3.1 Vacuum Components 67
4.3.2 Loading Ions 69
4.3.3 Imaging System 70
4.3.4 Magnetic Field Coils 71
4.4 Lasers 71
4.4.1 ^{9}Be^{+} Blue Doppler Beam Line 74
4.4.2 ^{9}Be^{+} Red Doppler Beam Line 75
4.4.3 ^{9}Be^{+} Raman Beam Line 76
4.4.4 ^{25}Mg^{+} Doppler Beam Line 76

5 Experiment Control 80
5.1 Introduction to FPGAs 81
5.2 Experiment-Control FPGA 82

5.3 Arbitrary Waveform Generator 84
    5.3.1 Hardware 86
    5.3.2 User Control 89
    5.3.3 Memory Storage 91
    5.3.4 Possible Future Implementations 94
    5.3.5 Experimental Implementations 97

6 Coherent Transport Dynamics of Trapped Ions 102
6.1 Adiabatic Ion Transport 103
6.2 Coherently-driven Ion Transport 106
6.3 Transport of ^{9}Be$^+$ Experiments and Results 108
6.4 Ion Separation 112
6.5 Separation of Two ^{9}Be$^+$Experiments and Results 115

7 Optimization of Multi-species Ion Transport via Feedback on Quantum Motion 121
7.1 Methods for Optimizing Two-Species Transport 123
7.2 Transport of a Two-Species Ion Chain Experiments and Results 125

8 Conclusions and Outlook 132

Bibliography 135

Appendix

A Transport Gate 141

B AWG Spec Sheets 145

Tables

Table

3.1 Normal modes for a ^{9}Be$^+$-^{25}Mg$^+$ linear ion crystal 36
3.2 Doppler-cooling limits $\bar{n}_{limit}$ for each axis for ^{9}Be$^+$ 49

4.1 UV and visible wavelengths for the ^{9}Be$^+$ lasers 72

5.1 Commands sent from the control computer to the AWG 92

7.1 Normal modes for a ^{9}Be$^+$-^{24}Mg$^+$ chain and the Doppler cooling limits $\bar{n}_{limit}$ 126
7.2 Normal modes for a ^{9}Be$^+$-^{25}Mg$^+$ chain and the Doppler cooling limits $\bar{n}_{limit}$ 129

Figures

Figure

1.1 Drawing of a wafer ion trap 3

1.2 Pie chart for SU(4) time-distribution 4

1.3 Pie chart for Randomized Benchmarking time-distribution 5

2.1 Diagram for atomic structure of ^{9}Be$^+$ 9

2.2 Zeeman shift for the $S_{1/2}$ hyperfine states 12

2.3 Diagram for atomic structure of ^{9}Be$^+$ with state preparation beams 16

2.4 Raman transition diagram 19

2.5 Detection histogram 25

3.1 An idealized linear RF Paul trap 28

3.2 Detection in the presence of micromotion 33

3.3 Diagram for a coherent state of motion 39

3.4 Diagram for a thermal state of motion 41

3.5 Diagram for a squeezed state of motion 42

3.6 Raman beam alignment for beams interacting with normal modes along the trap axis 44

3.7 Types of Raman sideband transitions between two spin levels 47

3.8 Diagram of the Raman sideband cooling process on a single mode of motion 50

3.9 Plot of Rabi π-times and rates for different number states 51

3.10 Rabi flopping trace for a thermal state of motion for a single ^{9}Be$^+$ 52

3.11 Rabi flopping trace for a thermal state of motion for a ^{9}Be^{+}-^{25}Mg^{+} ion pair 53

4.1 Photograph of the quantum logic trap 59
4.2 A model of the electrodes for the quantum logic trap 61
4.3 A close-up model of the quantum logic trap illustrating where ions would be trapped . 61
4.4 Schematic of the side view of the quantum logic trap 62
4.5 Photograph of the X-junction trap 64
4.6 A model of the electrodes for the X-junction trap 66
4.7 Diagram of the vacuum system 68
4.8 Images collected from a CCD camera imaging fluorescence from ^{25}Mg^{+} and ^{9}Be^{+} . 70
4.9 Diagram for the relative alignment of the ion imaging system, magnetic field coils, incident laser light, and the ion trap 73
4.10 ^{9}Be^{+} Blue Doppler beam line 77
4.11 ^{9}Be^{+} Red Doppler beam line 77
4.12 ^{9}Be^{+} Raman beam lines 78
4.13 ^{25}Mg^{+} Doppler beam line 79

5.1 Flow diagram overview of the AWG 86
5.2 Photograph of the AWG master board 88
5.3 Diagram of the Simple Dual-Port RAM input and output interface 92
5.4 Example waveform with filter compensation 98
5.5 Pulse shaping of a microwave signal using the AWG to specify the profile 100

6.1 Schematic for the diagonally-opposite DC electrodes of the quantum logic trap 108
6.2 Rabi flopping trace on the MAS and MSS after transport from zone A to B 109
6.3 Rabi flopping trace on the MAS following transport in which $\alpha(t_T) \neq 0$ 110
6.4 Fixed MSS drive time t after round-trip transport for different wait times in zone B . . 111
6.5 Ramsey-type interference experiment comparing contrast with and without transport 113

6.6 Calculation of $\frac{1}{\omega^2}\frac{d\omega}{dt}$ during the separation waveform 116

6.7 Change in ion position and normal mode frequency during separation 117

6.8 Ion fluorescence in zone A as a function of the offset potential during separation . . . 119

6.9 Rabi flopping traces of the MAS of the ion in zone A and zone B after separation . . 120

7.1 Schematic for the diagonally-opposite DC electrodes of the quantum logic trap 125

7.2 Rabi flopping traces on the MAS for ^{9}Be$^+$-^{24}Mg$^+$ following the optimization procedure 128

7.3 Schematic for the diagonally-opposite DC electrodes of the X-junction trap 128

7.4 Rabi flopping traces on the MAS for ^{9}Be$^+$-^{25}Mg$^+$ following the optimization procedure 131

B.1 AWG Spec Sheet 1 146

B.2 AWG Spec Sheet 2 147

B.3 AWG Spec Sheet 3 148

B.4 AWG Spec Sheet 4 149

B.5 AWG Spec Sheet 5 150

Chapter 1

Introduction

Quantum information processing (QIP) takes advantage of quantum mechanics to perform certain computations more efficiently than currently possible on a classical computer. Some examples are to simulate other quantum systems of interest [1, 2], factoring large numbers [3], or searching unsorted databases [4]. Typically, the basic unit of quantum logic is the quantum bit, or "qubit," which comprises two levels of any quantum system. Trapped atomic-ions are a promising basis for QIP; our ion-based qubit comprises two atomic hyperfine states of the ion, and "quantum logic" is performed by a sequence of laser or microwave pulses to drive transitions between the qubit states [5, 6]. The building blocks for QIP include a universal set of operations for quantum logic, transport of information about the processor, and qubits that can be prepared in an initial state, can be reliably measured, and have a long coherence time.

For large-scale QIP based on trapped ions, information transport could be achieved by designing an ion trap with an array of interconnected trap zones, where quantum information is transported by confining the ions in potential wells that are moved between trap zones [6, 7, 8]. The ion trap can be designed with many electrodes, where potentials on the electrodes form three-dimensional harmonic wells via a combination of static and oscillating electric fields, and an additional time-varying component to electrode potentials can transport the ions between zones. The necessary transport protocols include the separation of ions from a shared trap, combination of selected ions into a single trap, and transport of ions through junctions for re-ordering. Re-ordering ions and being able to combine them into a single trap is necessary for entangling any pair of qubits.

The qubit, with states labeled $|0\rangle$ and $|1\rangle$, can exist in the states $|0\rangle$, $|1\rangle$, or any superposition of the two states due to the quantum nature of the qubit system. Using the notation that the state for two qubits Q_1 and Q_2 is written as $|Q_1 Q_2\rangle$, then any two-qubit pure state can be written as

$$\Psi = c_{00}|00\rangle + c_{01}|01\rangle + c_{10}|10\rangle + c_{11}|11\rangle, \tag{1.0.1}$$

with the normalization constraint $\sum |c_{ij}|^2 = 1$ on the four complex coefficients that describe the state. This makes many-qubit systems far more interesting than classical-bit systems. A key element for quantum information that has no analog in the classical world is the entangled state. An example of such a state is given by

$$\Psi = \frac{1}{\sqrt{2}}(|00\rangle + |11\rangle), \tag{1.0.2}$$

which has the key characteristic that one qubit state is not independent or "separable" from the other.

The shared vibrational motion between multiple ions in a single trap zone can act as an “information bus” to entangle two ions [5]. By using laser beam configurations that can drive the qubit states and the ions’ shared harmonic motion, it is possible to engineer qubit-motion entanglement and in turn use the shared motion to entangle two qubits [5, 9, 10, 11]. The success rate, or “fidelity,” of the entangling gate is typically highest when the ions start in their ground state of vibrational motion, necessitating laser cooling to the near-ground state of motion in the trap. Ambient heating, motional excitations due to fluctuating stray electric fields, is an important source of decoherence for gates that use the shared motion as an information bus. In our scalable QIP architecture, entanglement between any two qubit ions requires separating, transporting, and combining ions in shared trap zones, which can cause additional motional excitations. Laser cooling can return the ions’ motion to the ground state, but if performed on the qubit ions, cooling disrupts the qubit state. To get around this, another ion species with very different laser wavelengths for cooling is trapped along with the qubit ions. Laser cooling on this “coolant ion” can cool the shared motion for all the

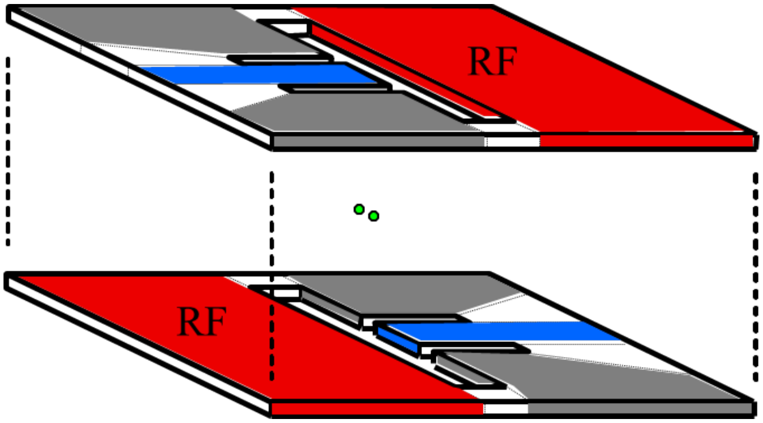

Figure 1.1: Wafer trap geometry. Ions are confined at the center between the wafers, where the green circles denote confined ions (not to scale). The ion trap is formed by static potentials on electrodes (grey and blue portions) and oscillating potentials on "RF" electrodes (red portions) to form a three-dimensional harmonic oscillator potential. Slots in the wafers allow laser-access to the ions. By fabricating many similar electrodes, a large array of trap zones can be created.

ions, a technique known as "sympathetic cooling," without disrupting qubit states.

There are several trap construction methods for this QIP scheme that have been used, and to-date there are two principal methods. The electrodes can be manufactured onto insulating wafers (as depicted in Fig. 1.1), where the electrodes are made from depositing conducting material onto a wafer made from a laser-machined insulator [12, 13, 14, 15]. The minimum size for electrode features is set by the laser beam's minimum focus size, and typical sizes have electrode widths of $\sim 100\mu$m. Another approach is through a lithographic process to produce the electrodes on a single planar surface, which allows smaller feature sizes down to $\sim 30\mu$m size scales [16, 17, 18]. For large-scale quantum information processing, development of larger trap architectures is necessary, such as those in Refs. [13, 18, 19, 15, 20, 21]. While the lithographic process has become more popular, many of the existing demonstrations of scalable trap architectures have been carried out in wafer traps.

Transport and separation of ions in a wafer trap was first demonstrated in Ref. [12], where it was shown that ion transport can be achieved with little motional excitation if performed adiabatically (that is, in a time much longer than the ion trap's vibrational period) and that the separation of

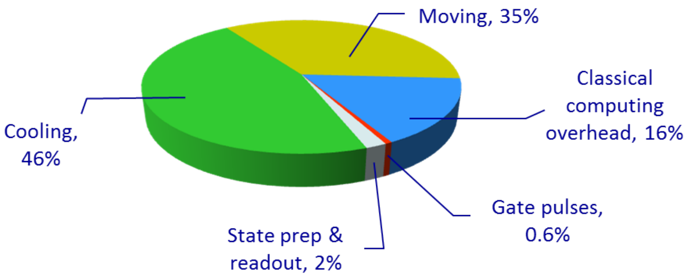

Figure 1.2: Time-distribution between various processes in Ref. [27]. Computer control includes preparing electronics for the experiment, laser control includes preparing the sequencing of laser pulses, and the largest portions are due to transport and the initialization of the motional states through laser cooling.

two ions from a single trap can also be performed. For work in Ref. [22], a trap was designed with electrode dimensions roughly half the size of those in Ref. [12], and greater control over ion separation was achieved, attributed to a smaller size-scale of the electrodes. Work reported in Ref. [23] showed the ability to transport ions on timescales comparable to quantum logic, but with the trade-off of large motional excitations. Transport experiments have also been carried out in a wafer trap to show reliable, adiabatic transport through a junction with low motional excitations [15], which is important for re-ordering ions. Excitations due to transport were largely attributed to electric field noise from electrode surfaces [24, 25, 26] and imperfect transport waveforms due to slow electronics for the transport potentials.

Demonstrations of our approach to scalable QIP method-sets with trapped ions were reported in Refs. [29, 27, 28] using ^{9}Be^{+} as the qubit ion and ^{24}Mg^{+} as the coolant ion. These demonstrations combined all of the building blocks of ion-based QIP, including long qubit coherence times, transporting ions between zones, ground-state cooling with another ion species, and laser-driven entanglement using the shared harmonic motion for universal logic gate sets. However, these experiments involved ion transport and laser cooling on long timescales. While each quantum logic operation typically took $\sim 10\mu$s, ion transport required hundreds of microseconds to remain in the adiabatic regime to suppress unwanted excitations of the ions' motion. The distribution for the durations of various processes in Ref. [27] is shown in Fig. 1.2 and the distribution for the durations

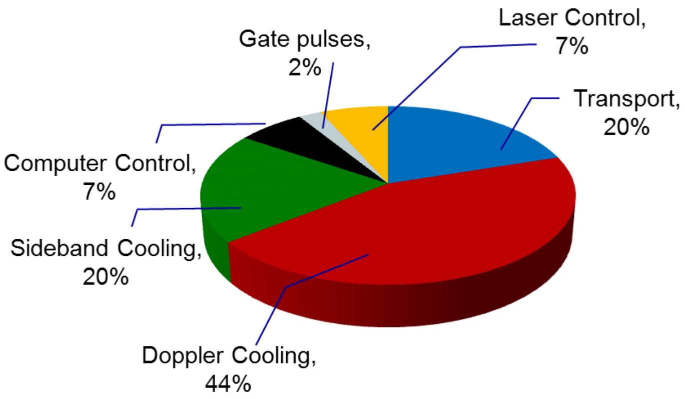

Figure 1.3: Time-distribution between various processes in Ref. [28]. The distribution is very similar to that for Ref. [27], where the largest portions are due to transport and cooling.

of various processes in Ref. [28] is shown in in Fig. 1.3. The timescales for QIP are dominated by laser-cooling the harmonic motion after transport, followed by the ion transport durations. A demonstration of an error correction algorithm, which is conditioned on the detection of errors, has also been carried out in this multi-electrode scheme with similar timescale discrepancies [30]. The timescale discrepancies between transport/cooling and quantum logic imposes a temporal bottleneck for large-scale quantum information processing. Therefore, to achieve large-scale QIP with trapped ions, transport must be performed on a timescale comparable to quantum logic with little-to-no motional excitations.

The work described in this thesis achieved orders-of-magnitude improvements in ion transport, characterized both by transport speeds on timescales similar to quantum logic gates and highly-mitigated excitations in ion motion during transport. This thesis describes experiments transporting and separating ^{9}Be$^+$ qubit ions and transporting qubit and coolant ion pairs of ^{9}Be$^+$-^{24}Mg$^+$ or ^{9}Be$^+$-^{25}Mg$^+$. To begin with, Chapter 2 discusses the ^{9}Be$^+$ qubit and the ion-laser interactions with the qubit states. Then, Chapter 3 discusses the motional dynamics of trapped ions, including the laser interactions with the harmonic motion of the ions and relevant laser interactions with the coolant ions. Chapter 4 discusses the apparatus for the experiments, including the ion traps and the laser systems used during the experiments. Chapter 5 describes the electronics used to control the experimental sequences and the electronics for controlling ion transport. In Chapter 6, I describe the theory and experiments for coherent ion transport with qubit ions on timescales comparable to quantum logic. This chapter also discusses the theory and experiments for separating a pair of qubit ions into distinct trap zones. In Chapter 7, I describe the experiments for applying an optimization routine for transporting qubit and coolant ion pairs on quantum logic timescales. I close with some discussion for future directions to further improve transport during QIP operations.

Chapter 2

^{9}Be$^+$ Qubit

A quantum information processor requires good quantum bits, or qubits, which implies that they have long coherence times for information storage over the duration of processor operations. A qubit also must be able to be prepared in a well-defined initial state, have a good method set for manipulating the qubit states and good measurement efficiency. A scalable processor requires a universal logic gate set and the ability to transport information about the processor. A qubit comprises two levels of any quantum system, which for this work comprises two electronic states of the ^{9}Be$^+$ ion. This chapter provides a description of the qubit states and how we manipulate them for our approach to quantum information processing. While ^{9}Be$^+$ ions have a diverse internal electronic structure, our use of lasers and microwaves allow us to isolate transitions between specific two-level subsets to carry out our experimental operations for qubit manipulations. Additional laser control is used for state initialization and detection of the qubit state. In this chapter, I'll discuss the energy levels in ^{9}Be$^+$ and motivate the choice of two specific hyperfine sublevels of the ^{9}Be$^+$ ground state as our qubit manifold. Then I'll describe the laser- and microwave-interactions to control and manipulate the internal states and laser-cooling of the ^{9}Be$^+$ qubit ion.

2.1 ^{9}Be$^+$Atomic Structure

Beryllium is the lightest alkali-earth metal, and when ionized, it becomes an alkali-like atom with a single outer electron. The single outer-electron configuration is a relatively convenient structure, and the ^{9}Be$^+$ atomic structure is well-studied. The relevant atomic structure for the work in this thesis is diagrammed in Fig. 2.1. The ground state level is the 2s$^2S_{1/2}$ state, which is split into two hyperfine levels $F=1$ and $F=2$ (which arises from the coupling of outer-electron angular momentum J to the nuclear spin $I=3/2$ with total angular momentum $F=I+J$ [31]), where the hyperfine states have ~1.25 GHz splitting. For the work in this thesis, the principle number $n=2$ and electron spin $S=1/2$ will not change and thus will be omitted in the discussion below. Our qubit comprises a pair of hyperfine states in the $S_{1/2}$ manifold (the upper of which has a radiative decay time of about 10^{15} s [6]), which we describe in the total angular momentum $|F,m_F\rangle$ basis.

The other relevant states are the lowest excited orbital angular momentum states, two P states, split by fine structure (the coupling of outer-electron spin to its orbit angular momenta [31]). The $P_{1/2}$ and $P_{3/2}$ are split by ~ 197 GHz [32], and both states are coupled to the S states with ~313 nm laser light. The P states have a linewidth of $\Gamma \simeq 2\pi \times 19.4$ MHz. The $P_{1/2}$ state has a hyperfine splitting of 237 MHz [32], and the higher $P_{3/2}$ state has a very small <1 MHz hyperfine splitting which we neglect in our experiments.

2.2 Hyperfine Structure and Magnetic Fields

In the experiments, we apply an external magnetic field to our ions. This provides a quantization axis and splits the hyperfine structure into magnetic sublevels by the Zeeman effect. The Hamiltonian including both the hyperfine interaction and the magnetic field interaction is

$$H = hAI\cdot J + \mu_B(g_J J + g_I I)\cdot B, \tag{2.2.1}$$

where h is Planck's constant, A is a hyperfine constant in Hz (for ^{9}Be$^+$ splitting of the $S_{1/2}$ state, A=-625.008837048(10) MHz), μ_B is the Bohr magneton, $g_J = 2.00226206(42)$ and $g_I/g_J = 2.134779853(2)\times 10^{-4}$ give the respective Landé g-factors for electron angular momentum J and nuclear spin I for ^{9}Be$^+$, and B is the externally-applied magnetic field (numbers from Ref. [33]). The direction of B, or $\hat{B}$, sets the spin quantization axis, which for this analysis I choose as the $\hat{z}$-axis.

The first term in Eq. 2.2.1 can be rewritten as

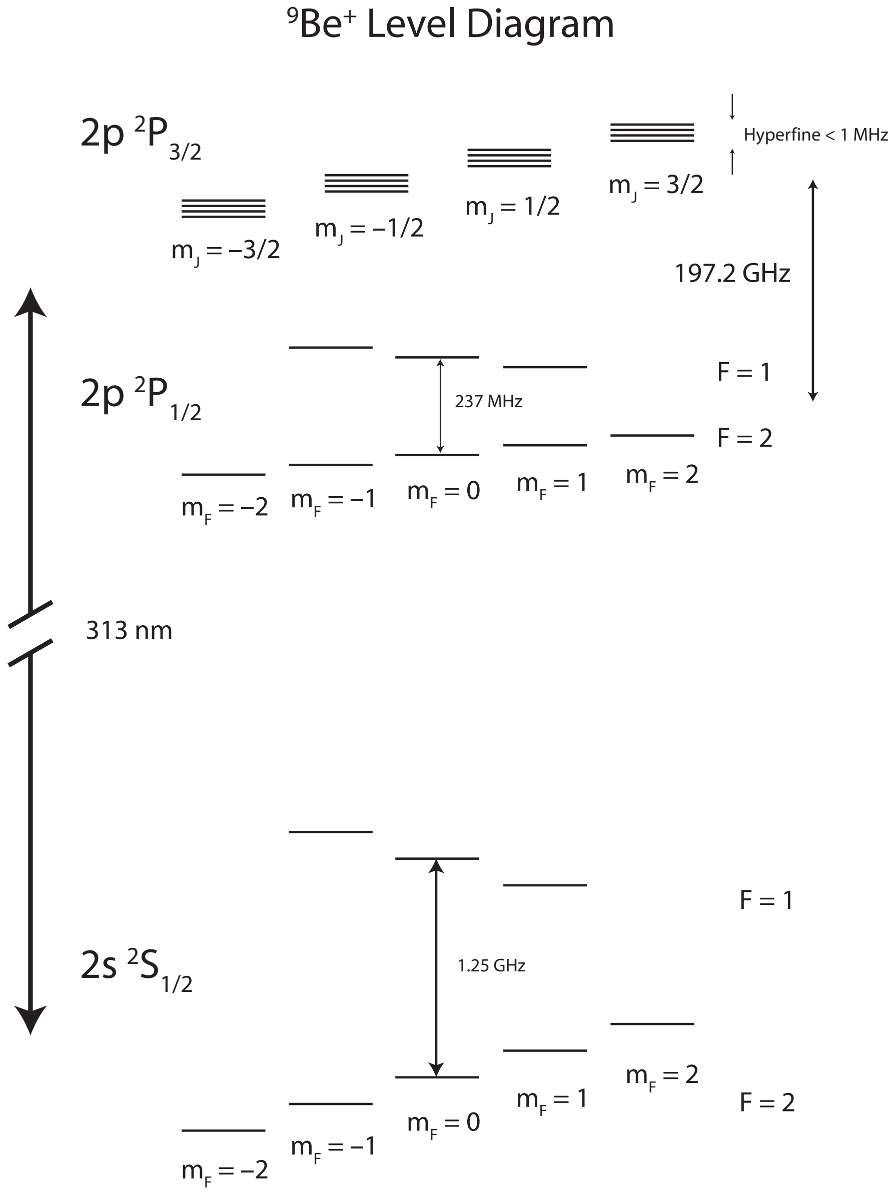
9Be+ Level Diagram
2p 2P3/2
mJ = −3/2
mJ = −1/2
mJ = 1/2
mJ = 3/2
Hyperfine < 1 MHz
197.2 GHz
2p 2P1/2
237 MHz
F = 1
F = 2
mF = −2
mF = −1
mF = 0
mF = 1
mF = 2
313 nm
2s 2S1/2
1.25 GHz
F = 1
F = 2
mF = −2
mF = −1
mF = 0
mF = 1
mF = 2

Figure 2.1: Atomic structure diagram of ^{9}Be$^+$. The hyperfine splitting of the $S_{1/2}$ state is $\sim$1.25 GHz. The fine structure splitting of the P states is $\sim$197.2 GHz and the hyperfine splitting of the $P_{1/2}$ state is 237 MHz while that of the $P_{3/2}$ state is less than 1 MHz. The S to P dipole-allowed transitions are coupled by 313 nm light. Hyperfine sublevels are shown with split m_F sublevels of each F state arising from an external magnetic field.

$$hAI\cdot J = hA(I_zJ_z + \frac{1}{2}I_+J_- + \frac{1}{2}I_-J_+), \tag{2.2.2}$$

where $I_{+/-} = I_x \pm iL_y$ and $J_{+/-} = J_x \pm iJ_y$ operators can be written by the usual raising and lowering operators for angular momentum $L_{+/-}|L,m_L\rangle = \sqrt{L(L+1) - m_L(m_L \pm 1)}|L,m_L \pm 1\rangle$ [31]. The second term in Eq. 2.2.1 can be written as

$$\mu_B B(g_J J_z + g_I I_z). \tag{2.2.3}$$

Solving for the dependence on B can be done by constructing an operator matrix for each m_I and m_J level and solving for the eigenvalues. Grouping terms for the above-diagonals involving I_+ the below-diagonals involving I_- as $I^{\pm}_{m_I}J^{\mp}_{m_J}$ constructs terms for a matrix such that

$$I^{\pm}_{m_I}J^{\mp}_{m_J} = \frac{1}{2}hA\sqrt{I(I+1) - m_I(m_I \pm 1)}\sqrt{J(J+1) - m_J(m_J \mp 1)}. \tag{2.2.4}$$

The terms for the matrix diagonal are

$$D_{m_i,m_j} = hAm_Im_J + \mu_B B(g_j m_J + g_I m_I). \tag{2.2.5}$$

These terms are put into the following matrix for the ^{9}Be$^+$ hyperfine sublevels of the $S_{1/2}$ state.

$$\begin{pmatrix}
D_{\frac{3}{2},\frac{1}{2}} & 0 & 0 & 0 & 0 & 0 & 0 & 0 \\
0 & D_{\frac{1}{2},\frac{1}{2}} & 0 & 0 & I^+_{\frac{1}{2}}J^-_{\frac{1}{2}} & 0 & 0 & 0 \\
0 & 0 & D_{-\frac{1}{2},\frac{1}{2}} & 0 & 0 & I^+_{-\frac{1}{2}}J^-_{\frac{1}{2}} & 0 & 0 \\
0 & 0 & 0 & D_{-\frac{3}{2},\frac{1}{2}} & 0 & 0 & I^+_{-\frac{3}{2}}J^-_{\frac{1}{2}} & 0 \\
0 & I^-_{\frac{3}{2}}J^+_{-\frac{1}{2}} & 0 & 0 & D_{\frac{3}{2},-\frac{1}{2}} & 0 & 0 & 0 \\
0 & 0 & I^-_{\frac{1}{2}}J^+_{-\frac{1}{2}} & 0 & 0 & D_{\frac{1}{2},-\frac{1}{2}} & 0 & 0 \\
0 & 0 & 0 & I^-_{-\frac{1}{2}}J^+_{-\frac{1}{2}} & 0 & 0 & D_{-\frac{1}{2},-\frac{1}{2}} & 0 \\
0 & 0 & 0 & 0 & 0 & 0 & 0 & D_{-\frac{3}{2},-\frac{1}{2}}
\end{pmatrix} \tag{2.2.6}$$

For $J = 1/2$, the eigenstates can be solved analytically, where the analytic solution to the system is referred to as the Breit-Rabi formula. Solving for the eigenvalues of the above matrix yields the magnetic field B-dependence of each hyperfine $m_F = m_I + m_J$ sublevel. The results of diagonalizing the matrix are plotted in Fig. 2.2 for the B-field dependence for each $|F, m_F\rangle$ sublevel; for the rest of this thesis, states labeled $|F, m_F\rangle$ are assumed to be a state in the $S_{1/2}$ manifold.

A key feature of the Zeeman shift is that for certain choices of B, the slope of the Zeeman shift vs. B is the same for certain pairs of $|F, m_F\rangle$ states. This means that certain choices of field B and a corresponding pair of two particular $|F, m_F\rangle$ states can form a qubit that is first-order insensitive to fluctuations from external fields (a "field-insensitive" qubit). The trivial solution for a field-insensitive qubit is the pair $|2,0\rangle \longleftrightarrow |1,0\rangle$ at $B = 0$, but since we need to spectrally resolve the m_F levels, this choice is unsuitable.

There are several pairs of states at non-zero B that form a field-insensitive qubit with spectrally-resolvable m_F levels; there are nine such pairs in all with calculations in Ref. [34], but we have chosen two for the convenient experimental-access in our lab in the intermediate-field regime of the Zeeman shift. The transition $|2,0\rangle \longleftrightarrow |1,1\rangle$ is field-insensitive at $B = 11.945$ mT and was used to demonstrate a qubit coherence time of ~ 15 s [35]. At that magnetic field, $|2,0\rangle \longleftrightarrow |1,1\rangle$ has a qubit splitting of 1207.49584322 MHz. The choice of $|2,1\rangle \longleftrightarrow |1,0\rangle$ is field-insensitive at $B = 11.964$ mT, with a splitting 1207.35280753 MHz, and was used to perform experiments involving the entanglement of two qubits [29, 27, 28] with similar coherence timescales. The $|2,1\rangle \longleftrightarrow |1,0\rangle$ qubit choice was used for the work described in this thesis.

2.3 Doppler Cooling

Working with an ion requires strong spatial localization. Part of this localization comes from Doppler cooling, a laser-light induced process to reduce the average kinetic energy of an ion held in an ion trap. Our ion trap uses a combination of static and time-varying electric fields to confine the ion in an approximately three-dimensional harmonic well (to be discussed in Chapter 3). A review

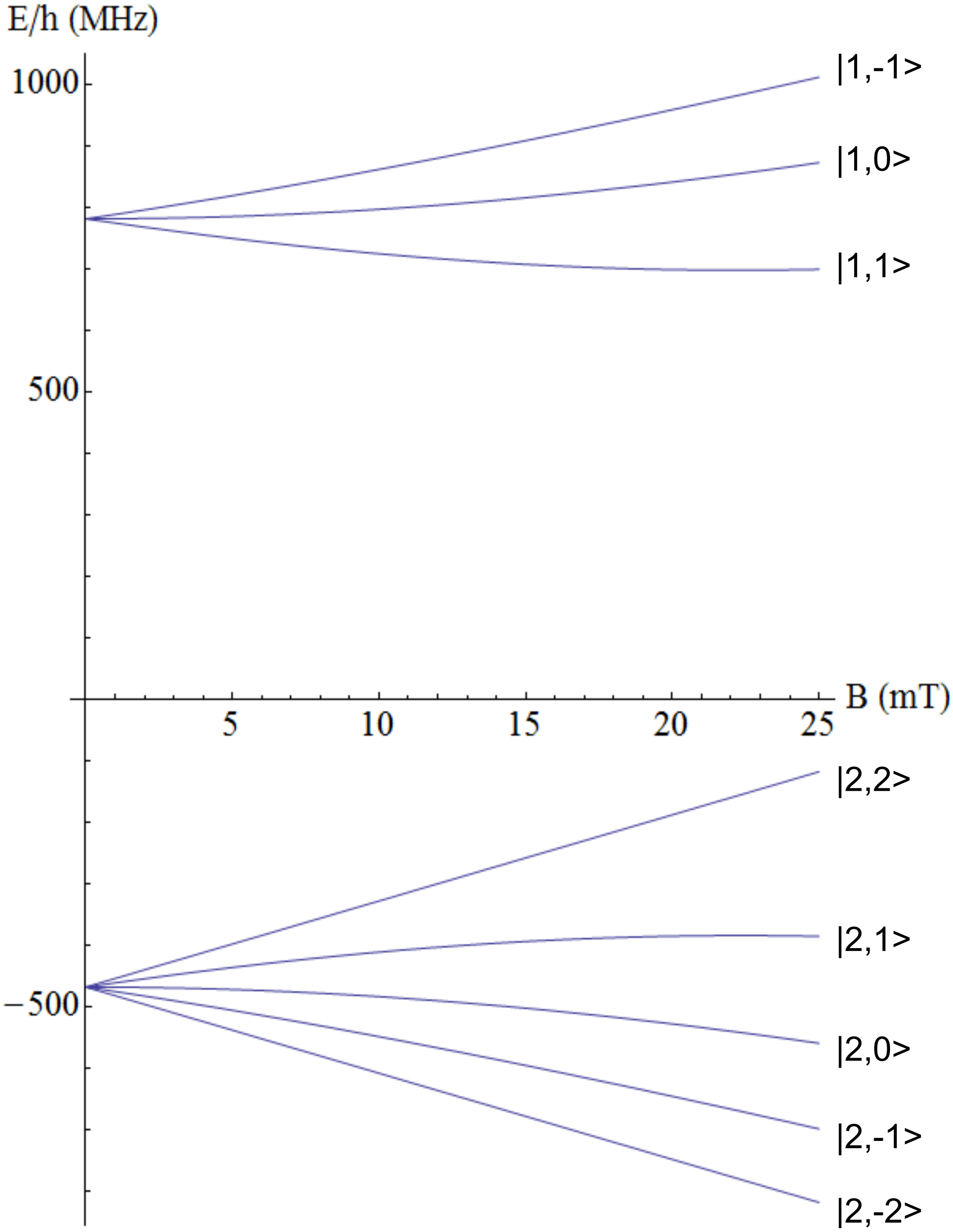

Figure 2.2: Zeeman shift as a function of magnetic field of the $S_{1/2}$ hyperfine states calculated via the Breit-Rabi formula. The states are labeled in the $|F, m_F\rangle$ basis. Two of the first-order field-fluctuation insensitive pairs of hyperfine states that are available to our experiments are the $|2,0\rangle \longleftrightarrow |1,1\rangle$ states at $B = 11.945$ mT, which have a splitting of 1207.50 MHz, and the $|2,1\rangle \longleftrightarrow |1,0\rangle$ states at $B = 11.964$ mT, which have a splitting of 1207.35 MHz.

of laser-cooling can be found in Ref. [36], and Doppler cooling on an ion was demonstrated in Refs. [37, 38] and were the first demonstrations of laser-cooling of atoms.

The typical treatment for Doppler cooling is for a laser beam used for cooling, detuned from resonance for a closed two-level transition. A laser beam is applied to the spatial region of the ion trap with its frequency set red-detuned by Δ_0 from the $S_{1/2}$ to $P_{3/2}$ resonance. The steady-state scattering rate is [31]

$$\gamma = \frac{\Gamma}{2} \frac{I/I_{sat}}{1 + I/I_{sat} + (2\Delta/\Gamma)^2}, \tag{2.3.1}$$

where Γ is the excited state's linewidth, I_{sat} is the saturation intensity [31], and $\Delta = \Delta_0 - k \cdot v$ is the detuning which varies with Doppler shift kv for light with wavenumber k and ion velocity v along the beam. For slowly-varying v, an ion with a velocity component opposite to the laser beam sees a blue detuning in the ion frame, bringing the light closer into resonance and resulting in a scattering force

$$F_{sc} = \hbar k \gamma \tag{2.3.2}$$

and a corresponding "damping coefficient" from $F_{damping} \simeq -\frac{\partial F}{\partial \omega} kv = -\mu v$ [39, 31] such that

$$\mu = -\frac{8k\Delta/\Gamma^2}{1 + I/I_{sat} + (2\Delta/\Gamma)^2} F_{sc} \tag{2.3.3}$$

This is a slowing force if Δ is negative (red-detuned) and heats the ion otherwise.

When light scatters off of the ion, photons fly off in random directions imparting momentum kicks $\hbar k$. The emitted photons lead to diffusion in velocity space, but the ion's velocity components along the beam experiences a slowing force. As the ion's velocity along the beam direction slows, so too does the scattering rate as the Doppler shift relaxes the beam's detuning away from resonance. The minimum temperature is reached at an equilibrium between absorption and re-emission, called the Doppler cooling limit. The Doppler cooling limit is reached with $\Delta_0 = -\Gamma/2$ and $I/I_{sat} \ll 1$, corresponding to a temperature [31]

$$k_B T_{min} = \frac{\hbar\Gamma}{2}, \tag{2.3.4}$$

where k_B is Boltzmann constant.

In an ion trap, there are three axes, and it is necessary to be able to consider Doppler cooling along each axis, which requires considering the alignment and polarization of the Doppler cooling beam with respect to our ion-trap geometry [40]. Our Doppler cooling light is σ^+-polarized and is red-detuned from the closed two-level cycling transition $|S_{1/2}, F = 2, m_F = 2\rangle \longleftrightarrow |P_{3/2}, F = 3, m_F = 3\rangle$ which has a linewidth of $\Gamma \simeq 2\pi \times 19.4$ MHz. In the case of a Doppler cooling beam with wavevector k and considering cooling along an axis i, the Doppler cooling temperature is given by [40, 39]

$$k_B T_{min} = \frac{\hbar\Gamma\sqrt{1 + I/I_{sat}}}{4}(1 + \frac{f_{si}}{f_i}) \tag{2.3.5}$$

where $f_i = \hat{k}_i^2$ and $f_{si} = \int P_s(\hat{k}_s)\hat{k}_{si}^2 d\Omega$ for scattered light with wavevector k_s and spatial distribution P_s. For isotropic scattering such that $f_{si} = 1/3$ for each axis i and $\hat{k} = \frac{1}{\sqrt{3}}(\hat{x} + \hat{y} + \hat{z})$ with a beam intensity $I/I_{sat} \ll 1$, then Eq. 2.3.5 agrees with the former cooling limit given by Eq. 2.3.4.

The experiment uses a Doppler cooling beam aligned with the external magnetic field axis $\hat{B}$, which lies at 45° to the $\hat{x}$ axis with respect to our ion trap. In spherical coordinates, the scattered light distribution for the σ^--polarized dipole scattering is given by [41]

$$P_s(\hat{k}_s) = (3/16\pi)[1 + \cos^2\theta_s] \tag{2.3.6}$$

where $\hat{B} \cdot \hat{k}_s = \cos\theta_s$. For example, the projection of the scattered light onto the $\hat{x}$-axis gives $\hat{k}_{si}^2 = (\sin\theta_s \cos\phi_s + \cos\theta_s)^2/2$ in spherical coordinates. The integration evaluates to $f_{si} = 7/20$ and the incident Doppler cooling beam's alignment projected onto the $\hat{x}$-axis gives $f_i = 1/2$, and putting these into Eq. 2.3.5 with $I/I_{sat} \ll 1$ solves for the theoretical Doppler cooling limit of ~0.4 mK.

2.4 State Initialization

Preparing our qubit in a well-defined initial state in every experiment is a vital part of our qubit operations. We perform optical pumping on ^{9}Be$^+$ with laser light, and from there we can perform coherent transitions to work with our qubit manifold. The P states decay with $1/\Gamma$=8.2 ns, providing rapid spontaneous decay back to the $S_{1/2}$ manifold. The $S \longleftrightarrow P$ transition can be accessed with dipole radiation at 313 nm. By selecting σ^+-polarized light propagating along the B direction, the light drives $m_F \longleftrightarrow m_F+1$ transitions. The proper combination of laser light can then prepare ^{9}Be$^+$ in the $|2,2\rangle$ initial state. Once in our initial state, we can coherently excite transitions as needed about the hyperfine manifold for qubit manipulations.

Several laser beams are used for state initialization and are shown in Fig. 2.3. We assume that the $S_{1/2}$ states are initially randomly populated. The Blue Doppler (BD) laser beams play a role in state initialization (while this is not their principle purpose, the role in optical pumping is important). Blue Doppler beams include both near-resonant (BD) and far-detuned (BD detuned) lasers coupling the $|S_{1/2}, F=2, m_F=2\rangle \longleftrightarrow |P_{3/2}, F=3, m_F=3\rangle$ transition. The BD detuned beam is $\sim$ -400 MHz detuned from this transition and is used to pre-cool very hot ions. This beam has several times the saturation intensity, and couples all of the $F=2$ states and $F=1$ states to $P_{3/2}$ with $m_F \longleftrightarrow m_F+1$ transitions, and therefore pumps all $S_{1/2}$ state-population towards the $|2,2\rangle$ state. The BD beam is near-detuned by $-\Gamma/2 \simeq -2\pi\times 9.7$ MHz from the transition and at less than the saturation intensity, which is chosen to satisfy the conditions for reaching the Doppler cooling limit. It would be on the order of milliseconds to reliably pump to the $|2,2\rangle$ state from all of the $F=2$ and $F=1$ states with the BD beams due to the far off-resonance transitions, so after the BD beams are applied to transfer population to near the $|2,2\rangle$ state, dedicated repumping beams are used to more efficiently prepare the initial state.

The core repumping beams couple the $S_{1/2}$ state to $P_{1/2}$ state with σ^+-polarized light. These are used following some amount of state preparation by the BD beams. A resonant repumping beam, or the "repumper" beam, resonantly drives the $|S_{1/2}, F=2, m_F=1\rangle \longleftrightarrow |P_{1/2}, F=2, m_F=$

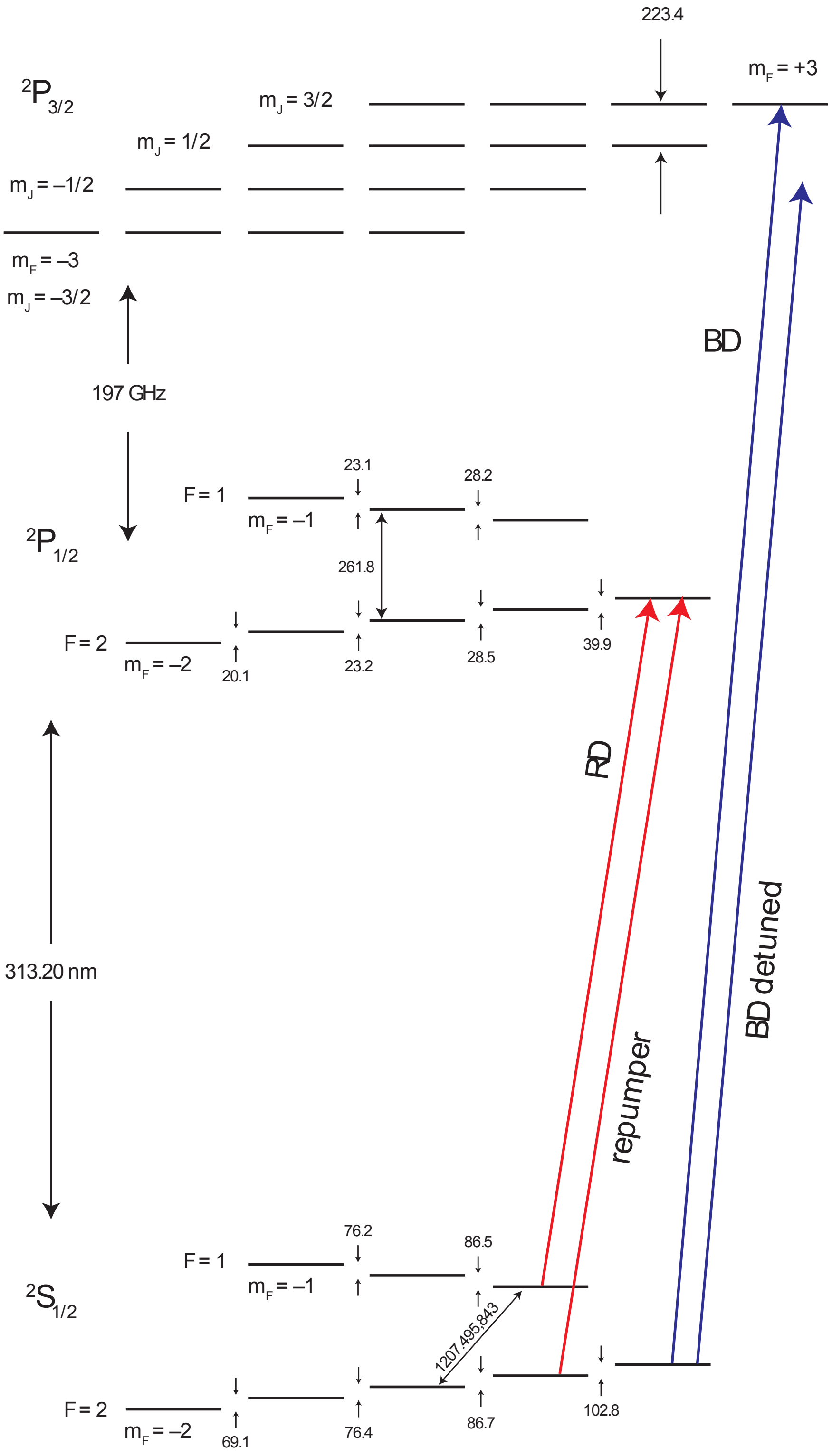
223.4
$^2P_{3/2}$
m_J = 3/2
m_F = +3
m_J = 1/2
m_J = –1/2
m_F = –3
m_J = –3/2
BD
197 GHz
23.1
28.2
F = 1
m_F = –1
$^2P_{1/2}$
261.8
F = 2
m_F = –2
20.1
23.2
28.5
39.9
RD
313.20 nm
repumper
BD detuned
76.2
86.5
F = 1
m_F = –1
$^2S_{1/2}$
1207.495.843
F = 2
m_F = –2
69.1
76.4
86.7
102.8

Figure 2.3: Atomic structure diagram of ^{9}Be$^+$ at B=11.94 mT showing the state-preparation laser couplings. The blue Doppler (BD) beams couple $S_{1/2}$ to $P_{3/2}$ and red Doppler (RD) beams couple to the $P_{1/2}$ state with σ^+-polarized light to optically pump into the $|2,2\rangle$ initial state.

$2\rangle$ transition. The $|P_{1/2}, F=2, m_F=2\rangle$ state dominantly decays by the dipole-allowed transitions to the $|2,2\rangle$, $|1,1\rangle$, and $|2,1\rangle$ states. Another beam, the Red Doppler (RD) repump beam, so-called historically due to being detuned to the red of the $|S_{1/2}, F=1, m_F=1\rangle \longleftrightarrow |P_{1/2}, F=2, m_F=2\rangle$ transition, is used as well. The detuning avoids a "dark state" that can arise from a coherent process from interference between the two repumping beams when they are at the same detuning from the $P_{1/2}$ state [42], and to avoid this, the RD beam is detuned by $\sim$ -20 MHz. As the incident repumping light is σ^+-polarized, once population is entirely pumped to the initial $|2,2\rangle$ state, the beams will no longer be able to drive transitions to the $P_{1/2}$ manifold due to selection rules. For any population in states of the $S_{1/2}$ manifold other than the $|2,2\rangle$, $|1,1\rangle$, and $|2,1\rangle$ states, any off-resonant transitions from $S_{1/2}$ to $P_{1/2}$ or $P_{3/2}$ can then allow decay to other states in the $S_{1/2}$ manifold (for example, when the $|1,-1\rangle$ state is excited, it can decay back to states other than those listed). However, the BD detuned and RD beams off-resonantly pump $F=2$ and $F=1$ states towards the $|2,2\rangle$ state. The combination of these repumping beams therefore asymptotically prepares the ion in the $|2,2\rangle$ state.

It is best to keep both repumping beam intensities below the saturation intensity, or else imperfect polarization components including σ^- (since light is along the B-axis, there is no π-polarization) can lead to significant depumping of $|2,2\rangle$. Each RD beam can have its intensity independently varied for an optimal value. The state initialization sequence begins with BD detuned, BD, RD, and repumper beams applied for the order of a $\sim$2 ms duration. Following this, we then apply the BD, RD, and repumper beams for $\sim$500 μs. Lastly, the RD and repumper are applied for $\sim$10 μs in the final stage of state preparation. The combination of all of the beams prepare the $|2,2\rangle$ state with near-unity population (Ref. [34] estimates repumping with an error on the order of 10^{-5}, accounting for imperfect polarization). Whenever the state needs to be re-initialized in the middle of an experiment, the repumper beams are applied for $\sim$10-30 μs to prepare the $|2,2\rangle$ initial state.

2.5 Stimulated Raman Transitions

After state initialization to the $|2,2\rangle$ state, we coherently transition to the $|2,1\rangle$ state and from there perform qubit rotations on the $|2,1\rangle \longleftrightarrow |1,0\rangle$ transition. Here, I use the notation for qubit states $|\downarrow\rangle \longleftrightarrow |\uparrow\rangle$. However, the qubit splitting of 1.2 GHz and the Zeeman splitting between m_F states of $\sim$100 MHz makes direct laser transitions impractical. A common technique is to use two-photon stimulated Raman transitions [43, 6] to control the $S_{1/2}$ hyperfine structure with two beams separated in frequency by the transition splitting. For the following, I consider an idealized three-level system.

Incident laser light from two beams have the electric fields

$$E_i = \hat{\varepsilon}_i E_i \cos(k_i \cdot x - \omega_{\mathrm{L}i} t + \phi_i) \tag{2.5.1}$$

for $i \in \{1,2\}$, with L1 and L2 denoting the two beams with polarizations $\hat{\varepsilon}_i$ wavevectors k_i and frequencies $\omega_{\mathrm{L}i}$. Laser beam L1 performs coupling from an initial ground state $|\downarrow\rangle$ to an intermediate state $|\mathrm{i}\rangle$ spaced from $|\downarrow\rangle$ by ω_i (in our case, the $S \longleftrightarrow P$ transition splitting; while both P states contribute, this analysis will consider coupling to a single intermediate state) detuned by Δ from resonance. Laser beam L2 similarly couples the final excited state $|\uparrow\rangle$ to the intermediate state $|\mathrm{i}\rangle$ with detuning Δ, and $|\omega_{\mathrm{L2}} - \omega_{\mathrm{L1}}| = \omega_0$ is the splitting between the desired hyperfine transition (diagrammed in Fig. 2.4). Hence, $\omega_{\mathrm{L1}} = \omega_i - \Delta$ and $\omega_{\mathrm{L2}} = \omega_i - \Delta - \omega_0$ in terms of the internal state frequencies. As of this thesis, our two Raman beams are $\sim$ -250 GHz red-detuned from the $P_{1/2}$ state.

The wavefunction for the three-level system for the states s is

$$\Psi = \sum_{s=\downarrow,\uparrow,\mathrm{i}} C_s(t)|s\rangle, \tag{2.5.2}$$

where C_s is the normalized coefficient for each state. The interaction Hamiltonian is

$$H_I = -\bar{\mu} \cdot (E_1 + E_2) \tag{2.5.3}$$

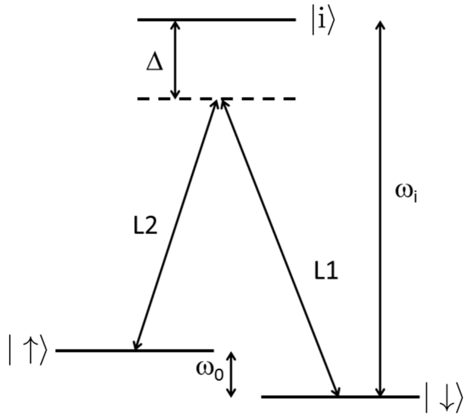
$|\text{i}\rangle$
Δ
ω_i
L2
L1
$|\uparrow\rangle$
ω_0
$|\downarrow\rangle$

Figure 2.4: Diagram of a stimulated Raman transition coupling the ground state $|\downarrow\rangle$ to excited state $|\uparrow\rangle$. Laser L1 couples the ground state $|\downarrow\rangle$ to an intermediate state $|\text{i}\rangle$ detuned by Δ from resonance. Laser L2 likewise couples the excited state $|\uparrow\rangle$ to an intermediate state $|\text{i}\rangle$ with a detuning Δ. The laser frequencies are split by $|\omega_{L2} - \omega_{L1}| = \omega_0$, each beam with respective k-vectors k_2 and k_1.

for dipole coupling between the dipole moment $\bar{\mu}$ and the incident lasers. It is convenient to transform to the interaction picture by taking $H_I' = e^{iH_0 t/\hbar} H_I e^{-iH_0 t/\hbar}$, where $H_0 = H_{internal}$ is the time-independent Hamiltonian for the three internal atomic states (this is effectively like transforming to the frame of the atomic states for the interaction). Transforming to the interaction picture and taking the rotating wave approximation gives

$$H_I' = \hbar g_1 \exp(i(k_1 \cdot x + \phi_1)) \exp(i\Delta t) |\downarrow\rangle\langle \mathrm{i}| + \hbar g_2 \exp(i(k_2 \cdot x + \phi_2)) \exp(i\Delta t) |\uparrow\rangle\langle \mathrm{i}| + h.c., \quad (2.5.4)$$

with multiplying factors $g_1 = -\frac{E_1}{2\hbar}\langle\downarrow|\bar{\mu}\cdot\hat{\varepsilon_1}|\mathrm{i}\rangle$ and $g_2 = -\frac{E_2}{2\hbar}\langle\uparrow|\bar{\mu}\cdot\hat{\varepsilon_2}|\mathrm{i}\rangle$ as short-hand. Then, applying Schrödinger's equation for the laser interactions, we have

$$\begin{aligned} \dot{C}_\downarrow &= -ig_1 \exp(i(k_1 \cdot x + \phi_1)) \exp(i\Delta t) C_\mathrm{i} \\ \dot{C}_\uparrow &= -ig_2 \exp(i(k_2 \cdot x + \phi_2)) \exp(i\Delta t) C_\mathrm{i} \\ \dot{C}_\mathrm{i} &= -i(g_1^* \exp(-i(k_1 \cdot x + \phi_1)) C_\downarrow + g_2^* \exp(-i(k_2 \cdot x + \phi_2)) C_\uparrow) \exp(-i\Delta t). \end{aligned} \quad (2.5.5)$$

If the detuning Δ is much larger than the coupling rates g_1 and g_2 and larger than the natural linewidth Γ of the state $|\mathrm{i}\rangle$, which is the case for the ^{9}Be$^+$ P states, then there is relatively little population in the $|\mathrm{i}\rangle$ state, i.e., $\dot{C}_\mathrm{i}$ is much less than $\dot{C}_{\uparrow,\downarrow}$ and therefore can be neglected. However, C_i must still be integrated to include in the $\dot{C}_{\uparrow,\downarrow}$ terms.

$$\dot{C}_\mathrm{i} = -\int i(g_1^* \exp(-i(k_1 \cdot x + \phi_1)) C_\downarrow + g_2^* \exp(-i(k_2 \cdot x + \phi_2)) C_\uparrow) \exp(-i\Delta t) dt \quad (2.5.6)$$

Integrating each term separately by parts gives first the term with $C_\downarrow$ as

$$C_\mathrm{i}^{\downarrow\text{-term}} = -ig_1^* \exp(-i(k_1 \cdot x + \phi_1)) \left[-\frac{C_\downarrow \exp(-i\Delta t)}{i\Delta} + \frac{1}{i\Delta} \int \dot{C}_\downarrow \exp(-i\Delta t) dt \right]. \quad (2.5.7)$$

With another round of integration by parts, this becomes

$$C_{\mathrm{i}}^{\downarrow\text{-term}} = -ig_1^* \exp(-i(k_1 \cdot x + \phi_1)) \left[-\frac{C_\downarrow \exp(-i\Delta t)}{i\Delta} + \frac{1}{i\Delta} \left[-\frac{\dot{C}_\downarrow \exp(-i\Delta t)}{i\Delta} + \frac{1}{i\Delta} \left(\int \ddot{C}_\downarrow \exp(-i\Delta t) \right] \right] \tag{2.5.8}$$

with a similar expression for the term including $C_\uparrow$. The increasing factors of $1/\Delta$ are increasingly vanishing, and so we only keep the terms first-order in $1/\Delta$, giving the coefficients

$$\begin{aligned} \dot{C}_\downarrow &= ig_1 \exp(i\Delta t)[ig_1^* \frac{C_\downarrow \exp(-i\Delta t)}{i\Delta} + ig_2^* \frac{C_\uparrow \exp(-i\Delta t)}{i\Delta} \exp(-i(\delta k \cdot x + \delta\phi)] \\ \dot{C}_\uparrow &= ig_2 \exp(i\Delta t)[ig_1^* \frac{C_\downarrow \exp(-i\Delta t)}{i\Delta} + ig_2^* \frac{C_\uparrow \exp(-i\Delta t)}{i\Delta} \exp(i(\delta k \cdot x + \delta\phi)]. \end{aligned} \tag{2.5.9}$$

where $\delta k \cdot x + \delta\phi$ denote the differences between the k-vectors $k_2 - k_1$ and phases $\phi_2 - \phi_1$ of the two beams.

The coefficients in Eq. 2.5.9 give rise to an effective two-state system, coupling $|\downarrow\rangle$ to $|\uparrow\rangle$ with very limited population in $|\mathrm{i}\rangle$ during the process. The corresponding effective Hamiltonian is then

$$H = -\hbar \left[\frac{|g_1|^2}{\Delta} |\downarrow\rangle\langle\downarrow| + \frac{g_1 g_2^*}{\Delta} |\downarrow\rangle\langle\uparrow| \exp(-i(\delta k \cdot x + \delta\phi)) + \frac{|g_2|^2}{\Delta} |\uparrow\rangle\langle\uparrow| + \frac{g_2 g_1^*}{\Delta} |\uparrow\rangle\langle\downarrow| \exp(i(\delta k \cdot x + \delta\phi)) \right] \tag{2.5.10}$$

This Hamiltonian is in the form of the familiar interaction with monochromatic radiation in a two-level system, which induces Rabi oscillations between the states $|\downarrow\rangle$ and $|\uparrow\rangle$ [31], but is characterized by the phase difference between the two laser beams $\delta k \cdot x + \delta\phi$ and a Rabi rate given by

$$\Omega_{Raman} = -\frac{g_1^* g_2}{\Delta}. \tag{2.5.11}$$

The diagonal terms of Eq. 2.5.10 are the usual AC Stark Shifts [31], which can be accounted for with a suitable tuning of the laser frequencies.

The Rabi rate in Eq. 2.5.11 depends both on the incident laser beam intensities (or, the electric field amplitude) and depends inversely on the detuning Δ (which also dictates population in $|\mathrm{i}\rangle$), offering tradeoffs between our available laser beam powers, possible detunings, and qubit operation speeds. The steady-state scattering rate off of the intermediate state γ (see Eq. 2.3.1) introduces a loss mechanism if $|\mathrm{i}\rangle$ can scatter to a state outside of $|\downarrow\rangle$ and $|\uparrow\rangle$, which is possible as the three-level system considered above is only an idealization of the $^9\mathrm{Be}^+$ atomic structure during a Raman transition.

This analysis can be extended to include multiple intermediate states, which applies to our specific case as the Raman transitions are driven in the presence of both $P_{1/2}$ and $P_{3/2}$ states. For a suitably large detuning from all intermediate states, such that every respective occupation C_j for the j^{th} intermediate state is very small, then the Raman transitions induce Rabi oscillations where the Rabi rate has contributions from Raman scattering off of each intermediate state. The general expression is then [44]

$$\Omega_{Raman} = \frac{E_1 E_2}{4\hbar^2} \sum_{\mathrm{i}} \frac{\langle \uparrow |\bar{\mu} \cdot \hat{\varepsilon_2} |\mathrm{i}\rangle \langle \mathrm{i}|\bar{\mu} \cdot \hat{\varepsilon_1}| \downarrow\rangle}{\Delta_{\mathrm{i}}} \tag{2.5.12}$$

for intermediate states i with detuning Δ_{i} from the respective intermediate state.

Our stimulated Raman transitions are driven with lasers composed of a combination of σ^--, π-, and σ^+-polarized light. Beam L1 has π-polarization with k_1 perpendicular to the magnetic field B direction. Beam L2, with k_2, is either co-propagating or 90° relative to k_1 and has σ^+ and σ^- polarization components. This enables $\Delta m_F = \pm 1$ transitions when implementing stimulated Raman transitions. For a detuning Δ from the $P_{1/2}$ state and detuning $\Delta - \Delta_f$ from the $P_{3/2}$ state, where Δ_f is the fine-structure splitting between the P states, then using appropriate Clebsch-Gordan coefficients allows the Rabi rate to be rewritten as [44]

$$\Omega_{Raman} = \frac{g_1 g_2}{\sqrt{6}} (\varepsilon_{1,\pi}\varepsilon_{2,\sigma^+} + \varepsilon_{1,\sigma^-}\varepsilon_{2,\pi}) \frac{\Delta_f}{\Delta(\Delta - \Delta_f)}, \tag{2.5.13}$$

where $g_{1,2}$ are the matrix elements $\frac{E_{1,2}}{2\hbar} |\langle \downarrow |\bar{\mu} \cdot \hat{\sigma}^+ | P_{3/2}\rangle|$ and $\varepsilon_{i,j}$ is the j^{th}-polarization component of the i^{th} laser beam.

During experiments, after state initialization into the $|2,2\rangle$ state, we drive a Raman transition to the $|2,1\rangle$ state, and from there perform coherent qubit rotations on the $|2,1\rangle \longleftrightarrow |1,0\rangle$ qubit states. Our incident laser beams typically have $\sim$1 mW of power, waist $w_0 \simeq 30\mu$m, and drive Rabi oscillation π-times of $\sim 5\mu$s. The states in the $S_{1/2}$ hyperfine manifold have an effectively infinite lifetime, and to the degree that spontaneous scattering can be suppressed, enable near-perfect Rabi flopping between any choice of states, the linewidth only Fourier limited from pulse duration.

2.6 State Detection

Detecting the final measured qubit state is necessary to discern the result of a quantum information process, and this requires the ability to distinguish final qubit state populations of $|2,1\rangle$ and $|1,0\rangle$ to a high degree. The approach with ^{9}Be$^+$, and ions in general, is to use state-dependent resonant fluorescence. In some cases, the process rapidly scatters photons on a resonant transition without any optical pumping out of the transition manifold. We refer to the state used for detection as the "bright" state.

We use a laser beam at 313 nm with σ^+ polarization to resonantly couple the $|S_{1/2}, F = 2, m_F = 2\rangle \longleftrightarrow |P_{3/2}, F = 3, m_F = 3\rangle$ states. Due to selection rules, the only possible decay path when the $P_{3/2}$ state decays is back to the $|2,2\rangle$ state. Thus, this closed transition cycle rapidly scatters photons off of the ^{9}Be$^+$ ion from the bright $|2,2\rangle$ state. Before detection, we transfer population from $|2,1\rangle$ to $|2,2\rangle$, therefore enabling efficient detection of the $|2,1\rangle$ state (we often refer to $|1,0\rangle$ as our "dark" qubit state). Our detection beam is derived from our BD beam shifted onto resonance. A portion of the solid angle of scattered light can be under observation to collect the light and distinguish whether or not the ion is in the bright state. Typically the beam intensity is less than I_{sat} such that spontaneous emission dominates the return to the bright state from $P_{3/2}$. Scattering off of a dark state, such as $|1,1\rangle$, is suppressed because transitions from this state are $\sim$1.2 GHz detuned from the bright transition with very little scattering from the detection beam.

The observed scattering rate for the resonant fluorescence is limited by the $P_{3/2}$ decay rate of 8.2 ns, the solid angle for photon collection, and quantum efficiency of our detector. The steady-state scattering rate γ from the detection beam (see Eq. 2.3.1) with detuning Δ=0 for resonant light with I/I_{sat}=1/2 gives γ=$\Gamma/6$ and we can expect that in a 250 μs detection, $\sim$5000 photons will be scattered off of the bright state. In practice, our photon detection system will observe $\sim$30 photons in that duration for an ion in the bright state. When the ion is in the dark state, no photons should be collected, but typically there is a background of $\sim$1-2 photons primarily from stray background light.

One source of error in detection is due to off-resonant scattering off of the dark state. To further discriminate the bright and dark states, an "electron shelving" technique [45] transfers population in the dark qubit state to a state which is farther detuned from the detection beam. When detecting the qubit state, $|2,1\rangle$ population is transferred to $|2,2\rangle$ for detection and the $|1,0\rangle$ population is transferred to $|1,-1\rangle$.

Repeated detections over many trials builds up statistics that ideally obey a Poisson distribution, that is, a distribution that describes random results from a fixed average rate. The Poisson distribution obeys the probability density function

$$\frac{\mu^x}{x!}e^{-\mu}, \tag{2.6.1}$$

where μ here is the mean value and x is the number of counts in the distribution (see Fig. 2.5 for an example of collected data). When detecting multiple ions, there is a mean value for μ_0 for zero ions in the bright state, μ_1 for one ion in the bright state, μ_2 for two ions bright, etc, for the number of ions under detection light, which follows a normalized sum of Poisson distributions. More in-depth discussion on detection can be found in Ref. [34].

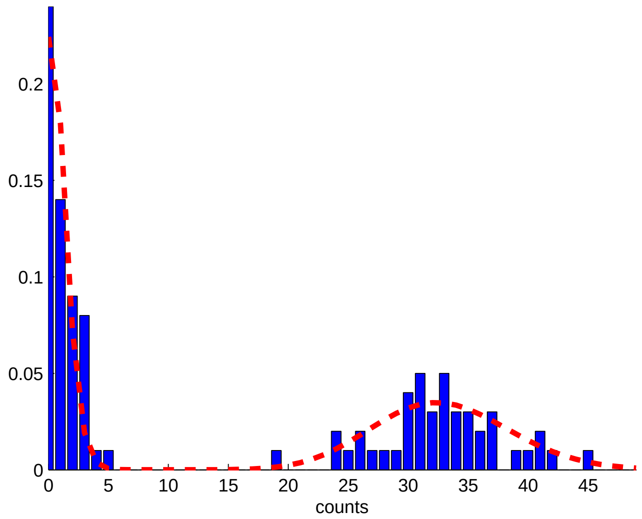

Figure 2.5: Example of detection data (blue histograms) from state-dependent resonant fluorescence for a 250 μs detection duration from an ion repeatedly prepared in a superposition of bright and dark states for 100 detections. The counts have been fit to normalized Poisson distributions (red dashed line). In this case, the data is consistent with measuring the ion in the bright state with $\sim$50% probability and average 32.86 PMT counts, and the ion in the dark state with $\sim$50% probability and average 0.80 PMT counts. The distributions for the bright and dark states are highly distinguishable.

Chapter 3

Motional Dynamics of Trapped Ions

To work with a trapped ion, we need to maintain a very strong spatial localization. By Earnshaw's theorem, it is impossible to have a purely confining static electric field with no local charge, and so to trap an ion, more complex fields are necessary. Two common types of ion traps are the RF Paul and the Penning trap. The Penning trap uses a combination of static electric and magnetic fields for confinement. The RF Paul trap, which uses a combination of time-varying and static electric fields, creates an effective confining potential, or pseudopotential. Our ion trap forms a three-dimensional harmonic oscillator, confining the ion to about $\sim$10 nm in every direction when they are cooled to near their ground state. We trap both ^{9}Be$^+$ and ^{24}Mg$^+$, and here I consider the motion of both trapped ion species.

We apply Doppler and Raman-sideband laser-cooling to the trapped ions to cool them to near the ground state of motion. The application of Raman pulses detuned by the oscillator frequencies allows us to couple directly to motional modes, and a judicious use of pulses coupled with repumping can be used to cool the ions to near the zero-point energy of the trap. At cold temperatures, the motion of the trapped ion is best described in terms of the number states of the quantum harmonic oscillator. The motion is inherently non-classical, and there are a few specific distributions of number states that are important in the dynamics of trapped ions. In this chapter I describe the quantum dynamics of for single and multiple trapped ions. I will begin with a description of the linear RF Paul trap and its harmonic confinement. Then I will describe some non-classical states of motion. Following this, I will describe the motional-state laser interactions, including motional state analysis and state initialization through laser cooling. The last section is on the atomic structure of ^{24}Mg^{+} and ^{25}Mg^{+}, which are used for "sympathetic" laser-cooling ions without disrupting the qubit-state of the ^{9}Be^{+} ions.

3.1 Linear RF Paul Trap

3.1.1 Idealized System

An ionic qubit may provide a promising basis for a QIP. However, it is not practical to work with ions without strict environmental control. For instance, coupling to a noisy environment, such as fluctuating electric or magnetic fields [6], can cause decoherence of the qubit state. In addition, it is difficult to selectively work with individual qubit ions without control over the spatial position of an ion. Selected ions could be lost from collisions with background gas, and it is desirable to confine ions in a system with little coupling other external environmental factors. Fortunately, a reasonable degree of decoupling from the environment can be achieved with an ion trap held in a vacuum system [46, 6, 35, 47].

One advantage to trapping ions is that their net charge allows the use of electric potentials for strong confinement (ions typically remain trapped for several hours). On this topic, Earnshaw's theorem states [31], "A charge acted on by electrostatic forces cannot rest in stable equilibrium in an electric field." The theorem can intuitively be understood from the fact that if there are no local static sources of an electric field $\bar{E}$, then $\nabla \cdot \bar{E} = 0$ in the region, i.e., there is no "sink" in three spatial dimensions. Fortunately, there are some ways around this problem.

One solution is to use time-varying electric fields combined with static electric fields. This solution is known as a linear radio-frequency (RF) Paul trap [48]; it is used for the work in this thesis. The basic idea of the Paul trap is to supply a combination of electric fields which would create a quadrupole, or "saddle point", potential. If this saddle point oscillates rapidly, it can generate stable confinement, i.e., it becomes an effective potential minimum in two or three dimensions at once.

A linear Paul trap can be built using conducting electrode rods in a quadrupole configuration;

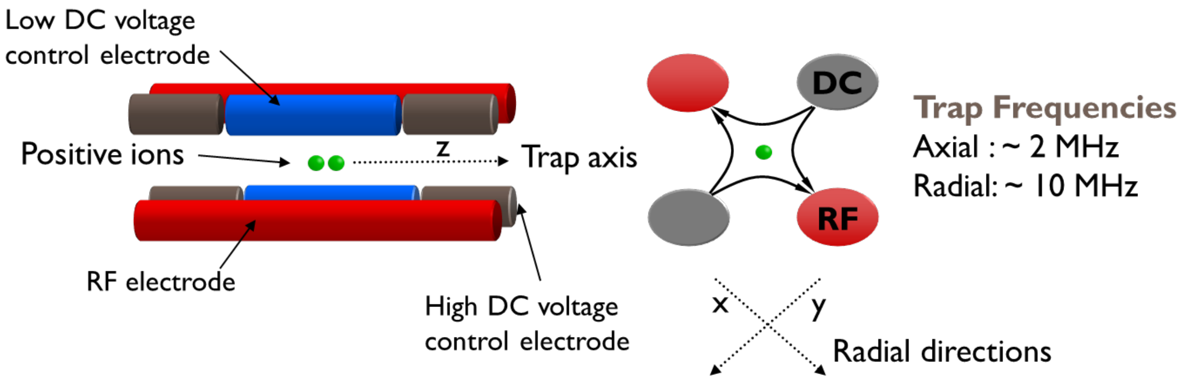
Low DC voltage control electrode
Positive ions
z
Trap axis
RF electrode
High DC voltage control electrode
DC
RF
Trap Frequencies
Axial : ~ 2 MHz
Radial: ~ 10 MHz
x
y
Radial directions

Figure 3.1: An idealized linear RF Paul trap with four parallel rod electrodes. A RF voltage is applied to diagonally opposite electrodes. The RF provides a harmonic pseudopotential along the radial directions, the x and y axes, wherein the ions are trapped at the potential null. The DC voltages, which are referenced to RF ground, are applied to another diagonally opposite pair of rod electrodes. The DC electrodes can be segmented and supplied with a combination of high outer-segment voltages and low inner-segment voltages to provide confinement along the z axis (also referred to as the trap axis).

an idealized diagram of this design is shown in Fig. 3.1. Applying time-varying electric fields can lead to stable ion confinement. Two pairs of diagonally opposite conducting rods carry an RF voltage $V = V_0 \cos(\Omega t)$, where Ω is the applied frequency. The other pair of rods are referenced to the RF ground. In this setup, we consider the potential due to the RF in the x and y radial directions, and z axis, which is also referred to as the trap axis. To achieve confinement along the trap axis, we create a static potential difference U_0 between the high DC electrode segments and the low DC electrode segments (as shown in Fig. 3.1). The electric potential ϕ must satisfy Laplace's equation, $\nabla^2\phi = 0$. The potential satisfying the boundary conditions is given by [49, 6, 39]

$$\phi = \frac{V_0 \cos(\Omega t)}{2R^2}[\alpha z^2 + \beta x^2 + \gamma y^2] + \kappa U_0[\alpha' z^2 + \beta' x^2 + \gamma' y^2], \tag{3.1.1}$$

where κ is an overall geometric factor and R is the distance from the trap axis to the surface of an electrode. Laplace's equation demands that $\alpha + \beta + \gamma = 0$ and that $\alpha' + \beta' + \gamma' = 0$. For the case $\alpha = 0$, the oscillating potential is uniform along the z axis, or "trap axis," for infinite length rods. This gives a generally good approximation in a linear Paul trap, as typical electrode scales are much larger than the confinement spatial extent. For our electrode geometry in Fig. 3.1, $\gamma = -\beta$ gives the desired potential, where the terms in the potential in Eq. 3.1.1 proportional to $\cos(\Omega t)$ are akin to rotating a saddle-point potential about the trap axis. Sometimes geometric factors are included to model different (and possibly imperfect) quadrupole configurations [39], but they are omitted from this analysis.

For the static potential, α', β', and γ' are determined by the electrode geometry. Laplace's equation constrains the coefficients in Eq. 3.1.1 to $\alpha' + \beta' + \gamma' = 0$, and for our symmetric configuration, $\beta' = \gamma'$, and for an ion of mass m and charge $q = |e|$, the potential can be rewritten in the more common harmonic oscillator notation to be

$$\phi_s = \frac{m}{2q}\omega_z^2[z^2 - \frac{1}{2}(x^2 + y^2)], \tag{3.1.2}$$

where $\omega_z^2 = 2\kappa q U_0/m$ is the center-of-mass oscillation frequency along the trap axis. The potential in Eqs. 3.1.1 is the lowest-order expression for the potential, which is reasonably valid for ions near the trap center provided that the spatial extent of the trapped ion's motion is much less than the ion-electrode distance R. The total potential is then given by

$$\Phi_{tot} = \frac{V_0 \cos(\Omega t)}{2}\left(\frac{x^2 - y^2}{R^2}\right) + \frac{m}{2q}\omega_z^2[z^2 - \frac{1}{2}(x^2 + y^2)]. \tag{3.1.3}$$

The classical equations of motion in the x and y directions are

$$\frac{\mathrm{d}^2 x}{\mathrm{d}\varsigma^2} + [a_x + 2q_x \cos(2\varsigma)]x = 0, \tag{3.1.4}$$

$$\frac{\mathrm{d}^2 y}{\mathrm{d}\varsigma^2} + [a_y + 2q_y \cos(2\varsigma)]y = 0. \tag{3.1.5}$$

These equations use the following variable substitutions: $\varsigma = \Omega t/2$, $a_x = a_y = -(4q\kappa U_0/m\Omega^2)$, and $q_x = -q_y = (2qV_0/\Omega^2 m R^2)$. The notation used in this derivation is the usual notation seen in ion trap literature, where q_i is not an electric charge and a_i is not a lowering operator of the quantum harmonic oscillator. Typically the relationship $a_i < q_i^2 \ll 1$ holds true. These equations are known as the Mathieu equations, which can be solved with known Floquet solutions [49, 6]. They are classical equations but are sufficient for describing the the potential wells The solutions of the Mathieu equations, to the lowest order in a_i and q_i, give us[6]

$$u_i(t) = A_i\left[\cos(\omega_i t)[1 + \frac{q_i}{2}\cos(\Omega t)] + B_i \frac{q_i}{2}\sin(\omega_i t)\sin(\Omega t)\right], \tag{3.1.6}$$

where i denotes the x or y directions, the amplitude A_i depends on initial conditions, and $B_i \simeq (a_i + q_i^2/2)^{1/2}$. Three motional frequencies arise, with two in the radial direction at $\Omega \pm \omega_i$, and the last at frequency $\omega_i = B_i\Omega/2$. For $a_i < q_i^2 \ll 1$, ω_i is much smaller than Ω. According to Eq. 3.1.6, oscillation terms at $\Omega \pm \omega_i$ have a much lower amplitude by at least a factor of $q_i/2$; these terms give rise to "micromotion." If the micromotion is neglected, the potential can be expressed as

$$\phi_p = \frac{m}{2q}\omega_r^2(x^2 + y^2), \tag{3.1.7}$$

for radial confinement where the static potential is negligible. Equation 3.1.7 forms a "pseudopotential" harmonic confinement in the radial directions with frequency

$$\omega_r \simeq qV_0/(\sqrt{2}\Omega m R^2) = q_x\Omega/(2\sqrt{2}). \tag{3.1.8}$$

Hence, we have the result that the linear RF Paul trap forms three-dimensional harmonic confinement governed by the potentials in Eqs. 3.1.2 and 3.1.7 and with frequencies ω_z and ω_r. However, critically, the Eq. 3.1.7 has an overall $1/m$ dependence and thus the radial potential varies with mass. The linear RF Paul trap has strong confinement, and it's typical to maintain a trapped ion for a mean lifetime of four hours, which is sufficient to collect experimental data.

There are both stable and unstable solutions depending on a_i and q_i (which could be translated to design parameters such as R and Ω for real-trap construction). A detailed analysis of "stability regions" in the parameter space of a_i and q_i can be found in Refs. [49, 39], though the motion is always stable for $a_i < q_i^2 \ll 1$. Another issue can arise if the potential is not a perfect quadrupole. Geometric imperfections can be accounted for in geometric factors such as κ, but for more serious design considerations, an analysis of higher-order terms in the potential may be necessary; details of this approach can be found in Ref. [50].

The radial symmetry for the pseudopotential is broken by the static DC potentials along the trap axis, which gives rise to anti-confinement in the radial directions. The total potential can be written with the geometric factors $z^2 - \alpha x^2 - (1-\alpha)y^2$ at the position of the ions. This means that the radial frequencies are given by

$$\omega_x = \omega_r\sqrt{1 - \alpha\omega_z^2/\omega_r^2}, \tag{3.1.9}$$

$$\omega_y = \omega_r\sqrt{1 - (1-\alpha)\omega_z^2/\omega_r^2}. \tag{3.1.10}$$

Or, if ω_x and ω_y can be independently evaluated such as through an experimental measurement, then the pseudopotential can be calculated with

$$\alpha = \frac{1}{2}\left(1 - \frac{\omega_x^2 - \omega_y^2}{\omega_z^2}\right), \tag{3.1.11}$$

$$\omega_r = \sqrt{\omega_x^2 + \alpha\omega_z^2}. \tag{3.1.12}$$

3.1.2 Nulling Micromotion

Unexpected or non-uniform static electric fields from the trap electrodes can lead to the trapped ions being pushed off of the pseudopotential null. In this situation, the radial micromotion at the trap frequency Ω will frequency modulate the laser beam interactions [51]. Heating can occur when the laser frequency is tuned near, but above the center frequency of a micromotion sidebands. To compensate for the effects of micromotion, a "shim," or differential voltage on diagonally-opposite pairs of electrodes, can be used to push the ion onto the trap axis. By observing fluorescence of an ion as a shim is varied, the frequency modulation can be measured, which will correspond to the Bessel function $J_0(\eta)$ with modulation index given by $\eta = A \times k$, where A is the micromotion amplitude at the displacement off of the pseudopotential null and k is the wavenumber of the light along the axis of the micromotion. A result of scanning a shim is shown in Fig. 3.2.

3.1.3 Normal Modes of Multiple Trapped Ions

The above treatment was for a single trapped ion. However, we often work with multiple trapped ions with different masses. Typically, $\omega_z < \omega_r$ to force multiple ions in a single trap to stay aligned in a one-dimensional crystal along the trap axis (as depicted in Fig. 3.1). However, as more ions enter the trap, the crystal may undergo a transition such that it is no long purely along the trap axis (such as a "zig-zag" pattern). It is required, then, that for two ions, $(\omega_r/\omega_z) > 1$ and that for three ions $(\omega_r/\omega_z) > 1.55$. For a number of ions $N_{ions} > 3$, there are several estimates, including $(\omega_r/\omega_z) > 0.73N_{ions}^{0.86}$ [52], though there is no exactly-known expression for maintaining a linear chain along the trap axis.

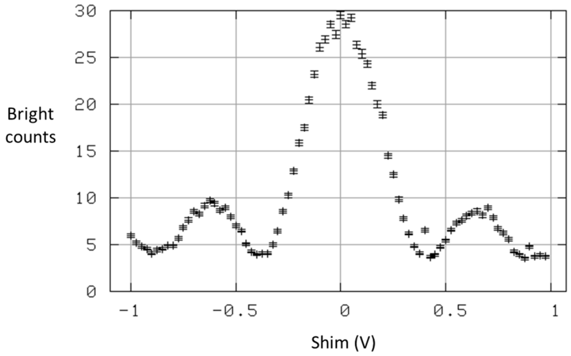

Figure 3.2: Varying a differential “shim” across two diagonally-opposite electrodes spaced apart by $\simeq 320\mu$m followed by detection of fluorescence on the cycling transition for a 250 μs duration. The shim values are applied as +Shim/2 and -Shim/2 on the opposite electrodes. The shim which gives maximum photon counts corresponds to a minimum in modulation, which occurs on the pseudopotential null. The non-zero minimum counts are due to background light.

As more ions are trapped, more normal modes must be included along the trap and radial axes as $N_{normal} = 3N_{ions}$. The problem becomes one of solving the frequencies of oscillation for all these normal modes given the equilibrium positions of ions, the Coulomb interaction between ions, and the variation in pseudopotential for different masses. I will assume that the frequencies for a single trapped ^{9}Be^{+} ion are known through measurement as ω_x, ω_y, and ω_z. For N_{ions} in the trap, there is a Coulomb coupling between the charges,

$$U_{cc} = \sum_{j=1}^{N_{ions}} \sum_{i=1}^{N_{ions}} \frac{k_e q^2}{|\bar{r}_i - \bar{r}_j|}, i < j, \tag{3.1.13}$$

where $k_e = 1/4\pi\varepsilon_0$ is the Coulomb coupling constant, $q = |e|$ the ion charge, and $\bar{r}_i$, $\bar{r}_j$ are the positions of the ions in three dimensions. The equilibrium positions along the trap axis can be solved from the real solutions to the system of equations from

$$-k_z z_i - \sum_{j=1}^{i-1} \frac{k_e q^2}{(z_i - z_j)^2} + \sum_{j=i+1}^{N_{ions}} \frac{k_e q^2}{(z_i - z_j)^2} = 0 \tag{3.1.14}$$

for each i^{th} ion. For two ions, the inter-ion distance is given by $d = (2k_e q^2/k_z)^{1/3}$.

The external potential is the same for each ion, and the axial confinement has no mass dependence. Therefore, the external potential on ions along the trap axis is

$$U_z = \sum_{i=1}^{N_{ions}} \frac{1}{2} k_z (\bar{r}_i \cdot \hat{z})^2 \tag{3.1.15}$$

where $k_z = m_{\mathrm{Be}}\omega_z^2$ is the axial spring constant, which is the same for all masses. The radial external potentials, properly scaled by mass, are

$$U_x = \sum_{i=1}^{N_{ions}} \frac{1}{2} \left(m_i \left[\frac{m_{\mathrm{Be}}}{m_i} \omega_r \right]^2 - \alpha k_z \right) (\bar{r}_i \cdot \hat{x})^2, \tag{3.1.16}$$

$$U_y = \sum_{i=1}^{N_{ions}} \frac{1}{2} \left(m_i \left[\frac{m_{Be}}{m_i} \omega_r \right]^2 - (1-\alpha) k_z \right) (\bar{r}_i \cdot \hat{y})^2, \tag{3.1.17}$$

for mass m_i of the ion at the i^{th} position and α given by Eq. 3.1.11. The total potential, then, is $U_{Tot} = U_{cc} + U_x + U_y + U_z$ and a coupling matrix can be formed.

Taking the frequency of small oscillations at the equilibrium positions,

$$k_{i,j} = \frac{\partial^2 U}{\partial i \partial j}, \tag{3.1.18}$$

we form a matrix of spring couplings $\overline{k}$ with elements $k_{i,j}$, and arrive at the eigenvalue problem [53]

$$k_{i,j} - \omega^2 m_{i,j} = 0. \tag{3.1.19}$$

To transform to mass-weighted coordinates, we take a diagonal matrix $\overline{m}$ with elements $1/\sqrt{m_i}$ and make the transformation

$$\bar{k}_{mass} = \overline{m} \cdot \overline{k} \cdot \overline{m}. \tag{3.1.20}$$

The eigenvalues of the matrix in Eq. 3.1.20 give the normal modes of motion and the eigenvectors give the normal mode amplitudes in mass-weighted coordinates.

I take as an example solving the normal modes for a two-ion, two-species crystal of ^{9}Be$^+$ and ^{25}Mg$^+$. The results of using the measured parameters

$$\begin{aligned} \omega_x &= 2\pi \times 13.33 \times 10^6 \\ \omega_y &= 2\pi \times 11.83 \times 10^6 \\ \omega_z &= 2\pi \times 3.59 \times 10^6 \end{aligned} \tag{3.1.21}$$

are given in Table 3.1.

3.1.4 Harmonic Oscillator States

The motion of trapped ions can be described in the energy basis of the harmonic oscillator [6, 39] to very good approximation. The harmonic oscillator Hamiltonian is

$$\hat{H} = \frac{\hat{p}^2}{2m} + \frac{m\omega^2 \hat{z}^2}{2}, \tag{3.1.22}$$

$\omega/2\pi$ (MHz)	$\hat{x}_{\text{Be}}$	$\hat{y}_{\text{Be}}$	$\hat{z}_{\text{Be}}$	$\hat{x}_{\text{Mg}}$	$\hat{y}_{\text{Mg}}$	$\hat{z}_{\text{Mg}}$
13.091	0.9997	0	0	0.0261	0	0
11.560	0	0.9995	0	0	0.0312	0
5.364	0	0	-0.9299	0	0	0.3677
4.846	-0.0261	0	0	0.9997	0	0
3.142	0	-0.0312	0	0	0.9995	0
2.492	0	0	0.3677	0	0	0.9299

Table 3.1: The normal modes for a ^{9}Be$^+$-^{25}Mg$^+$ linear ion crystal with mass-weighted coordinates.

where the operators $\hat{p}$, $\hat{z}$ are that of the usual momentum and position, respectively, for mass m and oscillator with frequency ω. The frequency ω can be for any normal mode of harmonic motion for a collection of trapped ions. If the operators $\hat{z}$ and $\hat{p}$ are rewritten with $a = \frac{1}{2}(\hat{z}/z_0 + \hat{p}/p_0)$ and $a^\dagger = \frac{1}{2}(\hat{z}/z_0 - \hat{p}/p_0)$, the Hamiltonian can be rewritten as

$$\hat{H} = \hbar\omega(a^\dagger a + \frac{1}{2}), \tag{3.1.23}$$

with the usual lowering operator $a|n\rangle = \sqrt{n}|n-1\rangle$, raising operator $a^\dagger|n\rangle = \sqrt{n+1}|n+1\rangle$, $z_0 = \sqrt{\hbar/2m\omega}$, and $p_0 = -i\sqrt{\hbar m\omega/2}$ (the position and momentum wavefunction packet sizes). The value z_0 offers a natural size scale for a trapped ion to be compared to trap sizes R or laser beam waists. A laser incident on an ion interacting with spin and motion has a convenient measure of the overlap between the trapped ion and incident laser light. This measure is the Lamb-Dicke parameter

$$\eta = kz_0, \tag{3.1.24}$$

where k is the incident laser's wave vector projected along the axis for the oscillator mode associated with z_0.

For each mode of frequency ω_i, there are discrete energy levels $E_n = \hbar\omega_i(n + \frac{1}{2})$ where n is an integer. Ions can be initialized in the lowest $n = 0$ energy state [54, 6] with high probability, and fields such as oscillating electric fields on the DC electrodes at frequency ω_i can cause excitations that populate higher n-states.

3.1.5 Re-ordering Ions

A mixed-species linear crystal of ions confined in an ion trap may not necessarily be in the desired order along the trap axis. When entangling two qubits, the ion crystal is often made up of two Be^+ ions as well as two Mg^+ ions, such as in Refs. [55, 29], and it is desirable to maintain symmetry in the crystal between the two qubit ions. For a $^9\mathrm{Be}^+$-$^{24}\mathrm{Mg}^+$ ion crystal, any anharmonicity in the trap potential can shift the normal mode frequencies depending on ion order [56]. Therefore, it is desirable to be able to re-order an ion crystal. The approach used in Refs. [29, 55, 56] and the work in this thesis takes advantage of the lower pseudopotential confinement for higher-mass ions.

To re-order a $^9\mathrm{Be}^+$-$^{24}\mathrm{Mg}^+$ ion crystal, or "BM," to either a BM or MB orientation, the heavier $^{24}\mathrm{Mg}^+$ ion must be pushed off-axis and torqued to the desired side of the $^9\mathrm{Be}^+$ ion along the trap axis. First, a shim is applied with sufficient strength such that the minimum-energy configuration for the ion crystal lies along the radial direction. Then, with the shim still applied, a torque is applied by adding a uniform bias field along the trap axis to push the $^{24}\mathrm{Mg}^+$ ion towards the desired side of the $^9\mathrm{Be}^+$ ion. Then the shim is removed, relaxing the ion crystal back onto the trap axis in the desired orientation.

When working with a four-ion crystal with two $^9\mathrm{Be}^+$ ions and two $^{24}\mathrm{Mg}^+$ ions, the BMMB configuration is the easiest to achieve. To re-order the ions into BMMB, the axial confinement strength is increased. The radial confinement is weakened as the axial confinement is increased. Beyond a critical point, the $^{24}\mathrm{Mg}^+$ ions will be forced off of the trap axis before $^9\mathrm{Be}^+$ due to the relatively weaker radial confinement. The lowest-energy crystal configuration at this point is for the two $^{24}\mathrm{Mg}^+$ to symmetrically lie along the radial direction perpendicular to the trap axis, and to be positioned between the two $^9\mathrm{Be}^+$ ions along the trap axis, in a "diamond" shape. This forces the two $^{24}\mathrm{Mg}^+$ ions at the center of the crystal, and if the axial confinement is then weakened, the crystal will return to the trap axis in the BMMB configuration.

3.2 Non-classical States of Motion

3.2.1 Coherent Distribution

The most classical-like state for the harmonic oscillator is the coherent state. In position-space, this is a state where the ground-state harmonic oscillator wavefunction is displaced from the trap minimum. For example, a coherent state can be excited by a sudden displacement of the trap minimum. The wavefunction is then displaced from the trap minimum with an amplitude number $|\alpha| = \frac{z_{max}}{2z_0}$ where z_0 is the wavefunction packet size for the ground-state wavefunction and z_{max} is the maximum displacement of the wavefunction center from the center of the trap.

The coherent state can be pictured in a phase-space image with a phase $\phi = \omega t$ as the phase evolves in a circle for a fixed amplitude $|\alpha|$, depicted in Fig. 3.3a, which is analogous to the classical behavior for the harmonic oscillator. The coherent state is related to the classical solutions of the harmonic oscillator by

$$|\alpha|e^{-i\omega t} = \frac{1}{2}(\frac{z(t)}{z_0} + \frac{p(t)}{p_0}), \tag{3.2.1}$$

for the position $z(t)$ and momentum $p(t)$ in the well.

The state $|\alpha\rangle$ is an eigenstate of the lowering operator such that

$$a|\alpha\rangle = \alpha|\alpha\rangle. \tag{3.2.2}$$

It is easy to verify that this is satisfied by

$$|\alpha\rangle = \sum_n \frac{\alpha^n}{\sqrt{n!}} e^{-|\alpha|^2/2}|n\rangle. \tag{3.2.3}$$

From this, the probability of each n-state is $P_n = |\langle n|\alpha\rangle|^2$, which gives the distribution of number states as

$$P_n = \frac{\bar{n}^n}{n!} e^{-\bar{n}}, \tag{3.2.4}$$

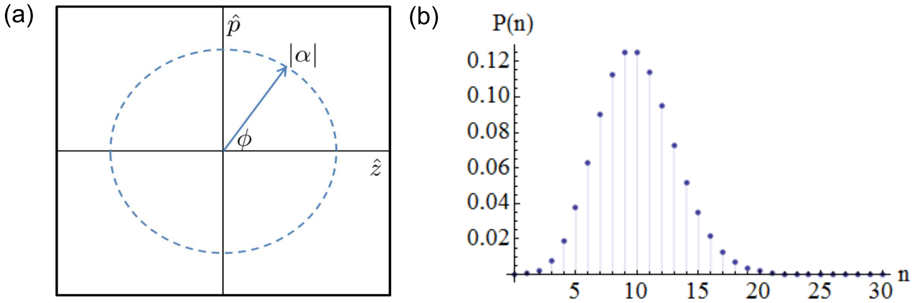

Figure 3.3: Diagram for a coherent state of motion. (a) Phase-space depiction of a coherent state $|\alpha\rangle$. The state evolves in a circle where $\phi = \omega t$ is the angle with respect to the coordinate $\hat{z}$-axis as given by Eq. 3.2.1. (b) Plot of the probability of each n-state for a coherent state with $\bar{n}$=10.

which is a Poissonian distribution over number states with mean value

$$\bar{n} = |\alpha|^2. \tag{3.2.5}$$

A coherent distribution over number states with $\bar{n} = 10$ is shown in Fig. 3.3b.

The displacement operator which creates the coherent state $\hat{D}(\alpha)|n=0\rangle = |\alpha\rangle$ is given by

$$\hat{D}(\alpha) = e^{\alpha a^\dagger - \alpha^* a}. \tag{3.2.6}$$

In Ref. [57], a coherent state was generated by applying a classical, resonant electric field to a trap electrode. The Hamiltonian for an oscillating potential along the normal mode axis $\hat{z}$ takes the form

$$V(t) = -eE_0\hat{z}\sin(\omega t - \phi) = i\frac{eE_0 z_0}{2}(a + a^\dagger)(e^{i(\omega t - \phi)} - e^{-i(\omega t - \phi)}) \tag{3.2.7}$$

for ion charge e and field amplitude E_0. In the interaction picture for the well, in which $a \to ae^{-i\omega t}$, and neglecting rapidly-oscillating terms with frequency 2ω, this becomes

$$V(t) = i\frac{eE_0 z_0}{2}(ae^{-i\phi} - a^\dagger e^{i\phi}). \tag{3.2.8}$$

The time-propagation operator for the interaction is then

$$U(t) = \exp[-\frac{eE_0 z_0}{2\hbar}t(ae^{-i\phi} - a^\dagger e^{i\phi})], \tag{3.2.9}$$

which is the displacement operator of Eq. 3.2.6 with

$$\alpha(t) = \frac{eE_0 z_0}{2\hbar} t e^{i\phi}. \tag{3.2.10}$$

This gives that the coherent state amplitude increases linearly with an applied resonant electric field.

3.2.2 Thermal Distribution

The thermal state often appears in ion trap motion which is most conveniently described as an incoherent distribution of number states. This motional distribution appears when there is a collection of random coherent kicks to the ion. This is the case for the motional distribution following Doppler cooling [36]. It also arises from a collection of random trap displacements over many observations of the motion. A common issue arises from ambient heating with a heating rate $\dot{\bar{n}}$ due to fluctuating electric field noise on trap surfaces radiating and interacting with the trapped ion [24, 25, 26] (typical heating rates for our systems is $\dot{\bar{n}} \sim 0.5$ quanta/ms). Measuring the ion motion from these random excitations over many measurements will give rise to observing the thermal distribution.

Treating the ion as being in contact with a thermal reservoir at temperature T, the motion has a probability of a particular number state

$$P_n = \frac{e^{-\beta E_n}}{Z} = \frac{e^{-\beta\hbar\omega(n+\frac{1}{2})}}{Z}, \tag{3.2.11}$$

where $\beta = 1/k_B T$, k_B being the Boltzmann constant, and Z is the partition function. The partition function is the sum over all states,

$$Z = \sum_{n=0}^{\infty} e^{-\beta\hbar\omega(n+\frac{1}{2})}, \tag{3.2.12}$$

and this geometric series sums up to

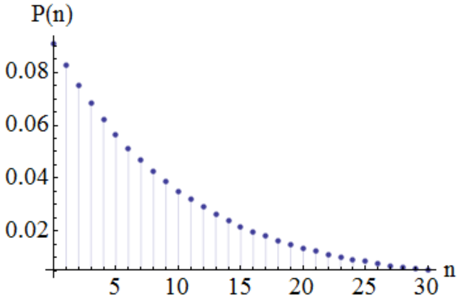

Figure 3.4: Plot of the probability for each n-state for a thermal state with $\bar{n}$=10.

$$Z = \frac{e^{-\beta\hbar\omega/2}}{1 - e^{-\beta\hbar\omega}}. \tag{3.2.13}$$

From this, we have an expression for P_n. The zero-point energy cancels and we arrive at

$$P_n = e^{-\beta\hbar\omega n}(1 - e^{-\beta\hbar\omega}). \tag{3.2.14}$$

The average number occupation $\bar{n}$ evaluates to

$$\bar{n} = \sum_{n=0}^{\infty} nP_n = \frac{1}{e^{\beta\hbar\omega} - 1}. \tag{3.2.15}$$

After some algebra, this can be used to arrive at the probability distribution for number states, which is

$$P_n = \frac{\bar{n}^n}{(\bar{n}+1)^{n+1}}, \tag{3.2.16}$$

and is plotted for $\bar{n}$=10 in Fig. 3.4.

It is not necessarily sensible to describe a single trapped ion as having a temperature T. However, we can reliably use Eq. 3.2.16 to approximate energy from a thermal expectation, such as for estimating the motional distribution following Doppler cooling on normal modes of motion.

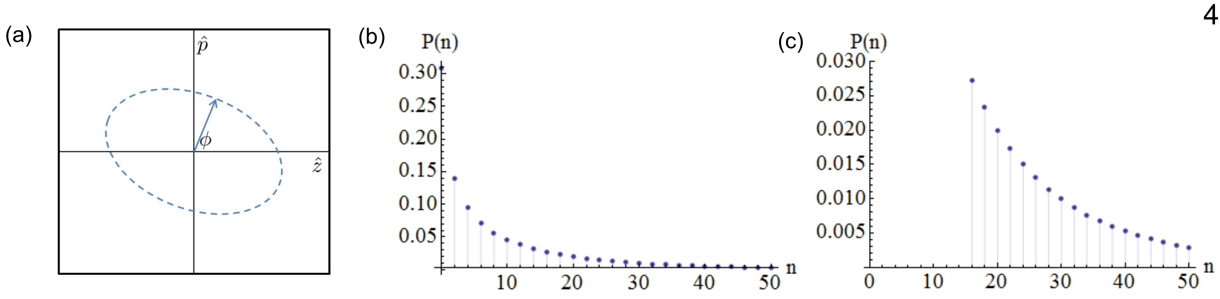

Figure 3.5: Diagram for a squeezed state of motion. (a) Phase-space depiction of a squeezed state. The state evolves with $\phi = \omega t$ as the angle with respect to the coordinate $\hat{z}$-axis. As depicted, the state along the $\hat{z}$-axis was squeezed with contraction by β_s and the $\hat{p}$-axis expanded by β_s at the start of state evolution. (b) Plot of the probability for each n-state for a squeezed state with β_s=40. (c) The same probability distribution with a factor of ten smaller vertical scale to showcase the relatively long "tail" of the distribution.

3.2.3 Squeezed Distribution

The minimum-uncertainty state of the harmonic oscillator is the ground state. The variance in both position $(\Delta z^2 = (1/m\omega)\hbar/2)$ and momentum $(\Delta p^2 = (m\omega)\hbar/2)$ clamps the distribution of position and momentum to $\Delta z^2 \cdot \Delta p^2 = \hbar^2/4$. A physical process may then "squeeze" the distribution in z, which will expand the distribution in p, and the state time-evolves with an out-of-phase breathing in the distributions of z and p in the harmonic well. The squeezed state can be characterized by a squeezing parameter β_s such that $\Delta z_s = \Delta z/\beta_s$ [58, 39]. A phase-space depiction is shown in Fig. 3.5a.

A squeezed state can be generated with a force which modulates the trapping well at 2ω (in Ref. [57], this was done with a parametric drive by two Raman beams at 90° with a frequency difference of 2ω incident on an ion initially in the state $|n=0\rangle$) and hence only even-n states will engage in the distribution. The probability distribution for even n is given by [58, 39]

$$P_n = \frac{2\sqrt{\beta_s}}{\beta_s+1}\left(\frac{\beta_s-1}{\beta_s+1}\right)^n 2^{-n}\frac{n!}{[(n/2)!]^2}. \tag{3.2.17}$$

This distribution has an exceptionally long "tail," that is, a significant occupation of number states out to large n, which is depicted in Fig. 3.5 for β_s=40.

Typically, squeezed states take parametric excitations to drive any relevant amount of population into higher n states. An instantaneous change in a trap, for example, from an initial 2 MHz confinement to a final 200 kHz confinement (which is an unrealistic situation) would lead to a squeezing parameter of $z_{0,f}/z_{0,i} = \sqrt{\omega_i/\omega_f} = \beta_s = 3.16$, and this squeezing parameter corresponds to $P_{n=0} \simeq 0.85$ ground-state occupation. Further analysis in Ref. [58] includes a description for a coherently displaced squeeze state, which adds more subtleties to the squeezed state. For example, typically, the state obtained from squeezing and then coherently displacing a state is not the same as that from coherently displacing and then squeezing the state.

3.3 Laser-Motion Interactions

3.3.1 Motional-Sideband Laser Interactions

The stimulated Raman transitions, discussed in Chapter 2, have an extremely narrow linewidth for transitions between states of the ^{9}Be$^+$ $S_{1/2}$ hyperfine manifold. The "carrier" transition, or the on-resonance transitions between hyperfine states, can be driven with either Raman beams that are co-propagating (co-carrier) or 90° from each other (90-carrier). Interactions with the ions' motion is achieved when the Raman beams are in the 90-carrier configuration and have a difference k-vector δk along the motional axis. By scanning the frequency of one or both of the laser beams, the Raman transition can resolve motional sidebands to the blue or red of the 90-carrier transition. For linewidths much narrower than the k^{th} normal mode frequency ω_k, given by Rabi rates much less than ω_k, then the carrier as well as the motional sideband resonances are spectrally resolved. By giving a relative detuning between two laser beams such that L1 has frequency $\omega_1 = \omega_i - \Delta$ and L2 has frequency $\omega_2 = \omega_i - \Delta - \omega_0 - \delta$ where $\delta = n\omega_k$, n an integer, then the beams resonantly drive a Raman transition which entangles the motion with the qubit.

To describe the Raman transitions between two levels, we start with time-independent $H_0 = H_{spin} + H_{motion} = \frac{\hbar\omega_0}{2}\sigma_z + \hbar\omega_z a^\dagger a$, with the usual Pauli spin operator σ_z. The interaction Hamiltonian is

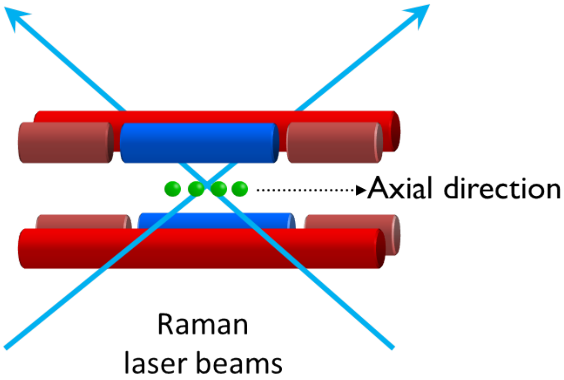
Axial direction
Raman
laser beams

Figure 3.6: Diagram of the Raman beam alignment for beams L1 and L2 with δk along the trap axis. The beams are ideally aligned to interact exclusively with normal modes along the trap axis.

$$H_I = -\bar{\mu} \cdot B, \tag{3.3.1}$$

for the coupling between the dipole moment $\bar{\mu} = \mu\bar{S}$ for spin S and the applied field $B = \hat{\varepsilon}B\cos(kz - \omega t + \phi)$ with wavenumber k and frequency ω. We assume that the field is propagating in the $\hat{z}$ direction and polarized in the $\hat{x}$ direction. Then Eq. 3.3.1 becomes

$$H_I = \frac{\hbar\Omega}{2}(\sigma_+ + \sigma_-)[e^{i(kz-\omega t+\phi)} + e^{-i(kz-\omega t+\phi)}] \tag{3.3.2}$$

where $\hbar\Omega = -\mu B/4$ and with spin operators $\sigma_+ = \frac{1}{2}(\sigma_x + i\sigma_y)$, $\sigma_- = \frac{1}{2}(\sigma_x - i\sigma_y)$, and the coordinate $z = z_0(a + a^\dagger)$.

Transforming to the interaction picture, in which $a \to ae^{-i\omega_z t}$ and $\sigma_+ \to \sigma_+ e^{i\omega_0 t}$, we take the rotating-wave approximation to get

$$H_I' = \frac{\hbar\Omega}{2}\sigma_+ \exp(i[\eta(ae^{-i\omega_z t} + a^\dagger e^{i\omega_z t}) - \delta t + \phi]) + h.c. \tag{3.3.3}$$

where $\delta = \omega - \omega_0$ is the detuning from the carrier resonance and $\eta = kz_0$ is the Lamb-Dicke parameter.

The wavefunction can be written as

$$\Psi = \sum_{s=\downarrow,\uparrow}\sum_{n=0}^{\infty} C_{s,n}(t)|s\rangle|n\rangle \tag{3.3.4}$$

for spin states $|s\rangle$, motional states $|n\rangle$, and normalized complex coefficients $C_{s,n}(t)$ for each state. For the case of on-resonance transitions $\delta = (n' - n)\omega_z$, where n' and n are integers (off-resonance transitions included in Ref. [6]), Schrödinger's equation gives the set of equations

$$\begin{aligned} \dot{C}_{\downarrow,n} &= -i^{(1-|n'-n|)} e^{-i\phi} \frac{\Omega_{n',n}}{2} C_{\uparrow,n'}, \\ \dot{C}_{\uparrow,n'} &= -i^{(1+|n'-n|)} e^{i\phi} \frac{\Omega_{n',n}}{2} C_{\downarrow,n}, \end{aligned} \tag{3.3.5}$$

which corresponds to two-level Rabi oscillations with a Rabi rate dependent on the motional interaction. The Rabi rates for these transitions are given by [59, 60, 6]

$$\begin{aligned} \Omega_{n',n} &= \Omega_{n,n'} = \Omega|\langle n'|e^{i\eta(a+a^{\dagger})}|n\rangle| \\ &= \Omega e^{-\eta^2/2}[n_<!/n_>!]^{(1/2)}\eta^{|n'-n|}L_{n_<}^{|n'-n|}(\eta^2), \end{aligned} \tag{3.3.6}$$

for driving between number states $|n\rangle$ to $|n'\rangle$ with $n_<$ the lesser and $n_>$ the greater, and Ω is the 90-carrier Rabi rate. $L_n^{\alpha}(x)$ is the generalized Laguerre polynomial defined by

$$L_n^{\alpha}(x) \sum_{m=0}^{n} (-1)^m \binom{n+\alpha}{n-m} \frac{x^m}{m!}. \tag{3.3.7}$$

The effects on the Raman transition due to the motion must be taken into consideration whenever driving transitions in the 90-carrier beam configuration. The most common cases in our experiments are to set δ to either be tuned to the first motion adding sideband, i.e., $n' = n+1$ which adds a quanta of motion, to the first motion subtracting sideband $n' = n-1$ which removes a quanta of motion, or the carrier $n' = n$; these cases are diagrammed in Fig. 3.7 to show the transitions.

3.3.2 Interactions in the Presence of Multiple Normal Modes

Driving a single-ion Raman transition in the presence of multiple ions adds extra terms to the Rabi rates due to the addition of more normal modes of motion affecting the transition. Assume that the lasers interact with the j^{th} ion in a linear chain of length N_{ions} ions. The Hamiltonian now includes the sum of each normal mode, giving

$$H_{0j} = \frac{\hbar\omega_0}{2}\sigma_{zj} + \sum_{l=1}^{3N_{ions}} \hbar\omega_l a_l^{\dagger} a_l. \tag{3.3.8}$$

with index k corresponding to each normal mode. The interaction Hamiltonian in Eq. 3.3.3 is now given by

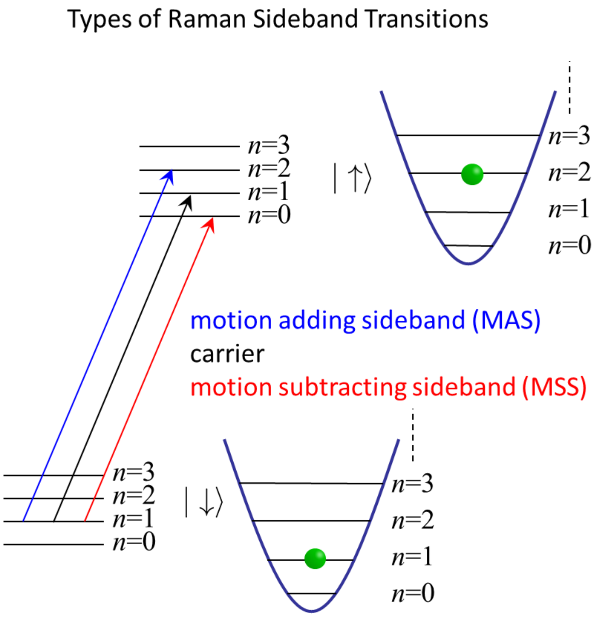
Types of Raman Sideband Transitions
n=3
n=2
n=1
n=0
|↑⟩
n=3
n=2
n=1
n=0
motion adding sideband (MAS)
carrier
motion subtracting sideband (MSS)
n=3
n=2
n=1
n=0
|↓⟩
n=3
n=2
n=1
n=0

Figure 3.7: Depiction of transitions between two spin levels for the first blue-detuned, or motion adding, sideband (adding one quanta of motion), the first red-detuned, or motion subtracting, sideband (removing one quanta of motion), and the carrier transition.

$$H'_{Ij} = \frac{\hbar\Omega}{2}\sigma_{+j}\exp(i[\sum_{l=1}^{3N_{ions}}\eta_l^j(a_l e^{-i\omega_l t} + a_l^\dagger e^{i\omega_l t}) - \delta t + \phi]) + h.c., \tag{3.3.9}$$

where the interaction now contains a sum over terms with the Lamb-Dicke parameters and frequencies for each mode. The interaction is therefore affected by every normal mode, and this gives rise to a Rabi rate for resonant transitions between states $|\downarrow, n_k\rangle$ and $|\uparrow, n'_k\rangle$ of [6]

$$\Omega_{n'_k,n_k} = \Omega|\langle n_{p\neq k}, n'_k| \prod_{l=1}^{3N_{ions}} e^{i\eta_l^j(a_l+a_l^\dagger)}|n_{p\neq k}, n_k\rangle|. \tag{3.3.10}$$

The "spectator" modes $p \neq k$ contribute multiplying factors to the driven sideband (often referred-to as Debye-Waller factors) given by Eq. 3.3.6. In the case of our 90° Raman beam configuration, ideally there are only interactions along the $\hat{z}$-axis of the trap reducing the contributions from $3N_{ions}$ modes to only N_{ions} modes.

Typically our beam waist is $\sim$30 μm, too large to only address a single ion in a same-species chain (on the order of a $5-10\mu$m-long chain). In the case of Rabi oscillations on multiple ions, the dynamics are more complicated due to the multiple spins interacting with individual modes as in Ref. [54]. In the case of two ions, and in the regime where $\eta_1, \eta_2 \ll 1$ (the Lamb-Dicke regime), the first sideband transition is

$$\Omega_{n1',n1}(n_2) \simeq \Omega\eta_1\sqrt{n_{1>}}e^{-(\eta_1^2+\eta_2^2)/2}(1-n_2\eta_2^2) \tag{3.3.11}$$

for a sideband transition on mode 1 with spectator mode 2.

3.3.3 Doppler Cooling on Normal Modes

In Chapter 2, I described Doppler cooling to reduce the net kinetic energy of ions. Our Doppler cooling beam is not aligned purely along any one trap axis, thereby allowing laser cooling in all trap directions. Once an ion is confined, the average energy achieved from Doppler cooling leaves the ion in a thermal distribution of number states set by the Doppler cooling limit. From Chapter 2 Eq. 2.3.5, the Doppler cooling limit for the $\hat{z}$-direction was given by

$\omega/2\pi$ (MHz)	$\bar{n}_{limit}$	Axis
12.26	0.54	$\hat{x}$
11.19	0.62	$\hat{y}$
2.69	2.59	$\hat{z}$

Table 3.2: Doppler-cooling limits $\bar{n}_{limit}$ for each axis when ^{9}Be$^+$ is Doppler cooled on a transition with a linewidth of $\Gamma \simeq 2\pi \times 19.4$ MHz, where the incident light is σ^+-polarized and in the direction $\hat{k} = \frac{\hat{x}+\hat{y}+\sqrt{2}\hat{z}}{2}$.

$$k_B T_{min} = \frac{\hbar\Gamma\sqrt{1+I/I_{sat}}}{4}(1+\frac{f_{si}}{f_i}) \tag{3.3.12}$$

with $f_i = 1/2$ and $f_{si} = 7/20$ for a σ^+-polarized beam that lies along our external magnetic field aligned 45° to the trap axis.

Generally, the concept of temperature only applies to particles in contact with some thermal reservoir. However, Doppler cooling prepares the motion in a thermal state [40, 36], and Eq. 3.2.15 gives us $\bar{n}$ for the normal mode with frequency ω given $k_B T_{min}$ after Doppler cooling. An example calculation for the average motional occupations along the axial and radial directions for a ^{9}Be$^+$ ion are shown in Table 3.2, assuming $\hat{r}$ breaks into $\hat{x}$ and $\hat{y}$ directions such that $\hat{k} = \frac{\hat{x}+\hat{y}+\sqrt{2}\hat{z}}{2}$ and that $f_{x,y} = 1/4$. In reality, as the radial direction's $\hat{x}$ and $\hat{y}$ components are not always perfectly known with respect to the beam direction, the Doppler cooling limit may be different than calculated between the two directions.

3.3.4 Sideband Cooling of Normal Modes

When entangling two ions, we use the normal modes of motion as an information bus to entangle two ions in a shared trap. It is typically best to prepare the normal modes of motion near the $|n = 0\rangle$ ground state. After Doppler cooling, we accomplish this ground-state cooling through Raman sideband cooling [61, 54]. A cycle of sideband cooling begins with a motion subtracting sideband (MSS) to remove a quantum, followed by optical repumping, which for $\eta \ll 1$ incoherently performs a carrier-like transition on the ion back to the initial state. For ^{9}Be$^+$, we drive the $|F =$

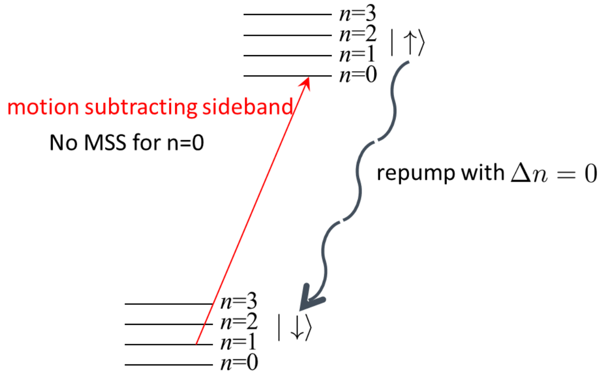

Figure 3.8: Diagram of the Raman sideband cooling process on a single mode of motion. First a motion subtracting sideband pulse is applied to the initial state $|\downarrow\rangle$, for us the ^{9}Be$^+$ $|2,2\rangle$ state, to drive the transition $|\downarrow,n\rangle \rightarrow |\uparrow,n-1\rangle$ where $|\uparrow\rangle$ in our case is the ^{9}Be$^+$ $|1,1\rangle$ state. This is followed by applying our repumping beams for $10-30\mu$s to dissipate the ions' internal energy and perform a carrier-like transition. Many repetitions of this process prepare the ion near the $|n=0\rangle$ state of motion.

$2, m_F = 2, n\rangle \rightarrow |F = 1, m_F = 1, n-1\rangle$ transition on the MSS. Then, our repumping beams are applied for $10-30\mu$s to return to the $|2,2\rangle$ initial state without a significant change in the motion, which is like an incoherent carrier transition on $|1,1\rangle \rightarrow |2,2\rangle$. This dissipates the motional energy (diagrammed in Fig. 3.8). After repeated applications, when most of the motional occupation is prepared in the $|n=0\rangle$ motional state, the motion subtracting sideband will no longer be able to drive the transition $|F=2, m_F=2, n\rangle \rightarrow |F=1, m_F=1, n-1\rangle$ as there is no motional state lower than the $|n=0\rangle$ state.

As each normal mode of motion for the trapped ions is in a thermal state following Doppler cooling, even a low $\bar{n}_k$ on mode k will have motional occupation of higher $|n\rangle$ states. Therefore, it requires many applications of the Raman sideband cooling cycle. Since there is a different Rabi rate $\Omega_{n-1,n}$ for each number state given by Eq. 3.3.10, it is most efficient to vary the duration of the motion subtracting sideband pulses by $\tau_{n-1,n} = \pi/\Omega_{n-1,n}$ for each Raman cooling cycle. Plots of the cooling pulse durations and the Rabi rates are given in Fig. 3.9 to show how the pulse durations vary when considering a single normal mode. Photon recoil from repumping and heating rates prevent perfectly achieving the $|n=0\rangle$ state. However, for example, motion in a starting thermal

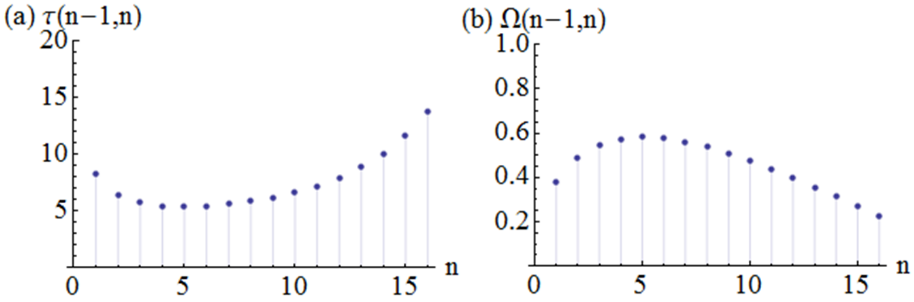

Figure 3.9: Plot of (a) Rabi π-times and (b) Rabi rates for different number states n taking Ω=1. These plots assume 313 nm light for the Raman transitions on ^{9}Be^{+} in a trap with $\omega = 2\pi\times$2.69 MHz for the axial normal mode frequency and $\eta \simeq 0.41$. The fastest π-time occurs for $n = 5$.

state of $\bar{n} = 3$ after Doppler cooling, applying $\sim$20 cooling cycles will be sufficient to ground-state cool a single ion to $\bar{n} \simeq 0.1$ quanta.

3.4 Analyzing Motional States

Driving Rabi oscillations on a motional sideband, which entangles motion and qubit, and measuring the qubit state as a function of pulse duration will allow observation of the probability distribution the driven normal mode. For a single ion initialized in the state $|\downarrow, n\rangle$, the Rabi oscillations take the form

$$P_{\downarrow}(t) = |\cos(\Omega_{n',n}t)|^2 = \frac{1}{2}[1+\cos(2\Omega_{n',n}t)] \tag{3.4.1}$$

with $\Omega_{n',n}$ given by Eq. 3.3.6. In general, the motion will be in a distribution of motional states, in which case the Rabi oscillations take on a beat-note signal due to interference of Rabi rates from multiple n-states. The Rabi oscillations are then [57, 6]

$$P_{\downarrow}(t) = \frac{1}{2}\left[1+\sum_{n=0}^{\infty} P_n \cos(2\Omega_{n',n}t)\right], \tag{3.4.2}$$

where P_n is the probability of the ion being in the state $|n\rangle$. A Fourier analysis of this signal yields the probability distribution of the $|n\rangle$ states. An example of analyzing the Rabi oscillations for a

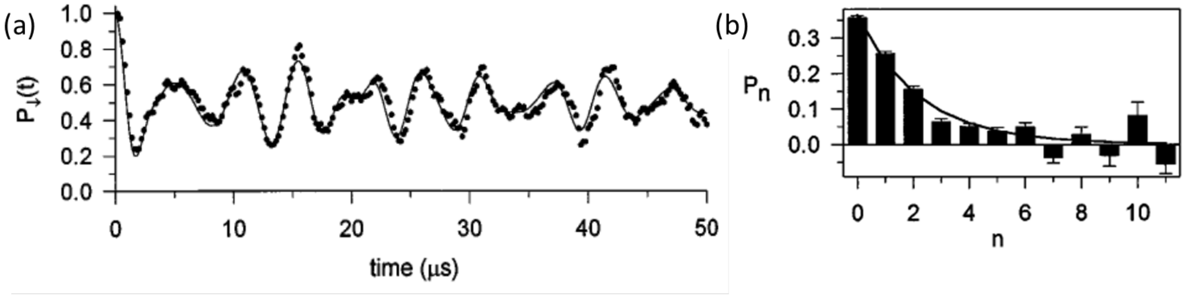

Figure 3.10: Rabi flopping trace for a thermal state of motion with $\bar{n} = 1.3 \pm 0.1$ and $\eta = 0.202$ for a single ^{9}Be$^+$ ion driving on the first motion adding sideband. (a) The Rabi oscillations are shown with distinct interference in the signal due to a distribution of number states. (b) The distribution of number states extracted from the Rabi oscillations. Figures reproduced from Ref. [57].

single ion in a thermal state of motion with $\bar{n} = 1.3$ is shown in Fig. 3.10 from the work in Ref. [57] (in which coherent, thermal, and squeezed states were all observed through the sideband Rabi oscillations on a single ^{9}Be$^+$ ion). Typicall for small values of $\bar{n} \lesssim 0.1$, it is difficult to distinguish between a thermal and coherent distribution.

When there are multiple modes of motion, the Rabi oscillations include terms from all normal modes. Then, the Rabi oscillation signal becomes

$$P_\downarrow(t) = \frac{1}{2}\left[1 + \prod_{l=1}^{3N_{ions}} \sum_{n_l=0}^{\infty} P_{n_l} \cos(2\Omega |\langle n_{p\neq k}, n'_k| \prod_{l=1}^{3N_{ions}} e^{i\eta_l(a_l + a_l^\dagger)} |n_{p\neq k}, n_k\rangle| t)\right], \tag{3.4.3}$$

where the terms in Eq. 3.4.2 for $\Omega_{n',n}$ have been replaced by the multi-mode case in Eq. 3.3.10 and the sum over probability P_n has been replaced by a sum over all products for each probability of the ion being in the state $|n_l\rangle$ for each normal mode l. For a specific situation, the Rabi oscillations for a Raman transition in the 90-carrier configuration on a ^{9}Be$^+$-^{25}Mg$^+$ ion chain's axial modes is given by

$$P_\downarrow(t) = \frac{1}{2}\left[1 + \sum_{n=0}^{\infty}\sum_{m=0}^{\infty} P_n P_m \cos(2\Omega |\langle m, n'| e^{i\eta_m(a_m + a_m^\dagger)} e^{i\eta_n(a_n + a_n^\dagger)} |m, n\rangle| t)\right], \tag{3.4.4}$$

where number states $|n\rangle$ and $|m\rangle$ are for the two normal modes of motion (the in-phase $INPH$ mode and out-of-phase $OOPH$ mode) with respective populations P_n and P_m, and for a sideband

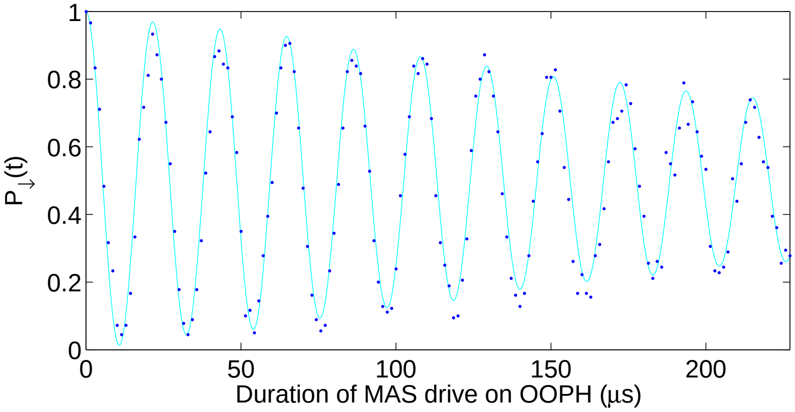

Figure 3.11: Rabi flopping trace from driving on the out-of-phase normal mode of a ^{9}Be$^+$-^{25}Mg$^+$ ion pair. Here the Lamb-Dicke parameters are [η_{INPH}, η_{OOPH}]=[0.16, 0.27] and the curve fits to a thermal distribution of [$\bar{n}_{INPH}$, $\bar{n}_{OOPH}$]$\simeq$[0.34, 0.01]. Histograms were collected from ion fluorescence many times, which were used to construct the Rabi oscillation trace.

transition on the mode with states $|n\rangle$, with $n' = n+1$ for the MAS, $n' = n-1$ for the MSS, or $n' = n$ for a carrier transition, while the mode with states $|m\rangle$ is a spectator mode. An example is given in Fig. 3.11 for a motion adding sideband oscillation curve performed on a ^{9}Be$^+$-^{25}Mg$^+$ ion chain.

A shortcut for analyzing a thermal state of motion takes advantage of the convenient form of P_n for a thermal state. If it is known that the ion is in a thermal state, such as after Doppler cooling, then observing both the motion adding and subtracting sidebands can be used to quickly extract $\bar{n}$ for the thermal state. For a drive time t_d on-resonance with the sideband, the state evolves to

$$\begin{aligned} P_{\downarrow}^{MSS} &= \sum_{n=1}^{\infty} P_n \cos^2(2\Omega_{n-1,n} t_d) \\ P_{\downarrow}^{MAS} &= \sum_{n=0}^{\infty} P_n \cos^2(2\Omega_{n+1,n} t_d), \end{aligned} \tag{3.4.5}$$

with $P_n = \frac{\bar{n}^n}{(\bar{n}+1)^{n+1}}$ from Eq. 3.2.16. Then, taking the ratio gives

$$R = \frac{\sum_{n=1}^{\infty} \frac{\bar{n}^n}{(\bar{n}+1)^{n+1}} \cos^2(2\Omega_{n-1,n} t_d)}{\sum_{n=0}^{\infty} \frac{\bar{n}^n}{(\bar{n}+1)^{n+1}} \cos^2(2\Omega_{n+1,n} t_d)}. \tag{3.4.6}$$

Factoring out $\frac{\bar{n}}{\bar{n}+1}$ from the numerator and shifting the sum, we then have

$$R=\frac{\bar{n}}{\bar{n}+1}\frac{\sum_{n=0}^{\infty}\frac{\bar{n}^n}{(\bar{n}+1)^{n+1}}\cos^2(2\Omega_{n,n+1}t_d)}{\sum_{n=0}^{\infty}\frac{\bar{n}^n}{(\bar{n}+1)^{n+1}}\cos^2(2\Omega_{n+1,n}t_d)}=\frac{\bar{n}}{\bar{n}+1}, \tag{3.4.7}$$

and thus

$$\bar{n}=\frac{R}{1-R} \tag{3.4.8}$$

for a thermal state. This only requires comparing the initial-state fluorescence to the fluorescence after the sideband drives on a single ion. This ratio method also works in the presence of other normal modes, as the Debye-Waller factors will cancel.

3.5 Sympathetic Cooling with ^{24}Mg$^+$ and ^{25}Mg$^+$

Laser-cooling the ^{9}Be$^+$ qubit-ions disrupts the qubit state of ^{9}Be$^+$, and so during sequences of two-qubit entanglement, it is necessary to be able to cool the ions' motion without disrupting the qubit states. One solution to this problem is through "sympathetic cooling," where laser cooling is applied to "coolant ions" to cool the shared motion in a trap with both coolant and qubit ions [6, 62]. By using another ion species with resonant wavelengths far-detuned from those of ^{9}Be$^+$, laser-cooling can be applied to the ion chain without disrupting qubit states.

We sympathetically cool with either ^{24}Mg$^+$ or ^{25}Mg$^+$ as the coolant ion, which have resonant transitions at 280 nm, far from the ^{9}Be$^+$ transitions at 313 nm. For the work in this thesis, Doppler cooling was applied to Mg$^+$ coolant ions, though Raman sideband cooling with ^{24}Mg$^+$ was instrumental as part of the method sets for work in Refs. [55, 29, 27, 28] before each entanglement operation between qubits in a shared trap zone. Entanglement in the presence of dissipation, where the dissipation was partially engineered by sympathetic cooling on ^{24}Mg$^+$, was demonstrated in Ref. [63]. Sympathetic cooling using an electromagnetic-induced-transparency effect to suppress motion-adding interactions while driving motion-subtracting interactions was demonstrated in Ref. [63] and described theoretically in Ref. [64]. We demonstrated this electromagnetic-induced-transparency cooling by sympathetic cooling on a ^{9}Be$^+$-^{24}Mg$^+$ ion pair to $\bar{n}_{INPH}\simeq 0.15$

and $\bar{n}_{OOPH} \simeq 0.08$ in 85μs, and this method could potentially reduce the temporal overhead for ground-state cooling in future work with scalable QIP.

The ^{24}Mg^{+} atomic structure has no hyperfine splitting, and the $S_{1/2}$ states $m_J = 1/2$ and $m_J = -1/2$ are split by ~334 MHz at an external magnetic field of $B = 11.964$ mT. The next lowest orbital states are the $P_{1/2}$ and $P_{3/2}$ states, which have a fine structure splitting of ~2.75 THz [65], which are coupled to the S states by 280 nm laser light. Doppler cooling is achieved with laser light at 280 nm red-detuned from the transitions $|S_{1/2}, m_J = -1/2\rangle \longleftrightarrow |P_{1/2}, m_J = 1/2\rangle$ with σ^{+}-polarized light and $|S_{1/2}, m_J = 1/2\rangle \longleftrightarrow |P_{1/2}, m_J = 1/2\rangle$ with π-polarized light. Both beams are necessary, as there is no closed two-level cycling transition between $S_{1/2}$ and $P_{1/2}$ at non-zero external magnetic field. These transitions have a linewidth of $\Gamma \simeq 2\pi \times 41$ MHz, and so optimal Doppler cooling occurs with a beam detuned from $|P_{1/2}, m_J = 1/2\rangle$ on the order of $-\Gamma/2 \simeq -2\pi \times 20.5$ MHz. However, a "dark state" can arise due to a coherent process from interference between the two cooling beams when they are at the same detuning from the $P_{1/2}$ state [42], so an offset of ~ 10 MHz detuning is used between the beams. Doppler cooling on ^{24}Mg^{+} is covered extensively in Ref. [14], including dark state analysis.

The ^{25}Mg^{+} atomic structure does have a hyperfine splitting due to the nuclear spin of $I = 5/2$, splitting the $S_{1/2}$ manifold into two hyperfine levels $F = 2$ and $F = 3$. A benefit to ^{25}Mg^{+} is that at the external magnetic fields for a field-insensitive qubit in ^{9}Be^{+} at $B = 11.945$ mT, the ^{25}Mg^{+} hyperfine states $|S_{1/2}, F = 3, m_F = 1\rangle$ and $|S_{1/2}, F = 2, m_F = 0\rangle$ are split by 1763.18440809 MHz and form a near-field-insensitive qubit that could possibly be used as a qubit in future experiments. The hyperfine levels at our typical external magnetic field values have a closed two-level cycling transition for Doppler cooling, achieved by σ^{+}-polarized light that drives the $|S_{1/2}, F = 3, m_F = 3\rangle \longleftrightarrow |P_{3/2}, F = 4, m_F = 4\rangle$ transition with 280 nm light. The linewidth for this transition is $\Gamma \simeq 2\pi \times 41$ MHz, so optimal Doppler cooling is achieved with a detuning by $-\Gamma/2 \simeq -2\pi \times 20.5$ MHz from the transition. The beam for far-detuned Doppler cooling is $\sim$ -500 MHz red-detuned from the $S_{1/2}$ to $P_{3/2}$ transition.

Chapter 4

Apparatus

This chapter describes the apparatus for running our experiments. The key apparatus components include multi-electrode ion traps, a vacuum-containment system for the traps, and optics for laser beam control. To carry out our scheme for scalable quantum information processing, the traps are designed with multiple electrodes that can be used to create many spatially distinct trap regions for ion confinement [8]. We have two wafer traps in which the ion transport experiments described in this thesis have been carried out: the "quantum logic trap" with up to 6 trap zones and the "X-junction trap" with up to 18 trap zones, each with similar electrode size-scales. To interact with the ions, up to six laser sources, many servo loops to stabilize laser intensity and position, and pulse-shaped microwaves are incident on one or more trap regions to drive atomic transitions. We have the capability to trap both ^{9}Be$^+$ and ^{24}Mg$^+$ (in the quantum logic trap) or ^{9}Be$^+$ and ^{25}Mg$^+$ (in the X-junction trap) in a shared trap zone for sympathetic cooling. This chapter will highlight the most important components and technical details which the apparatus comprises. Much of the work in this thesis was carried out in the quantum logic trap, though the relevant apparatus is extensively covered in Ref. [14]. As of this thesis, experiments are carried out with the X-junction trap, and this chapter focuses on the most current apparatus setup. First, I will describe the multi-electrode ion traps. Then I will describe the vacuum containment system, including hardware for loading ions. I then describe magnetic field coils and imaging system, which are external to the vacuum system. Lastly, I describe and diagram our laser beam setup for the ion-laser interactions.

4.1 Multiple Electrode Wafer Trap

To produce a multi-electrode trap, the idealized rod electrodes described in Chapter 3 can be replaced with wafers that have conducting material deposited on insulating surfaces. The traps described here were fabricated from wafers made out of laser-machined alumina sputter-coated with gold to form electrode surfaces [12]. Electrode details for both RF and DC electrodes were first machined into the wafer surfaces with an excimer laser. The minimum size for electrode features is set by the excimer laser's minimum focus size, which at the time of construction was 20 μm. A slot was also machined into each wafer, which allows optical access to the trapping region. Next, a titanium adhesion layer was laid down on the electrode features and then sputter-coated with gold on top of the adhesion layer. The deposition process produces a surface layer of conducting traces over the machined alumina, and this process is repeated on both sides of the wafer to produce the trap electrodes. Thorough descriptions of wafer trap fabrication method can be found in Refs. [12, 50, 14]. Here, I will focus on the geometry features that are important in ion transport experiments.

Wafer traps have been used for many experiments to demonstrate the building blocks for scalable ion-based QIP. Early work with multi-electrode ion traps involving transport led the way to improved electrode geometries. For instance, transport and separation of ions in a wafer trap was first demonstrated in Ref. [12], where it was shown that ion transport can be achieved with little motional excitation. However, the separation, or splitting, of two ions from a single trap led to significant motional excitation. For the work in Ref. [22], a trap was designed with a relatively smaller electrode structure, as compared to the electrode sizes and ion spacings in the trap in Ref. [12]. The new trap enabled greatly reduced motional excitation during separation, which was attributed to separating the ions over a smaller DC electrode that acted as a narrow wedge. Another improvement was based on a complication reported by Ref. [24], in which it was shown that when loading ions into the trap, stray ^{9}Be$^+$ could coat electrode surfaces and could contribute to ambient heating rates of the ion's motion. A mask was put in place in the trap of Ref. [12] to shield the trap electrodes of the experimental zone during ion loading and thus mitigated metal deposition which in turn led to a reduction in motional excitations. Other negative motional effects come from electric field noise on the electrode surfaces [24]. Electrically filtering the potentials applied to DC electrodes reduces noise levels that contribute to ambient heating rates of the trapped ion's motion. All of these improvements were incorporated into subsequent wafer designs in the traps used for the work described in this thesis.

4.2 Trap Geometries

4.2.1 Quantum Logic Trap

A multizone two-wafer trap, designed by M. Barrett and fabricated by J. Jost [14], was designed to be used to demonstrate the basic building blocks for scalable QIP in a multizone trap array. This trap is designated the "quantum logic trap." The quantum logic trap was used for several experiments to demonstrate scalable techniques for QIP, which include the demonstration of field-independent qubits with ^{9}Be$^+$ [35], entangling two separate mechanical oscillators [55], and experiments combining ion transport with quantum logic to demonstrate method-sets for a two-qubit quantum processor [29, 27, 28]. A photo of the quantum logic trap is shown in Fig. 4.2.1. This is the trap used for transport work in Ref. [66].

The quantum logic trap is composed of wafers with eight pairs of diagonally-opposite, segmented DC electrodes and a pair of diagonally-opposite RF electrodes. In-depth schematics of the electrode dimensions are contained in Ref. [14]. The spacing between each DC electrode segment on a single wafer is set by the minimum machining width of 20 μm. Each wafer has a laser-machined slot cut out of it for laser access to the trapping region between the two wafers. The narrow section of the RF-to-DC slot is 200 μm wide and is designated as the experiment region. Experiments are principally carried out in two different "interaction" zones, zones with laser access to address qubit-ions, which are located over 200 μm wide electrodes surrounding a narrow 100 μm wide "separation" electrode. The two zones provide confinement 370 μm apart, symmetric about

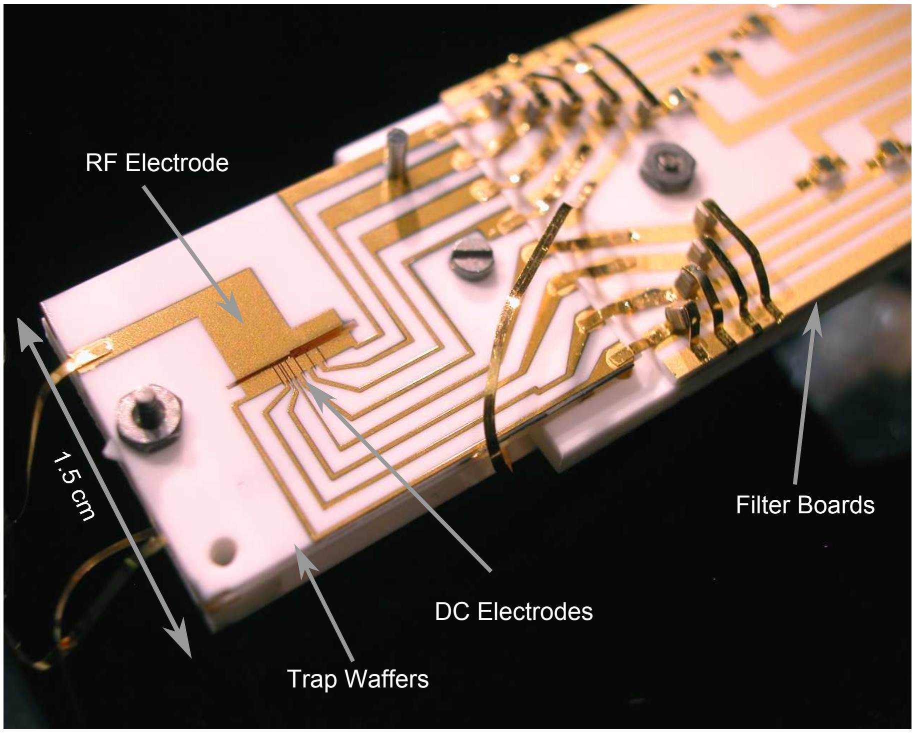
RF Electrode
1.5 cm
DC Electrodes
Trap Waffers
Filter Boards

Figure 4.1: Multizone wafer linear RF Paul trap, the “quantum logic trap.” Two trap wafers, each with segmented electrodes, are mounted together to form parallel planes spaced 200 μm apart. The trap has gold electrodes deposited on laser-machined alumina wafers. The wafers are attached to a filter board that electrically filters the DC potentials applied to the DC electrodes.

the separation electrode. The relevant dimensions are shown in a model of the trap in Fig. 4.2. Ions transported between interaction zones traverse the separation electrode, which is so-named as it is used to apply a separation “wedge” potential between ions to separate ions apart into distinct trap zones. The width of the separation wedge was limited by laser machining capabilities at the time of construction. In the wider portion of the slot, designated as the load region, the RF-to-DC slot is 400 μm wide. The slot is wider and displaced from the experiment region to help mitigate deposition of metal onto the experiment-electrode surfaces during loading.

The trap wafers are attached to filter boards to reduce electric field noise on the DC electrodes (one of the filter boards is visible in Fig. 4.2.1). Each DC electrode has a corresponding trace on the filter board with a low-pass RC filter, so that externally-applied potentials have been filtered to reduce noisy fields and thus reduce ambient motional heating effects. The filters comprise an 820 pF capacitor to RF ground and a 240 Ω resistor. These filters have a corner frequency of $1/2\pi RC$ $\sim$800 kHz to filter high frequency noise near the trap axial frequency. External to the vacuum system, there is additional filtering by two in-series RC filters with corner frequencies of ~ 200 kHz, each with a 1 nF capacitor to RF ground and an 820 Ω resistor. The DC potentials, in the range of -10 V to +10 V, can maintain confinement in the axial direction with $\omega_z/2\pi \approx 2.7$ MHz for a single ^{9}Be$^+$ ion. In this trap, a typical axial heating rate for a single ^{9}Be$^+$ ion is $\dot{n} \sim 0.5$ quanta/ms. A model in Fig. 4.3 illustrates the relative positions of a two-ion crystal along the trap axis between the two trap wafers.

The radial confinement is provided by RF applied to the RF electrodes. The RF is supplied by an external signal generator producing $\sim$1.5 W of RF power that is inductively coupled to a quarter-wave coaxial resonator made of copper. The resonator has $Q \sim 300$ and a resonant frequency of 150 MHz. The RF electrode potential has $\sim$180 V peak amplitude. The RF parameters used in the lab generate a pseudopotential with $\omega_r/2\pi \approx 11$ MHz radial frequency for a single ^{9}Be$^+$ ion.

The side-view dimensions of the wafers are shown in Fig. 4.4, which includes additional alumina wafers. The trap wafers are both 125 μm thick and spaced apart by 200 μm with by alumina spacers. As the experiment region’s slot is also 200 μm, the trap electrodes form a symmetric ge-

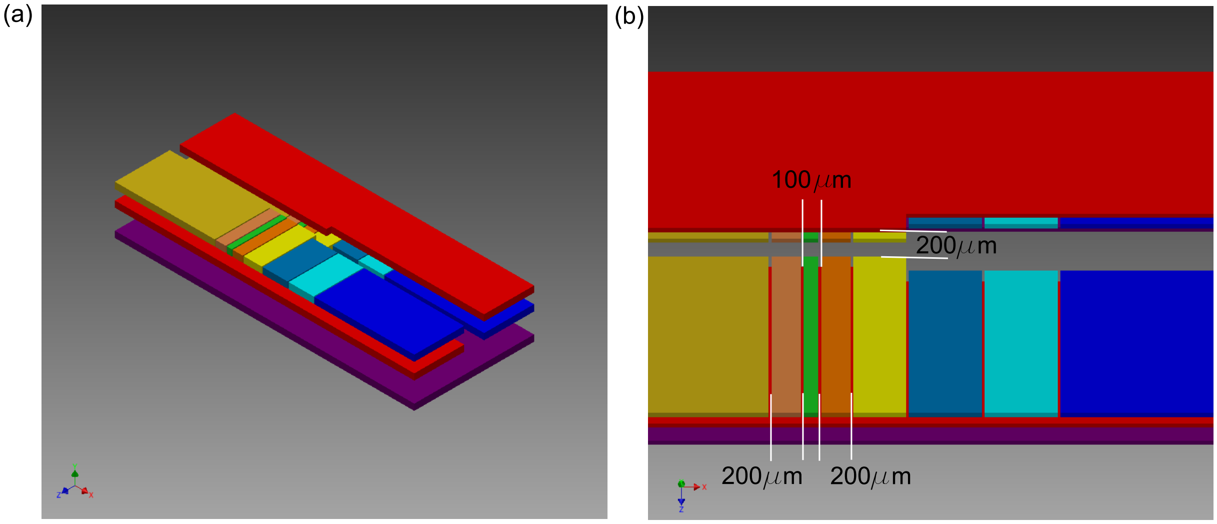

Figure 4.2: A model of the electrodes for the quantum logic trap. (a) Model of the trap showing the diagonally opposite segmented-DC electrodes, RF electrode (red), and biasboard (purple) in the quantum logic trap. The electrode wafers are spaced by 200 μm, and the biasboard is 400 μm from the bottom of the trap electrode wafers and is used to produce a uniform bias field orthogonal to the trap axis. (b) Dimensions for the experiment region. The slot between the DC electrodes and the RF electrode on each wafer is 200 μm in the "experiment" region and 400 μm in a wider "load" region. The DC electrodes are spaced diagonally apart by $\sim$280 μm. The wafers have diagonally opposite DC and RF electrodes to trap ions with a similar geometry to the idealized rod trap design discussed in Chapter 3.

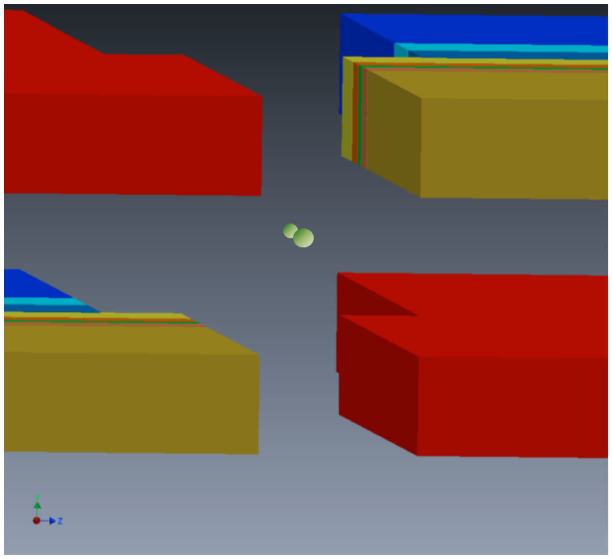

Figure 4.3: A close-up model of the trap wafers in the quantum logic trap. It illustrates where ions would be trapped along the trap axis (not to scale) between the two trap wafers.

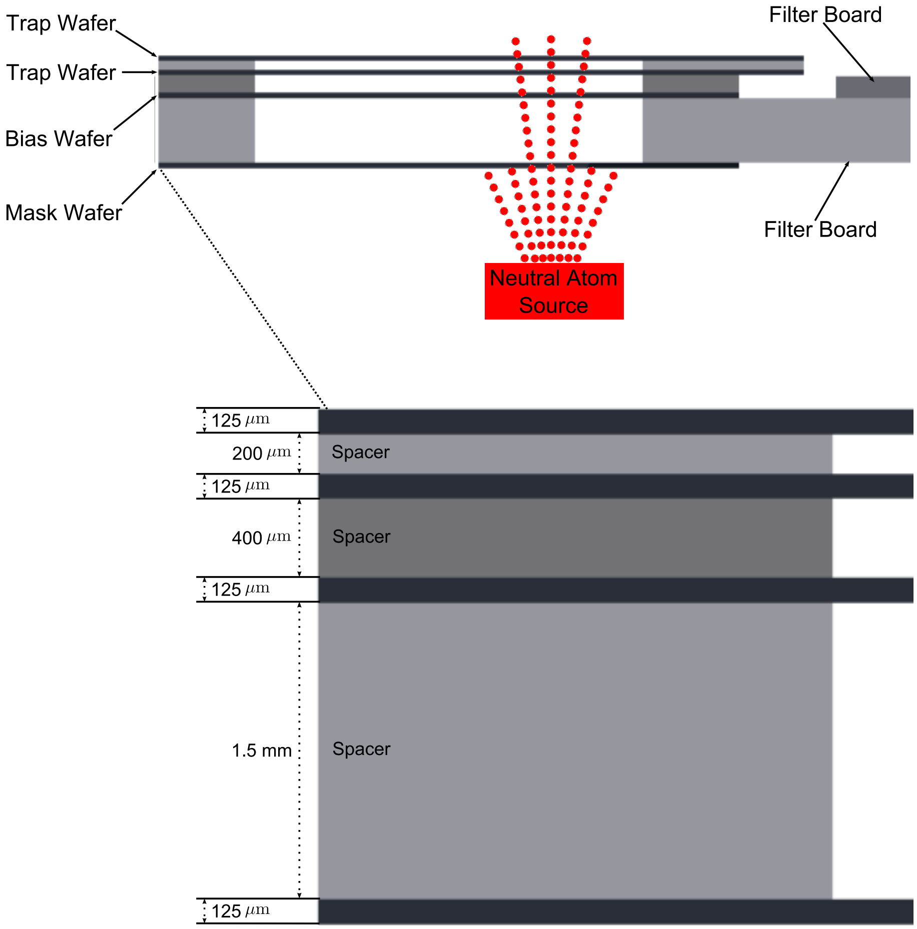
Trap Wafer
Trap Wafer
Bias Wafer
Mask Wafer
Filter Board
Filter Board
Neutral Atom Source
125 μm
200 μm
Spacer
125 μm
400 μm
Spacer
125 μm
1.5 mm
Spacer
125 μm

Figure 4.4: Schematic of the side view of the quantum logic trap. The spacer material is made from alumina. The bias wafer provides a source of global bias fields in the trap. A neutral atom source emits atoms towards the load region. The load region is spatially displaced from the experiment regions and the neutral atom source is partially blocked by a mask wafer to prevent deposition on experiment electrodes. Ionizing radiation is incident on the neutral atoms; once ionized, the atoms can be trapped in the load zone.

ometry around the trap axis. Another wafer, the biasboard wafer, is spaced 400 μm below the trap wafers. It has a large surface electrode designed to generate a uniform bias shim across the trap, largely orthogonal to the trap axis. When loading ions, a neutral atom source sends a flux of atoms through the gap in the wafers. There is a mask wafer 1.5 mm beneath the bias-board wafer, with a large electrode typically held at RF ground, primarily used to block incident neutral atoms or ions from depositing on the experiment electrodes during loading, but to still allow laser beams to pass through the load region.

4.2.2 X-junction Trap

The "X-junction trap" was designed to demonstrate transport reliably through a junction with low motional excitations [67, 15], which is important for re-ordering ions in a scalable QIP multi-electrode geometry. This X-junction trap was constructed with the same methods described in the previous section. It was designed and built by R. B. Blakestad [50]. A photo of the X-junction trap is shown in in Fig. 4.5. As of this thesis, it is also being used in work towards demonstrating scalable QIP and fast transport experiments.

The X-junction trap is formed from two wafers with a total of 46 DC electrodes (Fig. 4.6). In-depth details of the design and geometry are found in Ref. [50]. There is an X-shape machined into the wafers to form a junction. Inside the junction, there are three exits. The exits to the left and right of the junction lead to two experiment regions with similar electrode geometry to each other, each allowing two convenient spatially-distinct ion-laser interaction zones and a separation electrode. These regions are designated E (experiment) and H (horizontal). The final exit is the region designated V (vertical); this zone does not contain a separation electrode. In both experiment regions, there are pairs of 200 μm electrodes surrounding a 100 μm separation electrode as in the quantum logic trap. Additional relevant electrode geometry includes the vertical region, which has two 200 μm electrodes, and within the junction which is surrounded by two 100 μm-width DC electrodes per wafer. In the experiment and vertical regions, the wafer RF-to-DC slot is 200 μm. A load zone is connected to E through a 45° arm with a 300 μm slot width.

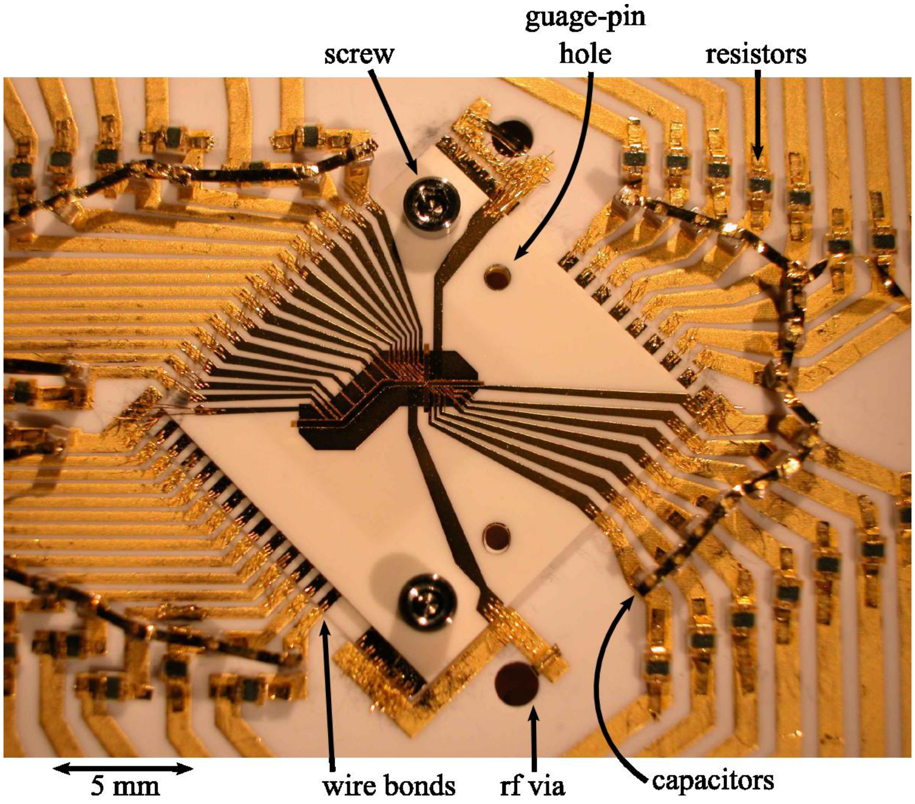
guage-pin
hole
screw
resistors
5 mm
wire bonds
rf via
capacitors

Figure 4.5: Multizone, balanced-geometry wafer trap, the "X-junction" trap. Two wafers, each with segmented electrodes, are mounted together to form parallel planes spaced 250 μm apart. The trap has gold electrodes deposited on laser-machined alumina wafers. The wafers are attached to a filter board that electrically filters the DC potentials applied to the DC electrodes.

A trapped ^{9}Be$^+$ ion has an axial frequency of $\omega_z/2\pi \approx 3.6$ MHz. The two interaction trap zones in the E and H regions provide confinement 340 μm apart about the separation electrode. The DC electrodes, as in the quantum logic trap, are connected to external potentials through a filter board, which can be seen in Fig. 4.5. The filter board has the same RC components as in the quantum logic trap's filter board, with an 820 pF capacitor to RF ground and a 240 Ω resistor giving a corner frequency of ∼800 kHz. An additional external RC filter applied to DC potentials has a 1 nF capacitor and a 1 kΩ resistor, giving a corner frequency of ∼160 kHz. In this trap, a typical axial heating rate for a single ^{9}Be$^+$ ion is $\dot{n} \sim 0.2$ quanta/ms.

The various wafers to form the X-junction trap are similar to that of the quantum logic trap, but the spacings differ somewhat. The trap wafers are 125 μm thick. The electrode wafers are displaced by a 250 μm alumina spacer. When higher order terms in trap potential were evaluated, R. B. Blakestad found it beneficial to use a larger wafer spacing relative to the DC-to-RF slot to more closely approach a perfect quadrupole. This wafer geometry is referred to as a balanced two-wafer geometry. There is a biasboard wafer to produce shim bias fields, seen as the rectangular back-plane with a large slot comparable to the size of the trap wafers in Fig. 4.6. The biasboard wafer is spaced from the trap wafers by a 500 μm alumina spacer. The alumina spacer between the bottom trap wafer and the biasboard has a surface that extends beyond the trap wafer region to also serve as the filter board. Instead of an attached mask wafer like in the quantum logic trap, there is a stainless-steel shield (not shown) to shield the experiment regions from the neutral atom sources during loading.

Each wafer has RF electrodes diagonally opposite from each other across the junction. The RF electrodes on a single wafer are connected to form a continuous conductor via a 70 μm wide bridge. This bridge is necessary for maintaining a confining pseudopotential inside the junction. A quarter-wave coaxial resonator made of copper delivers RF to both of the RF electrodes. The resonator has a loaded $Q \sim 42$ and a resonant frequency of 83 MHz. For better spectral purity, an external half-wave helical resonator is in series with the coaxial resonator with a $Q \sim 145$ for superior signal filtering on the applied RF to reduce motional excitations, particularly when traversing the

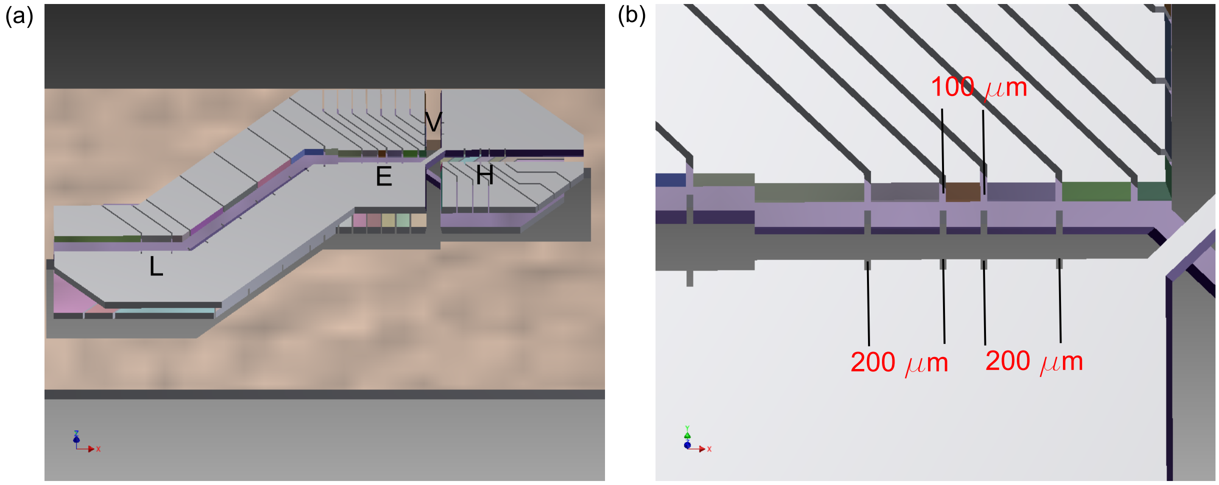

Figure 4.6: A model of the electrodes for the X-junction trap. (a) The X-junction trap can be used to transport ions to one of three possible regions from an X-shaped ensemble of electrodes. The electrode wafers are $125\mu m$ thick and spaced apart by $250\mu m$. The X-junction trap has a total of 18 trap zones that include two experiment regions E and H and a vertical region V. In the experiment and vertical regions, the laser-machined slot spacing is 200 μm. A loading region, L, is connected via a 45° arm far from the junction with a slot-width of 300 μm. The biasboard is 500 μm from the bottom of the trap electrode wafers and is used to produce a uniform bias field orthogonal to the trap axis. The biasboard is machined with a large slot to allow laser access to all trap zones. (b) Dimensions for the experiment region E. It has similar geometry to the experiment region in the quantum logic trap, except that the diagonal spacing of the DC electrodes is 320μm. The RF bridge across the junction can be seen on the right.

junction [67, 15]. An external signal generator applies $\sim$1.6 W of RF that is inductively coupled to the resonator. The RF electrode potential has $\sim$200 V peak amplitude. These RF parameters lead to a pseudopotential with a $\omega_r/2\pi \approx 12$ MHz radial frequency for a ^{9}Be$^+$ ion.

4.3 Containment System

4.3.1 Vacuum Components

Collisions between trapped ions and background gas lead to knocking ions out of the ion trap. Therefore, the ion traps are isolated from the environment by a vacuum system. Our wafer traps are enclosed in a quartz cell with fused-silica windows for laser access, which is kept at low pressure. The vacuum pressure is kept at $< 10^{-10}$ torr, which is typical in ion traps. The layout of our vacuum system is shown in Fig. 4.7. To maintain the low pressure, an ion pump continuously removes background gas. An ion gauge provides a measurement of the pressure in the system. A titanium-sublimation pump evaporates a titanium layer in the local vicinity to capture stray background gas (primarily H_2) in the system. This pump is run infrequently, only at times when we suspect that there is an excess of background gas about the ion trap.

There are electrical feedthroughs to bring various potentials from outside the vacuum into the system. There are 25-pin ribbon-cable connectors (one socket in the quantum logic trap, two in the X-junction trap) to carry potentials to the DC electrodes. Additional electrical feedthroughs supply currents to neutral-atom sources of ^{9}Be and ^{24}Mg (quantum logic trap) or ^{25}Mg (X-junction trap) for the first stage of loading ions. Currents, $\sim$1 A, heat metal structures holding bulk neutral-atom material inside the vacuum system, and the heat causes neutral atoms to evaporate into the chamber.

The ion trap and the RF resonator extend out from the side of the vacuum chamber. A quartz cell encloses the trap and resonator, keeping them under vacuum. In Fig. 4.7, the quartz cell surrounding the trap is shown as a nonuniform cylinder; the ion trap is surrounded by four windows that allow laser beams access to the trap from multiple directions. The windows are made from

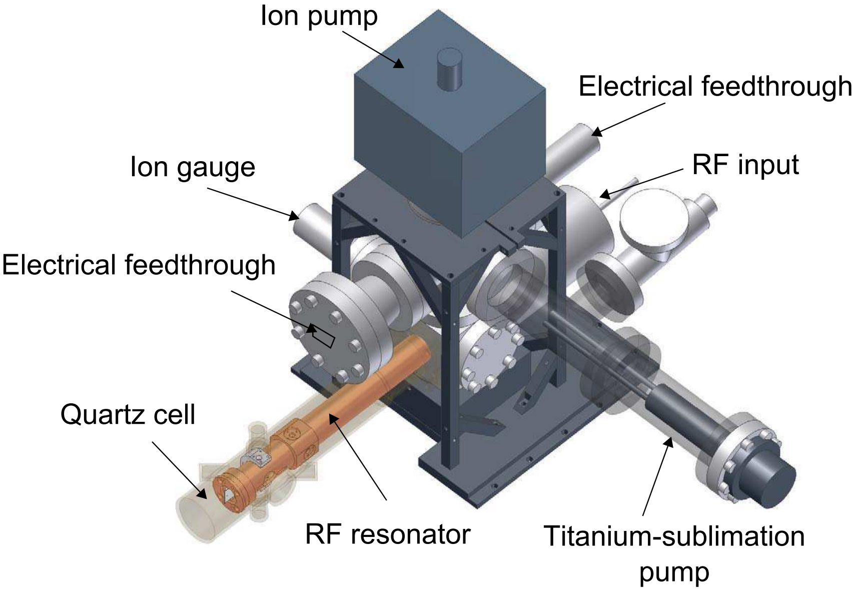
Ion pump
Electrical feedthrough
Ion gauge
RF input
Electrical feedthrough
Quartz cell
RF resonator
Titanium-sublimation pump

Figure 4.7: Diagram of the vacuum system used to maintain low pressure around the ion traps. The trap is enclosed in a quartz cell. The vacuum is kept at less than 10^{-10} torr. The DC and RF to the trap electrodes are introduced from outside of the vacuum system.

UV-grade fused silica. The slots in the trap wafers allow beams to pass from the windows, through the trap, and then exit out the other side. The beams which enter through various viewports are for Doppler cooling, ion-internal-state preparation, and Raman transitions, which are sometimes required in multiple zones in a single experiment.

4.3.2 Loading Ions

To load ions into the trap, a neutral atom source emits atoms towards the loading zone. There are two neutral atom sources: one is a ^{9}Be wire wrapped around a tungsten filament and the other is a stainless-steel tube loaded with isotope-enriched ^{24}Mg (in the quantum logic trap) or ^{25}Mg (in the X-junction trap). Atoms are emitted by heating their supporting metal structure; the heating evaporates atoms into the vacuum. As neutral atoms are emitted, they are ionized by either electron-bombardment from an in-vacuum electron gun or by photo-ionization (PI) light from laser sources. PI light is tuned to resonantly excited neutral ^{9}Be from $2s^2$ to $2s2p$, or ^{25}Mg from $3s^2$ to $3s3p$, after which a second photon excites the electron to continuum. We also shine Doppler-cooling light on the load region to cool ions once ionized in the trap zone beneath the trap depth. A typical loading rate in our experiment is one ion in every $\sim$10 s.

The ^{9}Be atoms are ionized through PI laser light with a 235 nm wavelength. To generate the PI light, first a laser-source at 532 nm with 5 W of power enters an optical cavity with a Titanium Sapphire (ti:sapph) crystal to generate a mode-locked pulsed laser at 705 nm with time-averaged power of $\sim$600 mW. This is then tripled through first a doubling stage with second harmonic generation (SHG) crystal and then a single-pass summing stage with a SHG crystal to a 235 nm source with time-averaged power of $\sim$10 mW, aligned to be incident on the vacuum chamber towards the load region. PI light with a 285 nm wavelength is used to ionize the neutral ^{25}Mg. This is generated starting with a near-infrared seed laser at 1140 nm which is amplified and sent through single-pass SHG crystal to achieve 570 nm light. This is followed by a doubling cavity using a BBO crystal for the final 285 nm UV light with 100 μW incident on the load region.

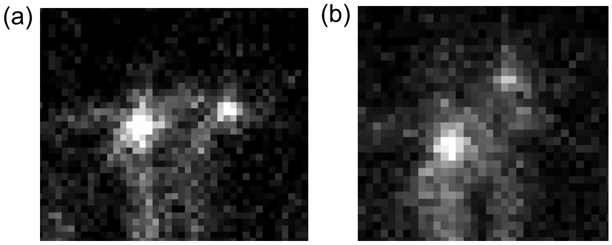

Figure 4.8: Images collected from a CCD camera simultaneously imaging fluorescence from ^{25}Mg^{+} on the left and ^{9}Be^{+} on the right. (a) Two ion species trapped in a shared trap zone with an approximate $\sim$4 μm spacing. (b) After applying a bias-field orthogonal to the trap access by a shim across diagonally-opposite DC electrodes, the ion crystal twists off of the trap axis due to the different pseudopotential confinement strength for the different-mass ions.

4.3.3 Imaging System

One of the windows in the quartz cell is used as a view port for the imaging system (shown in Fig. 4.9). A charge-coupled device (CCD) camera is typically used when loading ions so that we can see the ions as they are loaded into the trap, though during experiments we image the ion fluorescence on a photo-multiplier tube (PMT) for greater quantum efficiency. When our Doppler-cooling or resonant laser light scatters off of the ion, ion fluorescence is collected through several focusing optics. Our optics allow us to spatially resolve multiple ions in a single trap zone when imaging on the CCD camera.

The current imaging system as of this thesis has an initial stage for focusing the fluorescence from trapped ions, which is a 10x objective lens capable of imaging two different wavelengths (see Ref. [68] for details). Both ^{9}Be^{+} light at 313 nm and ^{25}Mg^{+} light at 280 nm can be imaged simultaneously. The next stage of focusing comes from a curved mirror which gives 5x magnification, for a final 50x magnification. See Fig. 4.8 for CCD image captures of two ion species simultaneously imaged in a single trap zone in the X-junction trap. The PMT is used to collect experimental data through detecting photons scattered from either ion species (see Chapter 2). For the experiments in this thesis, we only detect ^{9}Be^{+}, however, the ability to image detection light from both ion species opens up the possibility of performing QIP experiments on qubit states from both ion species simultaneously.

4.3.4 Magnetic Field Coils

We require a ~ 120 Gauss magnetic field to achieve the field-insensitive qubit splitting we use for QIP as discussed in Chapter 2. The field is generated by a pair of water-cooled coils of copper in a Helmholtz configuration, looped in a rectangular shape with dimensions 40 cm by 20 cm, separated from each other by 8 cm and centered on the ion position, as diagrammed in Fig. 4.9. The coil is made of twenty turns of hollow, square copper tubing, with 0.157” width and a 0.1” diameter round bore coated with kapton insulation. We apply 63 A of current to each coil to produce the desired field strengths at the position of the ion confinement. This current can generate $\sim$300 W of heat, necessitating water cooling. An additional pair of coils with 40 turns of 20 AWG copper wire are also used for adjustments to the field. We periodically intersperse experiments with a measurement of the resonant transition frequency for a ^{9}Be$^+$ hyperfine transition, and based on the result alter the current through the smaller coils until the correct magnetic field is applied to achieve our field-insensitive qubit transition.

4.4 Lasers

Incident laser light interacts with ions by entering through fused silica windows in the quartz cell and passing through the slots etched into the trap wafers. The magnetic field defines the quantization axis for the ions’ atomic states. Thus, the incident direction of light relative to the magnetic field $\hat{B}$ affects the allowed selection rules for internal-state transitions. Since the laser beam electric fields must be orthogonal to the beam direction, any beams traveling along the quantization axis do not have π-polarized light with respect to the ion, as discussed in Chapter 2. We need beams for carrier Raman transitions (those which directly drive transitions between hyperfine states) along with a configuration with a difference k-vector δk along the trap axis to interact with axial motion. Therefore, we need multiple laser-beam directions incident on our ions to perform all of the transitions that we need for our experiments. As shown in the diagram in Fig. 4.9, there are four windows that provide different beam directions. The diagram’s caption describes the various laser beams’

Beam	Visible Wavelength (nm)	Visible Power (mW)	UV Wavelength (nm)
BD	626.266	330	313.13
RD	626.395	230	313.2
Raman	626.610	2050	313.31

Table 4.1: Visible and corresponding UV wavelengths and visible powers for the ^{9}Be$^+$ lasers.

alignments with respect to the trap axis and magnetic field.

To-date, there are no commercially available UV sources with the powers necessary for our experiments, so our UV laser beams are derived from longer-wavelength sources. The light necessary for ion-laser interactions with ^{9}Be$^+$ is at 313 nm for both Raman transitions and those used for Doppler cooling beams (the Blue Doppler beamline) and repumping beams (the Red Doppler beamline). These are generated from laser sources that begin with seed lasers in the IR and then sent through amplifiers. The lasers are then single-pass summed through a temperature-controlled MgO:PPLN crystal held at $\sim$190 K temperature to produce visible wavelengths in the red at $\sim$626 nm [69]. The wavelengths needed after the frequency-summing is similar enough for all the beams such that power from the seed lasers at 1050 nm and 1550 nm can be re-used for different beams.

After the visible light is generated, the frequencies for Blue Doppler and Red Doppler are stabilized to an I_2 Doppler-free saturated absorption spectroscopy signal. The Raman beams, used for the Raman transitions between hyperfine states in ^{9}Be$^+$, are detuned by -250 GHz from the $S_{1/2}$ to $P_{1/2}$ transition (see Chapter 2), though the absolute frequency is not critical. Rather, the difference-frequency between two Raman beams is more critical, and therefore the beams are not stabilized to any frequency reference. Then, the visible light is sent into a bow-tie, or 4-mirror ring, cavity with a frequency-doubling BBO crystal at one of the foci [70, 71, 69]. The cavities consist of four mirrors, one of which is mounted on a PZT. The cavity length is stabilized to stay on-resonance through feedback on the PZT using a Hansch-Couillaud lock system [72]. The wavelengths and powers for the visible for ^{9}Be$^+$ beams are listed in Table 4.1 along with the corresponding UV wavelengths.

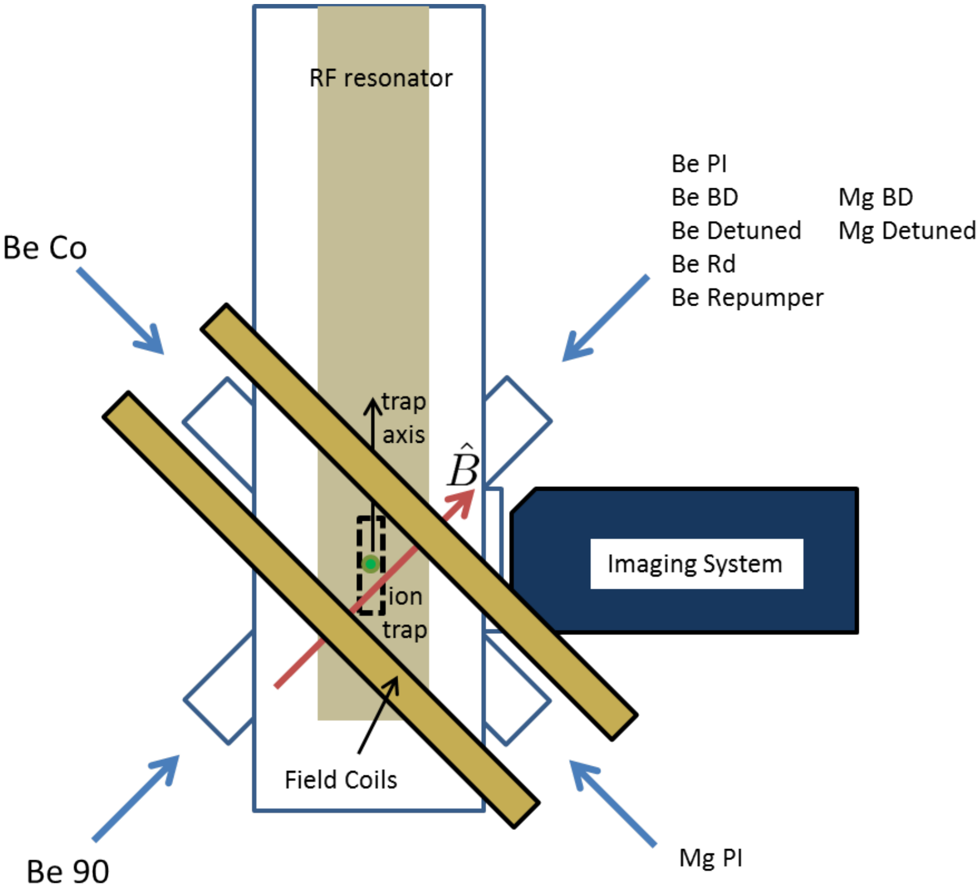

Figure 4.9: The relative alignment of the ion imaging system, magnetic field coils, incident laser light, and the ion trap. The ^{9}Be$^+$ Raman beams, aligned 90° to each other labelled Be Co (so-called for sometimes having co-propagating beams with a relative detuning for carrier Raman transitions that are motion-insensitive) and Be 90 (so-called for the relative allignment to Be Co for motion-sensitive Raman transitions), are depicted entering upper and lower ports of the left side of the diagram. ^{9}Be$^+$ blue Doppler and detection beams labelled Be BD, far-detuned Doppler cooling beam labelled Be Detuned, and repumping beams labelled Be Rd and Be Repumper (names respective to the transitions discussed in Chapter 2), enter on the upper right window and pass through the experiment region E of the X-junction trap. The ^{25}Mg$^+$ Doppler cooling beam labelled Mg BD and the far-detuned Doppler cooling beam labelled Mg Detuned co-propagate with the ^{9}Be$^+$ Doppler beams. Some of the Doppler cooling light is redirected towards the loading region L when loading ions into the trap. The coils generate a $\sim$120 Gauss magnetic field at the position of the trapped ions. The imaging system is meant to focus light scattered off of the ions onto a CCD camera or a PMT to observe fluorescence from the trapped ions under incident detection light.

The ^{25}Mg^{+} Doppler-cooling light is derived from a 560 nm dye laser with a bow-tie cavity.. The same dye laser setup was used for ^{24}Mg^{+} for the quantum logic trap, with details described in Ref. [14]. The dye laser cavity is stabilized in long-term to a I$_2$ Doppler-free saturated absorption spectroscopy signal. In short-term the laser is stabilized to an external reference Fabry-Pérot cavity with feedback on a PZT-mounted mirror and a PZT-adjustable etalon within the dye laser cavity. The visible light has a wavelength of 559.269 nm with ∼300 mW of power. This is sent through a frequency-doubling cavity similar to those used for ^{9}Be^{+} light for a UV wavelength of 279.63 nm.

All of the beams are position-stabilized before entering the trap apparatus. After the UV beam exits the doubling cavity, the position stabilization is achieved by first placing two mirrors mounted on PZTs as part of the beam path, and then picking off a small amount of laser light from the UV beam in two places farther down-stream, closer to the trap apparatus. The picked-off light is incident on a position-sensing quadrant detector, and as the beam deviates from a desired position, feedback on the PZT-mounted mirrors realigns the beam position. All of these beams pass through double-pass acousto-optic modulators (AOMs) to shift their frequencies. To switch certain laser beams on or off during an experiment, a TTL signal from our experiment-control FPGA switches the RF fed to the AOMs on or off to turn on or extinguish the diffracted beam. Following the UV beamlines, the beams then are passed through UV-compatible fibers to deliver the beams to the fused-silica windows to then pass through the ion trap [73]. Then, before entering the trap, the beams pass through $\lambda/4$ and $\lambda/2$ waveplates to select the necessary polarizations followed by a lens to focus the beams to $\sim 30\mu m$ waists at the position of the ions. This beam waist is sufficiently large to illuminate our typical trapped ion chains, but is much smaller than the distance between trap zones.

4.4.1 ^{9}Be^{+} Blue Doppler Beam Line

The Blue Doppler UV beam line for Doppler cooling (discussed in Chapter 2) is diagrammed in Fig. 4.10. This beam line synthesizes three beams for the $|S_{1/2}, F=2, m_F=2\rangle \longleftrightarrow |P_{3/2}, F=3, m_F=3\rangle$, denoted simply $S_{1/2}$ to $P_{3/2}$, transitions. AOMs are used to shift the input beam frequency to the desired values. The UV laser beam's frequency is initially tuned so that shifting the input beam by $\sim$ +600 MHz shifts the beam to near-resonance. This beam, which we call BD, is then tunable between optimal Doppler cooling with a red-detuning of $-\Gamma/2 \simeq 2\pi\times$9.7 MHz from the $S_{1/2}$ to $P_{3/2}$ transition and on-resonance with $S_{1/2}$ to $P_{3/2}$ for detection. The beam for far-detuned Doppler cooling, or BD detuned, comes from shifting the input frequency by $\sim$ +200 MHz, which is $\sim$ -400 MHz red-detuned from the $S_{1/2}$ to $P_{3/2}$ transition. The BD beam enters the trap with $\sim 5\,\mu$W of power, and the BD detuned beam with $\sim 500\,\mu$W of power.

4.4.2 ^{9}Be$^+$ Red Doppler Beam Line

The Red Doppler UV beam line for repumping into the initial state for ^{9}Be$^+$ (discussed in Chapter 2) is diagrammed in Fig. 4.11. This beam line synthesizes two beams for the $|S_{1/2}, F = 2, m_F = 1\rangle \longleftrightarrow |P_{1/2}, F = 2, m_F = 2\rangle$ repumper and $|S_{1/2}, F = 1, m_F = 1\rangle \longleftrightarrow |P_{1/2}, F = 2, m_F = 2\rangle$ RD transitions used for optically pumping for state initialization. AOMs are used to shift the beam frequency to the desired values. The UV laser beam's frequency is initially tuned so that it is in-between the resonances for the $|S_{1/2}, F = 2, m_F = 1\rangle \longleftrightarrow |P_{1/2}, F = 2, m_F = 2\rangle$ and $|S_{1/2}, F = 1, m_F = 1\rangle \longleftrightarrow |P_{1/2}, F = 2, m_F = 2\rangle$ transitions, and this beam is then split into two beams to be tuned to resonance for the repumper beam by +800 MHz and RD beam by -310 MHz. This difference in frequency then spans the hyperfine splitting for the $S_{1/2}$ states. The RD beam enters the trap with $\sim 10\,\mu$W of power and the repumper beam with $\sim 5\,\mu$W of power.

The Blue Doppler beams are combined with the Red Doppler beams through a 50/50 beam splitter. When we desire to have these beams in an "off" state, to avoid leaked light incident on the ions due to imperfect extinguishing of the RF to the AOMs or pick-up in the AOM transducers, we use a "switch AOM" configuration. This comprises two additional 200 MHz AOMs (not diagrammed), through which the beams are aligned for the +1 order and then the -1 order through the pair of AOMs. This results in no net shift in the beam frequencies, but allows a strong extinguishing of the beam when an off state is desired. After the Blue Doppler and Red Doppler beams pass through the switch AOM configuration, they are coupled into a UV-compatible fiber and delivered to the fused-silica input windows to the ion trap.

4.4.3 ^{9}Be$^+$ Raman Beam Line

The Raman beam lines for driving Raman transitions between hyperfine states of the $S_{1/2}$ hyperfine manifold in ^{9}Be$^+$ are diagrammed in Fig. 4.12. The beamline synthesizes two beams from the input UV beam. The Co beamline is so-named for being capable of having co-propagating Raman transition beams for carrier-transitions on the hyperfine states. There is a 600 MHz AOM which is in a double-pass configuration carefully aligned such that both the 0^{th} order and +1 order beams leave the AOM overlapped with each other, and are co-propagating for the rest of the beamline. This enables carrier Raman transitions with a single beamline. The Co beamline then passes through a double-pass Co AOM to allow shifts in the beam such that the Co coupled with another Raman beam span the $S_{1/2}$ hyperfine splittings. For motion-sensitive Raman transitions, there is also a 90 beamline so-called for being 90° to the Co beam when entering the ion trap. This beam passes through a double pass AOM, so that the Co is shifted by +620 MHz in the double-pass Co AOM and the 90 beam shifted by -420 MHz in the double-pass 90 AOM to span the $S_{1/2}$ hyperfine splittings. The beams then pass through UV fibers which delivers the beams to the trap, and the Co and 90 beams each enter the ion trap with $\sim$40 mW of power.

4.4.4 ^{25}Mg$^+$ Doppler Beam Line

The ^{25}Mg$^+$ UV beam line for Doppler cooling (discussed in Chapter 3) is diagrammed in Fig. 4.13.. This beam line synthesizes two beams for the $|S_{1/2}, F = 3, m_F = 3\rangle \longleftrightarrow |P_{3/2}, F = 4, m_F = 4\rangle$ transition, denoted as $S_{1/2}$ to $P_{3/2}$ transition. The UV laser beam's frequency is initially tuned so that shifting the input beam by $\sim$ +710 MHz with AOMs shifts the beam to near-resonance. This beam, which we call MG BD, is used for near-detuned cooling light with a detuning of $-\Gamma/2 \simeq -2\pi \times 21$ MHz from the $S_{1/2}$ to $P_{3/2}$ transition. The beam for far-detuned Doppler cooling, or MG detuned, is $\sim$ -500 MHz red-detuned from the $S_{1/2}$ to $P_{3/2}$ transition. The MG BD beam enters the trap with $\sim 30\mu$W of power, and the MG detuned beam with ~ 1 mW of power.

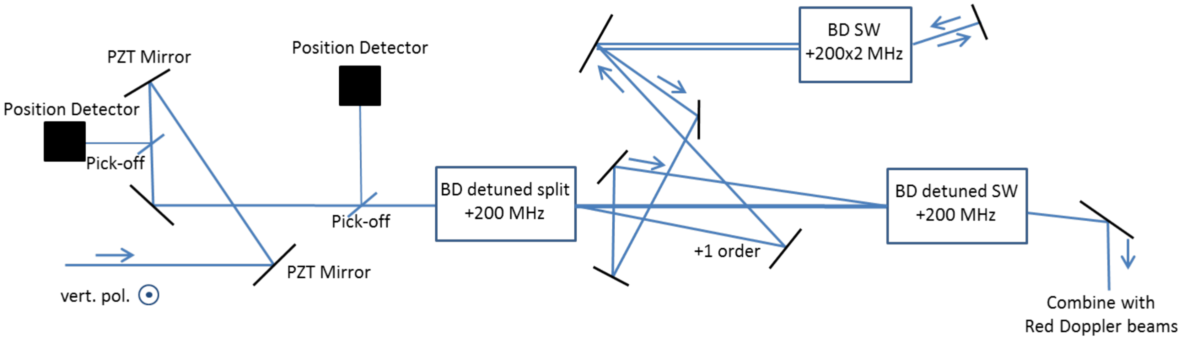
PZT Mirror
Position Detector
Position Detector
Pick-off
Pick-off
PZT Mirror
vert. pol.
BD detuned split
+200 MHz
BD SW
+200x2 MHz
BD detuned SW
+200 MHz
+1 order
Combine with
Red Doppler beams

Figure 4.10: $^{9}\mathrm{Be}^{+}$ Blue Doppler beam line beginning with UV from the doubling cavity on the left. The boxes with frequency shifts denote AOMs in the beam path. The output path of the double-pass AOM configuration has a small vertical offset, which is then reflected off of a mirror in a different direction from the input path. After the doubling cavity, the beam has a small amount of power diverted to quadrant position detectors to stabilize the beam position. The beam enters the BD detuned split AOM, so-called for splitting the Blue Doppler BD beam from the far-detuned cooling beam BD detuned, and when this AOM is switched on, the +1 diffracted order is sent to a +200 MHz double-pass AOM labeled BD SW (so-named as it is used as the switch for BD) to generate the near-detuned cooling light or resonant light. The BD detuned SW AOM is used to put +200 MHz on the far-detuned beam through the +1 diffracted order, and the BD beam is recombined with BD detuned by being alligned co-propagating with the +1 order BD detuned SW path.

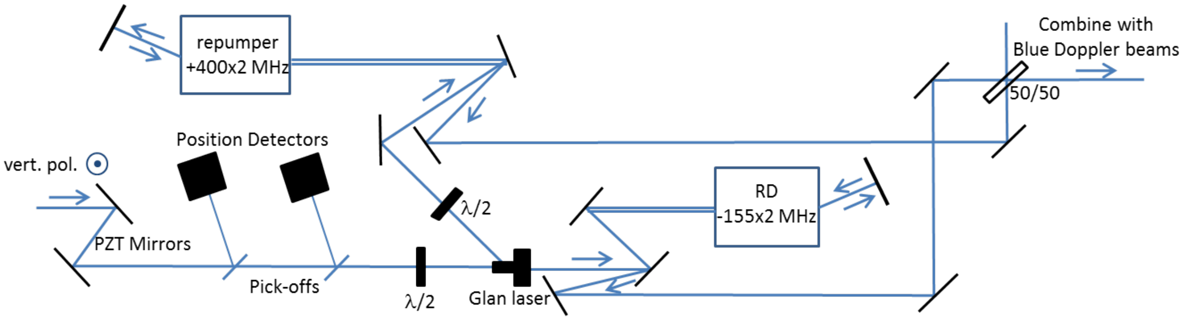
repumper
+400x2 MHz
vert. pol.
Position Detectors
PZT Mirrors
Pick-offs
λ/2
λ/2
Glan laser
RD
-155x2 MHz
50/50
Combine with
Blue Doppler beams

Figure 4.11: $^{9}\mathrm{Be}^{+}$ Red Doppler beam line beginning with UV from the doubling cavity on the left. The boxes with frequency shifts denote AOMs in the beam path. The output path of the double-pass AOM configurations has a small vertical offset, which is then reflected off of a mirror in a different direction from the input path. After the doubling cavity, the beam has a small amount of power diverted to quadrant position detectors to stabilize the beam position. The beam passes a $\lambda/2$ waveplate followed by a Glan-laser designed to split the beam into two distinct beams with orthogonal polarizations for the repumper and RD beams (same-polarization achieved again with a $\lambda/2$ waveplate in the repumper path). The repumper is double-passed through an AOM for a +800 MHz shift and the RD is double-passed for a -310 MHz shift. The Red Doppler beams are then recombined on a 50/50 beam splitter before then combining with the Blue Doppler beams on another 50/50 beam splitter.

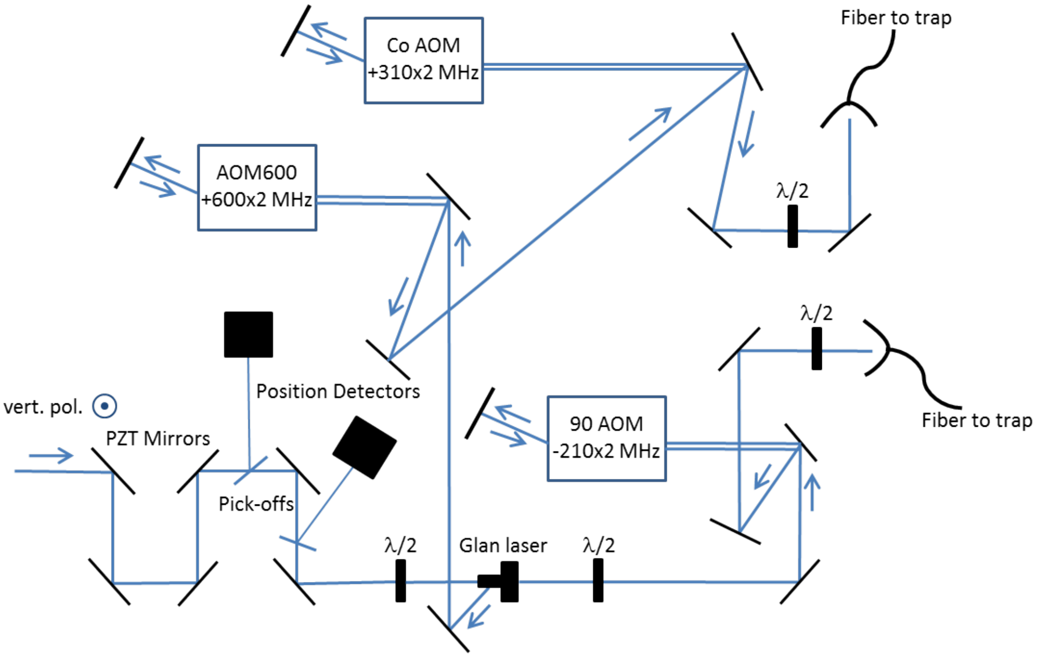

Figure 4.12: ^{9}Be$^+$ Raman beam lines beginning with UV from the doubling cavity on the left. The boxes with frequency shifts denote AOMs in the beam path. The output path of the double-pass AOM configurations has a small vertical offset, which is then reflected off of a mirror in a different direction from the input path. After the doubling cavity, the beam has a small amount of power diverted to quadrant position detectors to stabilize the beam position. The beam passes a $\lambda/2$ waveplate followed by a Glan-laser designed to split the beam into two distinct beams with orthogonal polarizations for the Co and 90 Raman beams (same-polarization achieved again with a $\lambda/2$ waveplate in the 90 path). The Co beam passes through the AOM600 which is in a double-pass configuration carefully alligned such that both the 0^{th} order and +1 order leave the AOM co-propagating to drive carrier Raman transitions. For motion-sensitive Raman transitions, we use the 90 beamline, so-called for being 90° to the Co beam when entering the ion trap. During Co-90 motion-sensitive transitions, the AOM600 is switched off and the Co is shifted by +620 MHz in the double-pass Co AOM and the 90 beam shifted by -420 MHz in the double-pass 90 AOM to span the $S_{1/2}$ hyperfine splittings. The AOMs have bandwidths that allow scanning ranges of $\sim \pm$50 MHz, allowing us to achieve our desired hyperfine transitions. The beams then pass through UV fibers which delivers the beams to the trap.

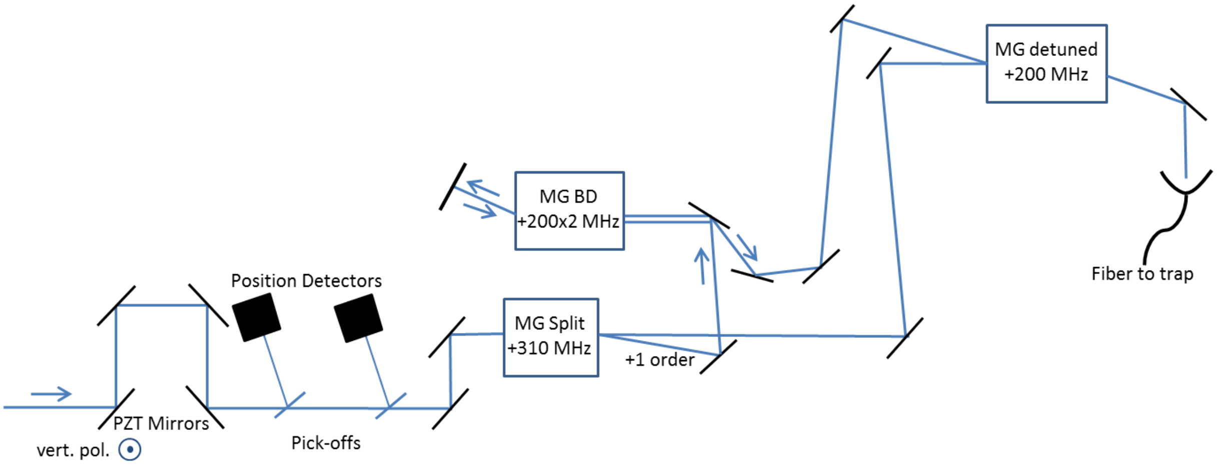
MG detuned
+200 MHz
MG BD
+200x2 MHz
Fiber to trap
Position Detectors
MG Split
+310 MHz
+1 order
PZT Mirrors
vert. pol.
Pick-offs

Figure 4.13: $^{25}\mathrm{Mg}^{+}$ Doppler beam line beginning with UV from the doubling cavity on the left. The boxes with frequency shifts denote AOMs in the beam path. The output path of the double-pass AOM configuration has a small vertical offset, which is then reflected off of a mirror in a different direction from the input path. After the doubling cavity, the beam has a small amount of power diverted to quadrant position detectors to stabilize the beam position. The beam enters the MG Split AOM, so-called for splitting the Blue Doppler MG BD beam from the far-detuned cooling beam MG detuned, and when this AOM is switched on, the +1 diffracted order is sent to a +200 MHz double-pass AOM labeled MG BD to generate the near-detuned cooling light. The MG detuned AOM is used to put +200 MHz on the far-detuned beam through the +1 diffracted order, and the MG BD beam is recombined with MG detuned by being alligned co-propagating with the +1 order. The beams then pass through UV fibers which delivers the beams to the trap.

Chapter 5

Experiment Control

As the complexity grows in our experiments, so too does the need for adaptable and scalable experimental control. Our experimental needs include precise control over the timing, frequencies, and phases of laser or microwave pulses, controlling the timing for ion transport through time-varying trap potentials, and PMT count collection for state detection. Additionally, an experimental sequence may requiring branching (a change in the experimental sequence based on the result of state detection) which is useful for things such as for error correction during quantum information processing. We also need rapid adaptability from day to day and experiment to experiment, such as being able to rapidly measure and calibrate motional sideband frequencies, calibrate the external magnetic field, and other regular calibrations interspersed with the main experimental work. Our experimental control comes in large part from a home-built system which comprises a graphical user interface (GUI) on a host computer, TTL and direct digital synthesis (DDS) interface sequenced by a field-programmable gate array (FPGA), and peripheral software and hardware control. This experiment FPGA system forms the core of the interface between us and the quantum information processor.

A key component to our approach to scalable QIP is to achieve information transport through the physical transport of ions between spatially-distinct trap regions. This transport requires fast and precise electronics to control the trap potentials if transport is to be performed in a way such that motional states of ions are preserved. To address this need, I developed a novel device dedicated to efficient and fast arbitrary voltage outputs in a ±10 V range for our experiments, which can be used for trap confinement, ion transport, and for quantum logic pulse shaping. It is designed with a 50 MHz update rate, which is much faster than both the ion trap oscillation frequency and our Raman transition Rabi rates. The device is based around an FPGA as a controller that updates the inputs to digital-to-analog converters (DACs) that in turn output the voltages to a fast amplifier. It has the capability to functionalize multiple waveforms and switch between them based on TTL inputs during experiments.

In this chapter, I first give a brief introduction to FPGA technology. I then describe how it is used for both timing and frequency control of the atom-laser interactions as well as measurement of the ion states. For the bulk of the chapter, I describe the FPGA-based electronics that I developed for an arbitrary waveform generator; a summary of the hardware and applications is detailed in Ref. [74], with expanded information provided in this chapter and full schematics in Appendix B. Its primary use is for precision control of the trap potentials, described here with specific attention to its features for scalable methods for ion transport. It is also used for laser- and microwave-pulse shaping, and I briefly describe this application.

5.1 Introduction to FPGAs

FPGAs are logic ICs (integrated circuits) that are reconfigurable for user-specified logic operations. They were first commercially available from Xilinx, though there are now a number of manufacturers. An FPGA chip largely comprises internal, on-chip arrays of logic gates, which are configured to perform whatever logic sequences the user demands. There are input and output logic signals to the FPGA, which the FPGA interprets through its configured internal logic gates. The FPGA thus is configurable to functionalize its outputs based on its inputs. The FPGA also comprises logic blocks that may include registers, memory, buffer drivers, multiplexers, and mathematical operations. This is a technology that allows enormous amounts of digital adaptability.

The FPGA logic-gate configuration, or gateware, is user-defined through computer communication. A common communication method is through a joint test action group (JTAG) programmer.

Specific data that contains the configuration information for the on-chip logic is often derived from a hardware description language, typically VHDL or Verilog; the FPGAs in our lab are typically designed with VHDL. FPGA manufacturers often provide software tools to assist in synthesizing code into an FPGA configuration. The language is designed to be convenient for specifying logic sequences. The logic on the FPGA updates each clock cycle from an externally-supplied clock signal. This makes the logic timing of the FPGA deterministically known to the user. The language syntax defines processes in parallel operations, thereby specifying simultaneous operations at each clock cycle in a deterministic way.

Each physical input or output line to and from the FPGA chip can be described in VHDL; in code, it is treated as a signal, which is an object operated upon in a way similar to a variable. Signals are used either for logic gates (such as if statements) or to produce a derived logic output. An FPGA configuration, then, can be used as a sequencer of logic operations, potentially conditioned on external signals. This is used for controlling logic pulse sequencing by having logic output signals from the FPGA directly control switching between on and off states in devices such as RF switches, or more generally having inputs and outputs communicate with a variety of ICs. In addition to being an array of logic gates, FPGAs have on-chip blocks of static RAM. The RAM can hold data to be stored and dynamically accessed during FPGA operations. In this way, a host computer could send data that signals the FPGA to store information in block RAM, such that the FPGA later has access to data in real-time. Uploading information to RAM provides a way to load data before an experiment begins so that the FPGA can run an experimental procedure purely from within its own memory with no loss in run time due to computer interface.

5.2 Experiment-Control FPGA

In our typical experiments, such as in Refs. [27, 28, 66], we need many laser pulses with varying frequencies, durations, and phases, which are possibly interspersed with transport waveforms, and followed by detection of ion states through collection of photon counts from a photo-multiplier tube (PMT). The experiments are controlled by a single “experiment” FPGA that is used to control and sequence all of these necessary operations. This experiment FPGA uses the Virtex-IV FPGA from Xilinx, interfaced through a commercial evaluation board, which is configured to receive data from a host experiment-control computer (connected through a PCI slot) to specify the timing and sequencing of the experiment.

The in-depth details for this pulse sequencer are in Ref. [34], so I will restrict the discussion to the key features when running experiments. The experiment FPGA is clocked by an external synthesizer at 62.5 MHz. The FPGA provides our experiments with 16 independent TTLs. It can control of up to 32 independent direct digital synthesizers (DDSs), which are principally used to set frequencies and phases of laser pulses by feeding the digitally synthesized RF signals from the DDSs into acousto-optic modulators (AOMs) and deflectors (AODs). Most TTL channels control the on/off states of RF switches for DDS signals fed to the AOMs and AODs, thus controlling the timing of the laser pulses. One TTL is dedicated to triggering ion transport waveforms. Before an experimental sequence begins, the host computer downloads a specific sequence of TTL and DDS settings to the experiment FPGA into its block RAM. The FPGA reads RAM in real time, controlling the experiment as the user had defined.

A DDS produces an RF source from a digital phase accumulator and a sine-wave look-up table along with an input reference clock, with final analog output from a DAC. The phase accumulator divides the desired output frequency by the reference clock and uses this to calculate the step-size at which an address register steps through the sine-wave lookup table, where the register points to locations in the sine-wave look-up table. The phase accumulator typically has far more digital precision than typically available in the look-up table or the DAC output such that it maintains a much higher-precision calculation of the phase than available in the final output of the DAC. The DDSs in the experiment, the AD9858, have a 32-bit phase accumulator, 14-bit phase-offset adjustment, and an output voltage from 10-bit digital-to-analog conversion. To ensure accuracy and stability, the DDSs are synchronized to a 1 GHz signal derived from the 10 MHz Hydrogen maser source at NIST.

An experimental sequence ends with collecting PMT counts from ion state detection. The FPGA has a dedicated TTL input channel which reads photon counts from a PMT for the detection duration, typically $\sim 200\mu$s. The count data is then received by the host computer over many repeats of an experiment to build up suitable statistics at the end of many rounds of experimental sequences. The FPGA is designed to allow the conditional branching off of the detection results if necessary, which has applications in error correction or in functionalizing certain experiments.

We have a graphical user interface (GUI) to an experiment-control program that allows us to conveniently intersperse many user-defined experiments. Our own parser language, which serves as a high-level language for our digital control, had been designed for defining experiments through our FPGA system. This allows us to use a very simple language to specify relatively complex sequences and careful timing for our lasers, waveforms, and other experimental parameters. The experiment-control program translates the results of parsing our digital control language into a stream of data that the FPGA interprets, stores into RAM, and then runs to produce the physical realization of our experiment.

5.3 Arbitrary Waveform Generator

In demonstrations of our multi-electrode trap array scheme for QIP, ion transport required hundreds of microseconds to remain in the adiabatic regime, where the forces applied to the ion cause only small displacements from the center of the confining potential, while each quantum logic operation typically took $\sim 10\mu$s [29, 55, 27, 28]. For larger scale quantum information processing, development of larger trap architectures is necessary; some examples of the work towards larger multi-electrode trap designs can be seen in Refs. [13, 18, 19, 15, 20, 21]. However, the time scale discrepancy between quantum logic and ion transport poses a bottleneck for rapid quantum information processing. In addition, slow transport leads to an increased motional excitation due to heating from electric field noise originating from electrode surfaces [24], and therefore increases the laser cooling needed to initialize motion close to the quantum ground state via Doppler and Raman sideband cooling, which in turn further increases the incurred time penalty for ion transport. To overcome these challenges, it is necessary to make ion transport times comparable to gate speeds which will necessarily require leaving the adiabatic limit where transport can not be considered slow compared the ion motional trap period.

The ambient heating in ion traps is the dominant source of motional excitation when performing adiabatic ion transport. Work in Ref. [25] reported a 100-fold improvement in heating rates from electrode surface cleaning, but this method cannot easily be applied to our multiple-wafer traps and transport durations still need to be reduced. Experiments in Refs. [55, 67] used commercially available digital-to-analog converters (DACs) with update rates of 500 kHz for ion transport. However, update rates lower than the frequencies of ion motion in the confining potential well are unsuitable for precise control of the potential on time scales similar to or faster than the trapped ions' motional period. In addition, harmonics of the 500 kHz update rate could cause significant heating of the ions' motion if not heavily filtered [15]. A further requirement comes from large-scale error correction algorithms that may require the ability to quickly alter ion transport conditioned on the detection of errors. For example, a demonstration of an error correction algorithm, which is conditioned on the detection of errors, has been carried out in this multi-electrode scheme [30] had a similar slow transport. Hence, our electronic needs for this quantum information processor scheme include fast DAC update rates compared to confinement frequencies, which can be used to reduce the duration of ion transport with low motional excitations on a quantum logic time scales. We also require the ability to control many electrodes at once with low latency in accessing DAC output patterns (waveforms) that can be conditionally selected.

To this end, I addressed our technical needs by creating a fast multi-channel arbitrary waveform generator (AWG) with an update rate of 50 MHz, well beyond currently relevant trapping frequencies (typically $\sim$1 MHz). The design is easily scalable to control a large number of electrodes. The AWG is based on an FPGA, which controls an ensemble of DACs that provide arbitrary analog outputs in a $\pm$10 V range. The device is capable of simultaneously storing multiple "branches," different sets of waveforms that can be selected by use of digital logic inputs on the device with a

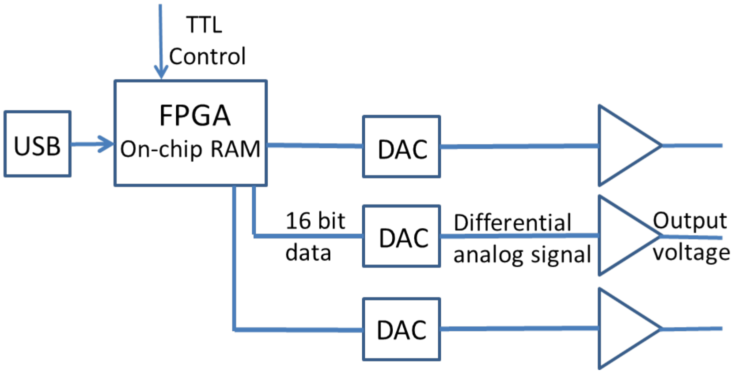

Figure 5.1: A flow diagram overview of the AWG. The host computer transmits waveform data via USB to the FPGA which is stored in on-chip RAM. The FPGA transmits a 16-bit digital signal derived from its RAM to each DAC, whose output is then amplified.

40 ns latency. This section covers the hardware which comprises the AWG and the software control, followed by the underlying operation of the FPGA, and then gives examples of experimental uses.

5.3.1 Hardware

The core of the AWG is the Xilinx Spartan-3E XC3S500E PQ208 model FPGA, coded in VHDL using the Xilinx ISE Design Suite. The FPGA is directly connected to three 16-bit Analog Devices AD9726 DACs. The AD9726 DAC was chosen because of its high speed, its linearity, and its use of low voltage differential signal (LVDS), which is resistant to pick-up noise. The FPGA is clocked by a 50 MHz crystal oscillator. Each FPGA has 32 output signals (16-bit LVDS) and two derived 50 MHz clock-sources connected on-board to each DAC (three DAC channels per FPGA). Our experiment-control computer transmits waveform data via USB to the on-board FTDI FT245RL USB-to-parallel-FIFO (first-in-first-out), which provides an interface to upload waveform data a byte at a time (8 bits) from a host computer to the FPGA. When data is transmitted, the FPGA interprets the data stream and stores information for each DAC channel in three segments of on-chip, independent static random access memory (RAM) in the FPGA. An overview for the operation of the AWG is shown in Fig. 5.3.1.

There are two types of AWGs, a “master” and a “slave”, with a small number of hardware differences. The VHDL code used is the same for both masters and slaves, however the FT245RL and a 50 MHz crystal oscillator are only present on a master. Slaves are connected to the master through board-to-board interconnects, through which the waveform data and the clock signal are routed to be processed by their respective FPGAs, each identified by an on-board hex switch. One master and one to five slaves can be connected together to provide up to 54 synchronous channels on a single USB connection (limited by clock signal integrity). Separate masters are referenced to their own oscillators and hence have timing offsets of at most 20 ns. This caused negligible errors in ion experiments at NIST (though it is possible to bypass the on-board crystal oscillator to use a single external clock signal for all masters used in experiments to clock the AWG at different speeds or to achieve better synchronous operation). Each AWG master is identified over the USB connection by a unique serial number programmed into the FT245RL, so in principle any number of channels can be controlled from a single computer (limited by the computer's USB architecture).

The DACs are clocked with 50 MHz signals derived by the FPGA from the crystal oscillator. Each DAC's output is referenced to a precision 1.25 V source (Linear Technology LTC6652), specified to have 10 ppm/$^\circ$C and 2.1 ppm noise, for stable and consistent potentials out of every channel. The differential signal outputs of each DAC are sent to the Analog Devices AD8250 high-speed amplifier with a gain of 10 to provide the final output potentials; the DAC and amplifier system is configured for a $\pm$10 V output with 16-bit linear resolution, stable down to roughly 30 μV and with $\sim 1\,\Omega$ output impedance. A 50 Ω resistor can be added in series with the output to prevent ringing in long cables. From observing after the resistor, we measure a white noise power spectral density of $\simeq$120 nV/$\sqrt{\mathrm{Hz}}$ with an external 50 Ω load. The amplifier's output has a measured slew rate of 40 V/μs; although this limits the voltage swing at each clock update, it is sufficient for our experimental implementations. A photograph of a master board is shown in Fig. 5.2 with the discussed components highlighted.

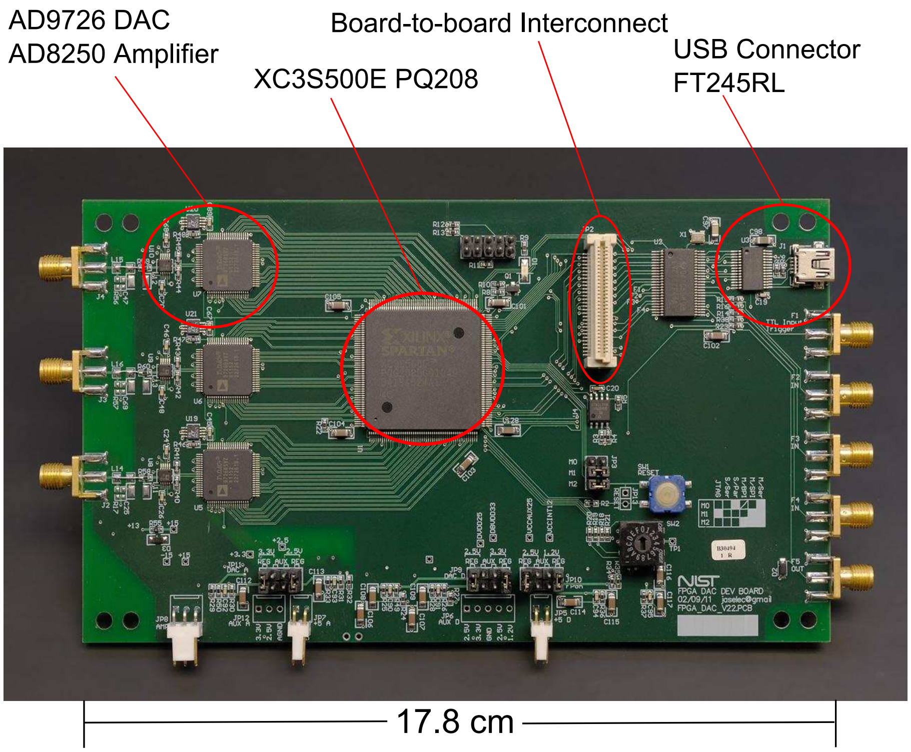
AD9726 DAC
AD8250 Amplifier
Board-to-board Interconnect
XC3S500E PQ208
USB Connector
FT245RL
17.8 cm

Figure 5.2: A master board. The key components described in the text are highlighted. The host computer communicates with the master board via USB. The FT245RL handles the interface with the XC3S500E PQ208 FPGA on up to three boards (a master and two slaves) on a shared communication channel through a board-to-board interconnect. The FPGA drives three AD9726 DACs whose output is fed to AD8250 amplifiers, which creates the final three output potentials. Reproduced from Ref. [74].

5.3.2 User Control

Before an experiment begins, a computer transmits waveform data via USB to be uploaded to the AWG's RAM for each channel. The FT245RL manufacturer provides a support library of C++ commands provided by the manufacturer. The support library includes commands to open communication with the FT245RL, to send bytes of data to the FT245RL (which in turns fills a data buffer which is read by FPGA), and to read data such as each FT245RL's serial number, which is used for identifying each master, or to possibly read bytes sent by the FPGA. This has been integrated into our experiment-control program, but computer control also exists as stand-alone control programs in C++ and Python. Before running an experiment, the experiment-control FPGA system is preconfigured to intersperse laser pulses and waveform triggers and the AWG is preconfigured with waveform data, so that an experiment runs without delays due to RAM upload times. When scanning an experimental variable involving waveforms, such as the waveform duration or a voltage offset, only the affected channels are redownload to minimize download times before running experiments.

Using the gateware at the time of this thesis, the AWG is able to operate in one of four modes: (1) Output specified by a single value for the output potential at each 20 ns clock cycle update, (2) Output given by values separated in time for specified durations, (3) Output given in terms of quadratic polynomials specified by a duration and coefficients, and (4) Output specified in terms of cubic polynomials. Options 2, 3, and 4 can provide increasing levels of data compression to overcome limited amounts of RAM and reduce waveform upload durations from the host computer. We generally use cubic spline interpolation of the desired waveform, which enforces 1^{st} and 2^{nd} derivative continuity in the final waveform and each cubic polynomial can have a duration of anywhere from 240 ns to $\sim$655 μs. When running experiments, we typically constraint the initial and final derivatives to be zero, thereby smoothing end points of potentials. The interval between a TTL trigger and when a waveform begins to run depends on the time required to read the initial data from memory (longest is the 4^{th} mode where 240 ns, or twelve clock cycles, are required before the waveform begins), but after this initial delay the memory is read continuously so that voltage updates are continuous with no loss due to read-time on each clock cycle.

Masters have input TTL ports routed to all connected slaves, and the port to signal that a waveform should begin running is labeled as F1. The rising edge of the TTL trigger signals the start of a waveform on all connected channels (a “run trigger”). Each waveform is assigned a branch number by the user and put into a corresponding segment of RAM in the FPGA. A branch is selected through three external TTL inputs labeled as F2, F3, F4 with F4 the most significant bit and F2 the least. The TTL inputs switch waveforms with 40 ns (two clock cycles) latency between branches and allow the user to switch between waveforms in response to events during the experiment. By tying more than one master to a single TTL, many masters (and their respective slaves) can be run synchronously. Each waveform branch may further be broken up into a sequence of waveform “steps”, where a step is a collection of waveform data run off of a single TTL trigger within the selected branch after which the AWG awaits the next TTL trigger. There is an additional line F5 which can be configured as an input or output and is independent on every master and slave board. The F5 line is currently only used for diagnostics but can potentially be used for additional branches, synchronous output triggers, or an additional input port for counting TTL pulses such as from a PMT. The AWG’s branching lets us functionalize our waveforms to concatenate a basis-set of transport operations that can be triggered on the fly, possibly dependent on experimental results, without the need for delays due to downloading new waveform data.

The gateware is designed to accept command codes which the master FPGA interprets and routes accordingly to the proper master or slave FPGA when the experiment-control computer transmits data. The commands sent from the control computer are listed in Table 5.1. The master routes a line to every connected FPGA to signal that there is incoming data from the FT245RL 8-bit wide transmit buffer. When uploading waveform data to RAM, the user first sets which FPGA to talk with (CMD_FPGAADDR) which is set by an on-board HEX switch from 0 to 15, then sets which specific DAC connected to that FPGA out of three (CMD_SETDACX) that will receive the waveform data. After that, any new data only interacts with the specific DAC channel’s respective RAM.

The starting communication address for writing waveform data can be set to begin at a predefined location (CMD_SETMADDR), such as at the start of a specific branch. When sending waveform data, first the length of bytes to be sent is specified (the length set by CMD_BURST), followed by the stream of data (CMD_WRITEBURST). Branch data points are specific memory addresses that define a memory address register that tells the FPGA where to look for the beginning of waveform data when the respective branch is selected. When the branch input TTLs select a specific branch followed by a run trigger, waveform data is read starting from the respective branch data point up to the next branch or to the maximum address (set by CMD_SETLEN).

5.3.3 Memory Storage

Each channel has on-chip block RAM allocated for its waveform specifications. The interface to the block RAM was generated using the Xilinx Block Memory Generator. The AWG implements a Simple Dual-port RAM diagrammed in Fig. 5.3. This allows two independent ports to the RAM: port A has an input to specify an address at which to write to memory and port B has a separate input to specify an address for reading from memory. The independent addresses allow the option to maintain write and read locations independent of one another. Port A has data written at the RAM address labeled ADDRA, clocked at CLKA, and with data from the FT245RL at DINA so that data transmitted from the experiment-control computer is uploaded to the desired channel's memory when the write-enable line goes high. Port B has data read from RAM at the address ADDRB, clocked at CLKB (for the current gateware, CLKB and CLKA are the same), and with data output at DOUTB, which is interpreted for waveform outputs. It takes two clock cycles to interact with the RAM at a specific memory address for either port. On a given clock cycle, the address is read, and on the following clock cycle, the memory at that address location will be available for input or output. Therefore, care must be taken in the timing to a clock-cycle delay between specifying a memory address and having new data available.

Each channel's RAM can hold 110 kilobits, but this could be rapidly consumed for complex experiments with ion transport. This memory is set for 16-bit wide data that is 6144 memory locations

Command	Hex	Function
CMD_FPGAADDR	00	Sets the address to flag which FPGA is to receive signals from the FT245RL amongst connected PDQ boards
CMD_BURST	01	Sets burst length for how much waveform data will be sent
CMD_SETMADDR	02	Sets the starting communication memory address for writing the waveform to memory registers
CMD_WRITESINGLE	03	Write waveform data
CMD_WRITEBURST	04	Write a stream of waveform data to the memory register with size 'burst length'
CMD_SETLEN	06	Maximum waveform address in the memory register
CMD_MODE	08	Running mode for all the DACs (00, 01, 02, or 03)
CMD_SETDACX	1X	Choices for which of X (0, 1, 2) of three channels for incoming waveform data
CMD_SETBRANCHX	2X	Setting branch memory addresses for each channel where X (0, ..., 7) is the branch number for current DAC

Table 5.1: Commands sent from the control computer to the AWG through the FT245RL USB interface.

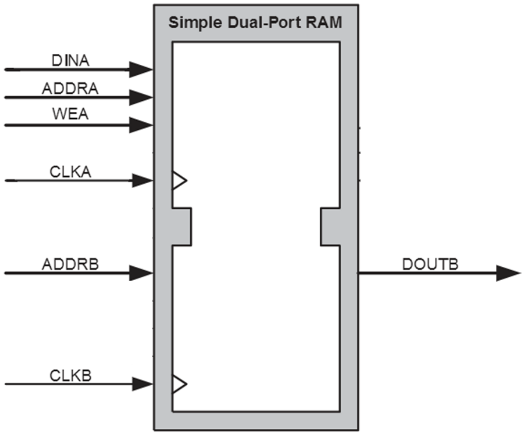

Figure 5.3: Diagram of the Simple Dual-Port RAM input and output interface generated by the Xilinx Block Memory Generator. Port A is used to write to the RAM and port B for reading out the RAM. The CLKA and CLKB clock inputs are both referenced to the same global clock as the rest of the FPGA logic. ADDRA specifies the writing address for data DINA when the write enable line WEA is high, and ADDRB specifies the address for read-out of the RAM data via DOUTB.

deep (each memory location has two parity bits for a total of 18-bit wide data, but this is unused in the current gateware and could potentially be used to hold additional information about a memory location). The 16-bits comprise a pair of 8-bit-wide data transmissions through the FT245RL USB connection. The memory depth corresponds to memory addresses specified with 13-bits, and memory registers include addresses for upload locations in RAM, addresses for reading waveform data in RAM, and the branch-point address register.

In the 4^{th} mode, which uses cubic polynomials to specify waveform outputs, a single cubic polynomial uses ten memory locations. The initial voltage voltage for each channel uses 16 bits for the starting voltage: 0 to 32767 specifies 0 V to 10 V, and 32768 to 65536 specifies the 2's-complement (taking the bit parity flip and adding one) for -10 V to 0 V. The first linear coefficient uses 32 bits with 16 bits of fractional precision. The quadratic and cubic coefficients use 48 bits with 32 bits of fractional precision. The duration for the polynomial is specified in number of clock cycles with 16 bits (up to a 32767×20 ns duration). A 2's-complement duration signifies that the AWG should wait for a TTL trigger before running the next polynomial in memory. Thus, when operating in the 4^{th} mode, up to 614 polynomials can be stored in each channel's RAM.

To convert a real time polynomial,

$$y(t) = a + bt + ct^2 + dt^3, \tag{5.3.1}$$

into a form used by the AWG, the voltage output must be computed using a discrete sum over clock cycles. As such, at the n^{th} clock cycle during waveform output, the coefficients for waveform output are evaluated by the FPGA as

$$\begin{aligned} \gamma_n &= \gamma_{n-1} + \delta \\ \beta_n &= \beta_{n-1} + \gamma_n \\ \alpha_n &= \alpha_{n-1} + \beta_n. \end{aligned} \tag{5.3.2}$$

This corresponds to a voltage output given by

$$V_{out} = \alpha_0 + n\beta_0 + \frac{n(n+1)}{2}\gamma_0 + \frac{n(n+1)(n+2)}{6}\delta_0 \tag{5.3.3}$$

at the n^{th} clock cycle, given initial coefficients α_0, β_0, γ_0, and δ_0. These values are computed from the desired continuous polynomial by the relationships

$$\begin{aligned}\delta_0 &= d\\ \gamma_0 &= (c-d)/2\\ \beta_0 &= b - c/2 + d/6.\end{aligned} \tag{5.3.4}$$

Before uploading these values to the RAM for an AWG channel, these values then must be scaled by the user to the necessary precision for the RAM storage and converted from the input units of volts. The maximum final output voltage of 10 V corresponds to the signed 16 bit number $2^{15} - 1 = 32767$ applied to the input of each DAC. For example, γ_0 is converted as $2^{32}\gamma \times (32767/10\,\mathrm{V})$, with the factor of 2^{32} included for the 32 fractional bits. In the 4^{th} mode, the FPGA expects to read data for a cubic polynomial of a total duration of n_{tot} clock cycles in the sequence α_0, n_{tot}, β_0, γ_0, and δ_0, after which it will interpret the next data as α_0, ... for the next polynomial. For the 1^{st} (, 2^{nd} (, 3^{rd})) mode, data is likewise interpreted as the sequence α_0 (, n_{tot} (, β_0, γ_0)).

5.3.4 Possible Future Implementations

5.3.4.1 Faster DAC Output

The AWG has built-in hardware and protocols for the computer-communication interface, which does not need to change for different output interfaces. Currently, the AD9726 DACs are clocked at 50 MHz, but this can be increased to 100 MHz by configuring the FPGA gateware to derive a 100 MHz internal clock from the input 50 MHz oscillator and correspondingly clock the DACs at 100 MHz. Additional speed can be attained from using an interpolating DAC. Such DACs, for example the Texas Instruments DAC5681Z, can further up-convert the clock frequency internally to interpolate between the user-specified voltage values faster than otherwise possible from the FPGA update rate. For such a feature, however, the PCB design for the AWG must be updated for the new DAC pin connections.

The AD8250 amplifier is specified to have approximately a factor of 5 slower speed than the fastest DAC response-time. To obtain a faster DAC signal, two options are available. One is to bypass the amplifier entirely, directly accessing the dual-ended DAC output (this approach has been implemented on some AWGs to feed the outputs directly to an external amplifier). The other is to choose a different on-board amplifier. The AD8250 was one of the fastest options at the time of the AWG's creation. However, there are faster amplifiers now available, such as the Analog Devices ADA4895, and this could be implemented to further speed up the overall AWG output speed.

5.3.4.2 Use as a DDS Source

The uploaded waveform data to the AWG could be chosen in such a way to behave as a sine look-up table in block RAM to be used to generate an RF signal, limited by acceptable sampling rates and the FPGA update rate (for example, a properly well-defined signal must be a divisor of the DAC update rate). This will generate a fixed-phase sine wave, and could possibly be used to inject RF on a trap electrode super-imposed on the confining voltage signal. However, a superior approach would be to alter the AWG to replace the three DAC channel outputs and instead use an array of DDSs. This would require reconfiguration on both the hardware and VHDL level.

The AWG could be re-configured to generate a sequence of RF signals by storing sequences of phase and frequency settings in block RAM to be sent to dedicated DDS chips. The computer-communication methods already in the AWG gateware may remain fixed for transmitting data and uploading data to RAM. The AWG has 48 LVDS bits (currently to control the three DAC output channels); with suitable changes to the traces on the PCB, the final AWG output can replace outputs to DACs for arbitrary signals with outputs to DDSs for phase and frequency settings. The AWG can be used to control a sequence of RF signals by updating phase and frequency settings derived from block RAM. The available 48 LVDS bits can be distributed amongst DDSs as needed (offering the choice of more bit precision vs. number of DDS channels per board; the current experiment-control system uses 8-bit precision DDSs in addition to phase settings which is typically suitable for our needs). The interpretation of block RAM for the final output from the FPGA to the DDS chips must be altered in VHDL, and an additional physical input line would be needed for a reference clock to the DDSs. This would allow an experimenter to control many DDSs per USB connection.

5.3.4.3 Expanded Memory

Future demonstrations of scalable QIP will possibly require very complex and lengthy transport sequences. If experiments require an expansion in available memory on the AWG beyond that already provided by data-compression via cubic splines, there are more efficient uses of the block RAM. The current way that polynomials are stored in memory is by specifying polynomial coefficients with units of numbers of clock cycles, which are summed each clock update to calculate the proper output. This satisfies the current fractional precision necessary for most waveform uses. Memory storage could be made more efficient if it is known in advance if less fractional precision in the coefficients is necessary for experiments. For example, very rapidly-changing polynomials could remove the lowest elements of fractional precision to free up memory. For sufficiently small higher-order polynomial terms, memory can also be saved by only operating in 2nd or 3rd modes of operation. The memory usage could be made more efficient by replacing the coefficients with voltage updates per some number of clock cycles. For example, the quadratic coefficient γ can be a 16 bit value added to the desired voltage output V_{out} every n_γ clock cycles. This would eliminate the need for any fractional storage in each channel's RAM, which could reduce the required memory to specify a cubic polynomial to eight memory locations deep rather than ten.

5.3.5 Experimental Implementations

5.3.5.1 Driving Filtered Electrodes

The high update rates of the AWG relative to confinement frequencies in our traps enables variation of electrode potentials for ion transport on timescales faster than the ion oscillation period. In ion transport experiments, the AWG produced the time-varying electric potentials in a multi-electrode linear Paul trap (diagrammed in Fig. 5.4a). These experiments demonstrated that transport and separation over distinct trap zones on quantum logic time scales can be performed with suppressed excitation in the trapped ions' final motional state.

A complication arises from a chain of resistor-capacitor (RC) low-pass filters that is applied to each electrode to reduce electric field noise from external sources at the trap frequencies. To achieve the high speed of the fast ion transport waveforms, we must precompensate for the low-pass effects of the filters in order to achieve the desired time-dependence of the electrode potentials [75]. The filters for each electrode in the quantum logic trap, from AWG-side to trap-side, are a pair of 200 kHz low-pass RC filters followed by one 800 kHz low-pass RC filter for our quantum logic ion trap, which have resistors {R_2, R_1, R_0} = {820, 820, 240} Ω and capacitors {C_2, C_1, C_0} = {1, 1, 0.82} nF. The input potential V_{input} to a single stage of the RC filters in the filter chain are related to the desired output potential V_{output} by

$$V_{input} = V_{output} + R_i C_i \frac{dV_{output}}{dt} + (V_{output} - V_{prev}) \frac{R_i}{R_{prev}}, \tag{5.3.5}$$

where R_i and C_i are the RC component values of the i^{th} layer of the filter chain and V_{prev} and R_{prev} are from the solution to the previous layer of filtering trap-side. One example of numerically solving for the effects of the filter system is shown in Fig. 5.4b. However, this approach is ultimately limited by the maximum voltage output and amplifier speed, so it cannot be done arbitrarily fast. The transport waveforms altogether in Ref. [66], including that shown in Fig. 5.4b, were specified by cubic splines that occupied ~ 6 % of each channel's memory.

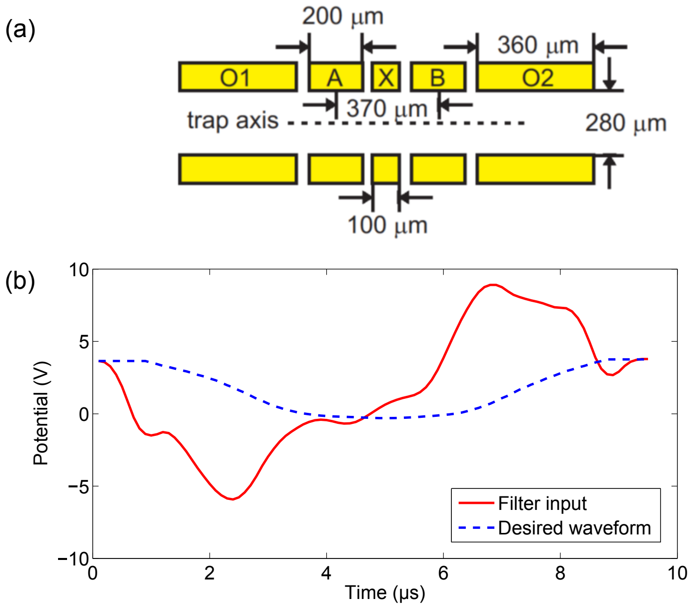

Figure 5.4: (a) Schematic of the ion trap electrode structure showing the two diagonally opposite segmented DC electrodes (not to scale). Outer electrodes O1 and O2 are used to fine tune the potential while ions move over electrodes A, X, and B during the experiments in Ref.[66]. (b) Example filter compensation for electrode X during transport of an ion from over electrode A to over electrode B. The desired waveform is generated from simulation and the potentials generated by the AWG must account for filter distortion. The waveform from the AWG must overshoot in voltage to achieve the desired 8 μs transport potentials. Reproduced from Ref. [74].

5.3.5.2 Waveform branching

The capability to quickly switch between waveform branches allows complex sequences of waveforms to be built up from a series of simpler component waveforms. For example, the experiments in Ref.[28] required multiple instances of two ^{9}Be^{+} qubit ions undergoing operations with quantum logic in a shared trap zone for two-qubit operations and the separation of the ions to distinct zones for one-qubit operations. The full sequence required as many as 16 separation and recombination waveforms in a single experiment. We used three waveform branches preloaded into AWG memory and selected with TTL inputs during the experiments: (1) the static trap potential, (2) the separation waveform, and (3) the recombination waveform. Because the three waveforms are reused and need to be combined in various sequences, we can define the corresponding branch for each waveform and the experimental sequences of these three waveform branches were concatenated on the fly without the necessity to upload a new set of waveforms for each sequence.

5.3.5.3 Shaped Microwave Pulses

Microwaves can be used to drive transitions between hyperfine states. In one implementation, the AWG was used for pulse shaping of a microwave signal at ~ 1.69 GHz that drives the $|S_{1/2}, F=3, m_F=1\rangle \longleftrightarrow |S_{1/2}, F=2, m_F=1\rangle$ hyperfine transition in ^{25}Mg^{+}. For the experiments in Ref. [76], the AWG was used to prevent ringing of high power ($\sim$45 dBm) pulsed microwave signals during turn on/off by shaping the pulse with a smooth rise and fall. In this case, the microwaves were ramped on and off in 10 μs. A multiplier combines the AWG shaping waveform and the microwave signal into a shaped microwave pulse, which is then amplified. Resonances for the hyperfine transition, shown in Fig. 5.5, taken by varying the frequency of the microwave signal followed by a state-dependent fluorescence measurement, are demonstrated for two cases: a rectangular pulse shape (Fig. 5.5a), and a Gaussian pulse shape (Fig. 5.5b). The transition profiles are related to the Fourier transform of the pulse shape, a sinc^2 and a Gaussian, respectively, with pulse durations chosen for approximately equal full width at half max for each profile.

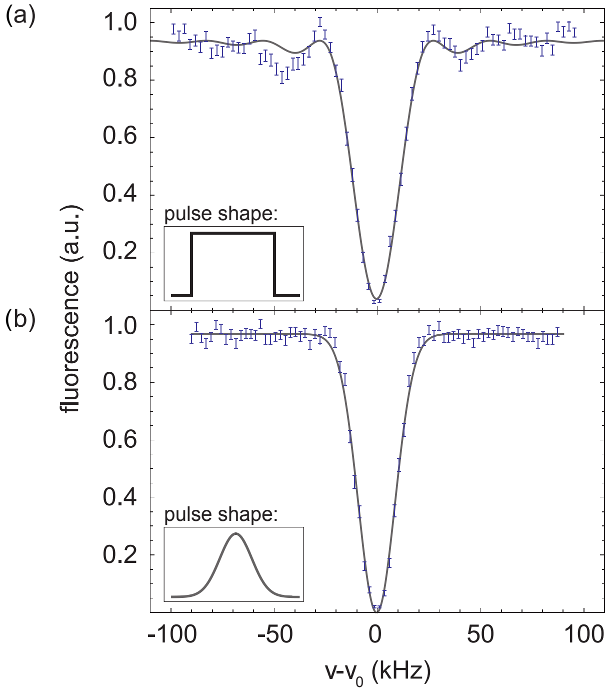

Figure 5.5: Pulse shaping of a microwave signal using the AWG to specify the profile. The microwave drives the hyperfine transition in ^{25}Mg^{+}. Shown is the ion fluorescence in arbitrary units vs. microwave frequency. Here $\nu_0 \sim 1.69$ GHz denotes the frequency splitting of the two hyperfine levels. (a) Observed sinc^2 lineshape from a rectangular pulse shape for a 20 μs duration. (b) Observed Gaussian lineshape from a Gaussian pulse shape. The FWHM pulse duration was 45 μs, with the Gaussian tail truncated to a total duration of four times the FWHM. Reproduced from Ref. [74].

5.3.5.4 Laser Pulse Shaping and Stabilizing

As the ion-laser interactions are typically pulsed, our pulse sequencer switches laser beams on and off as needed. For some applications, greater control over the optical pulse amplitude is desired. Laser intensity noise can be a source of error both singe-qubit Rabi oscillations and in laser-driven two-qubit entanglement. We use a feedback loop to measure the laser intensity and control it. However the feedback loop doesn't behave well when we just switch it on instantaneously to do a square pulse. One way to deal with this problem is to ramp the laser on and off smoothly so the feedback loop can follow and stay locked.

To this end, we use the Analog Devices AD5390 vector multiplier which can be used as a quadrature amplitude modulator, or sometimes known as an I/Q modulator. These modulators have a local oscillator RF signal with two RF input ports and two DC control "I" and "Q" input ports, where I and Q are components which give an amplitude and phase offset in the complex plane. The ADL5390 was chosen for its frequency range and linear amplitude response to the inputs. The signal sent to the modulator's I port is determined by the output of an analog proportional-integral (PI) servo with an integrator hold capability. The PI is configured to minimize $|V_+ - V\text{-}|$, where V_+ is a signal from a photodiode derived from the laser beam and V_- is an output channel of the AWG. Laser beam attenuation is controlled by utilizing the -1 diffracted order of the AOM for the laser in a double-pass configuration. When a laser pulse is desired, the servo's response to a pulse shape from the AWG into the V_- port drives the I port of the I/Q modulator, thereby increasing the amplitude of the RF signal fed into the AOM. Noise within the bandwidth of the servo is attenuated as the laser beam increases intensity to its maximum value. The RF signal is switched off when the beam is not in use.

Chapter 6

Coherent Transport Dynamics of Trapped Ions

The large timescale discrepancy between the time it takes to perform quantum logic ($\sim 10\mu$s per operation) and to perform transport and recooling ($\sim$1-2 ms per operation) in previous demonstrations of our QIP architecture [29, 27, 28] are unacceptable in large-scale QIP. Previous ion transport experiments, such as those in Refs. [12, 15], have demonstrated cold transport with adiabatic transport durations, that is, much longer than the period of oscillation for the trapped ion. Excitations, due to non-ideal transport waveforms and accumulated thermal heating in our traps, made more significant for longer transport durations [24, 25, 26], degrade our two-qubit entanglement through the shared motion. Finite qubit coherence times also contribute to imperfect entangling-gate fidelity that can surpass acceptable error levels accrued during long operation times (practical fault-tolerant entangling gate errors typically are cited as having a threshold of 10^{-4} [77, 78]). It is critical to reduce QIP operation time well-beneath qubit coherence times. Therefore, it is a requisite that ion transport durations are at least on timescales comparable to quantum logic, and that transport is performed with mitigated motional excitations to reduce overhead from recooling.

Transport is performed by applying time-varying potentials, or “waveforms,” to the ion trap electrodes. For significantly short transport durations, diabatic excitation effects due to accelerations can become significant. Additionally, former limitations in commercially available DACs that were used to supply waveforms could cause unwanted excitations. Harmonics of the update rate, with a fundamental frequency of $\simeq 500$ kHz, could have Fourier components at the ions’ axial frequencies and thus cause motional excitations during transport [15]. During ion separation or recombination, the axial frequencies could go quite low and cross through a resonance of the fundamental or harmonics of the DAC update rate, which can also lead to undesirable excitations. With sufficiently fast and precise DACs for transport, the steps in the potentials can be approximately continuous with respect to the ions' motion. The electronics to generate the waveforms in the experiments described here were supplied by the arbitrary waveform generator with a 50 MHz update rate described in Chapter 5. This allows waveforms that approximately match any position profile for transport, and the motion can be coherently excited and de-excited with timing precision on timescales faster than ion trap periods.

This chapter discusses the experimental results towards improvements on ion transport characterized by both orders-of-magnitude faster timescales over former implementations as well as highly-mitigated motional excitations. I begin with an overview of some experiments with ion transport prior to my research, which was generally in the adiabatic regime, followed by a description some of the theoretical treatments for speeding up ion transport in ways that consider limited motional excitations on fast timescales. The theoretical discussions include that for separating two ions into distinct trap zones, which necessarily includes changing the axial trap frequencies. I will then describe my experimental results for coherent diabatic transport of one and two ^{9}Be$^+$ qubit ions between two trap zones and the separation of two ^{9}Be$^+$ ions into distinct trap zones on timescales comparable to quantum logic durations and with mitigated motional excitations. I also discuss the diabatic transport of two-species ion chains. These results pave the way for ion-based scalable QIP, combining all the building blocks in a way that can potentially have information processing timescales well beneath acceptable coherence-time limitations.

6.1 Adiabatic Ion Transport

The faster that ions are transported, as durations approach timescales comparable to the axial trap periods, the more that motion can be coherently excited due to fast accelerations. If transport durations are much slower than the trap periods, referred-to as “adiabatic transport”, then excitations will be mitigated. A multi-electrode wafer trap was the earliest platform for ion transport [12]. A ^{9}Be$^+$ ion was transported with a position profile of $z(t) = \sin^2(\pi t/2T) \times 1.2$ mm, T the total duration, traversing an intermediate electrode, with varied velocities in a 2.9 MHz well. When $T \sim 50\mu$s, for example, the timescales were much longer than the motional period and thus the transport was adiabatic, and in turn motional excitations along the axis were ~0.01 quanta. However, as durations were decreased, as low as $T \sim 20\mu$s, large motional excitation was observed to the point of being difficult to measure the number-state occupation. The trap from these experiments also had a "separation wedge" electrode which was 800 μm wide. Two ions were brought over this electrode and split into two separate trap regions with a 95 % success rate. The final motion incurred a great amount of motional excitation and separation was not perfectly reliable, though it had promise for splitting a two-ion chain into spatially distinct wells.

Transport through a T-junction in an ion trap was reported in Ref. [13] with ^{112}Cd$^+$ and transport through the junction in the X-junction Trap with ^{9}Be$^+$ was reported in Ref. [67], demonstrating that ions can traverse a junction in the electrode architecture to allow a which-way transport for ion re-ordering. Low-excitation ion transport through the X-trap's junction was achieved in work reported in Ref. [67] and improved upon in Ref. [15]. Here, ions entering the junction and exited at either 0° or 90° degree angles from the incident trajectory and transported back to the starting position with average velocities of 2 m/s over a ~1 ms duration and only incurred ~0.2 quanta excitation, which is promising for future scalable QIP implementations.

In Ref. [22], a similar trap design to the quantum logic trap was used in a demonstration of quantum teleportation between qubits which involved the separation of ions. A crystal of three ^{9}Be$^+$ qubit ions underwent various stages of separation and combination along with several entanglement steps. The success of the teleportation experiment depended heavily on two-qubit entanglement operations not degrading due to accumulated motional excitations in the shared motion. In those experiments, only 0.1 quanta of excitation was seen in the stretch mode of motion in a two-ion crystal after a separating three ions into groups of one and two in distinct trap zones across a 1 ms separation duration. The separation wedge was 100 μm wide, and the improved separation result compared to that in [12] was attributed to the relatively narrower separation wedge electrode.

Several theoretical considerations have been made towards ideal ion transport. Optimal adiabatic transport was investigated in Ref. [79] by looking at the quantum dynamics of the forced harmonic oscillator. A number of time-varying transport profiles were analyzed, with one of the most interesting results due to the error function transport, where $\mathrm{erf}(t) = \frac{2}{\sqrt{\pi}} \int_0^t e^{-t'^2} \mathrm{d}t'$ is the standard error function. This was calculated to be a highly effective adiabatic profile for a suitably precise waveform for timescales down to small numbers of trap periods. However, in Ref. [23], transport at high speeds was demonstrated with an error function profile on timescales under 4 trap periods for $^{40}\mathrm{Ca}^+$ ions, and resulted in final excitations outside the adiabatic regime with a 1% ion loss rate, necessitating the development of rapid transport with a higher success rate. Simulated analysis of trap designs that are optimal for transport in conjunction with optimal transport waveforms have been carried out as well [80].

Even under perfect adiabatic transport, it may not be possible for the ions' motion to remain ground-state cooled across QIP operations due to ambient heating [24, 25, 26] (our systems have typical heating rates of $\dot{\bar{n}} \sim 0.5$ quanta/ms). Our solution to the acquisition of motional excitations during transport and heating effects arose out of sympathetic cooling. Our qubit ions, $^9\mathrm{Be}^+$, can share a trap zone with a $^{24}\mathrm{Mg}^+$ or $^{25}\mathrm{Mg}^+$ coolant ions during transport. In [81], work with the quantum logic trap brought together all the building blocks for scalable QIP which involved separation, recombination, and sympathetic cooling in traps which held both Be^+ and Mg^+ ions. However, an additional latency arises due to sympathetic cooling, as the ground-state cooling method also required roughly 1 - 2 ms of cooling time. Having both qubit and coolant ions to sympathetically cool motional excitations acquired due to imperfect transport and ambient heating rates in the trap is an added consideration for rapid transport with multiple ion species.

6.2 Coherently-driven Ion Transport

One approach to rapid ion transport is to find transport profiles which stay adiabatic on timescales down to a few trap oscillation periods at high speeds such as discussed in Ref. [79], which includes an error function profile. There have been several theoretical investigations on diabatic transport with minimally excited final states, including optimized electrode and transport potential analysis [80, 82]. An approach to perform diabatic transport is to coherently excite and de-excite the motion across the waveform by engineering transport waveforms with suitable accelerations with no net excitation at the transport destination. As long as the harmonic trap frequency ω is held constant, excitations will always be coherent. Precise transport requires varying the confinement potential in a way that approximately matches the theoretical transport profile with respect to the trapped ions, which is accomplished with our arbitrary waveform generator with a 50 MHz update rate (see Chapter 5), and this also allows us to control the transport timing with precision much faster than the trap oscillation period. For an ion with mass m, trap frequency ω, and with a transport profile $z_0(t')$, then the coherent state amplitude α is given by [83]

$$\alpha(t) = \sqrt{\frac{m\omega}{2\hbar}}\left(-e^{-i\omega t}\int_0^t \dot{z}_0(t')e^{i\omega t'}dt'\right). \tag{6.2.1}$$

That is, as long as the Fourier component of $\dot{z}_0(t')$ at the trap frequency vanishes when integrated over the transport duration, the ion will end up in its initial state at the destination $z_0(t)$. The simplest case is for the trapped ion to suddenly move with a constant velocity v and then stop after a total transport duration t_T ($\dot{z}_0 = 0$ for $t < 0$ and $t > t_T$, and $\dot{z}_0 = v$ for $t \in [0, t_T]$). This gives us

$$\alpha(t_T) = \sqrt{\frac{m\omega}{2\hbar}}\left(i\frac{v}{\omega}\left[1 - e^{-i\omega t_T}\right]\right). \tag{6.2.2}$$

For an ion initially in the ground state of motion, then for the condition that $\omega t_T = 2\pi N$, N an integer, the ion returns the ground state at the destination. This is similar to an approach using step-wise accelerations of neutral atoms in [84] performing transport on the 1 s timescale. For non-integer N, the ion will be left in a coherent state different from the ground state. Due to the finite response times of our trap electrode filters and drive electronics, sudden starts and stops are not practical. Nevertheless, Eq.(6.2.1) gives a criterion for transport functions with low excitations at the destination. In the case of multiple same-species ions, there will be no differential force, so only the common mode of motion needs to be considered so that in principle this approach is effective for many ions.

Considering transport for multi-species ion chains requires more careful consideration due to the potential for excitations of all normal modes of motion. The work in Ref. [85] produced a theoretical treatment for multi-species ion transport with no residual excitations, with specific attention to the case of ^{9}Be$^+$ and ^{24}Mg$^+$. Under transport which coherently drives the motion, the out-of-phase normal mode of motion will be excited, unlike in the same-species case. One approach decomposes the transport profile into a finite-length Fourier series, such that the coefficients are used as degrees of freedom to solve for ideal transport with the constraints that $z(0) = z_i$, $z(t_T) = z_f$, $\dot{z}(0) = 0$, $\dot{z}(t_T) = 0$, and that the integral for coherent excitations for each mode ω_j proportional to $c(\omega_j) = \int_0^{t_T} \dot{z}(t) e^{i\omega_j t} dt$ vanishes. The position profile,

$$z(t) = (z_f - z_i) \times (\frac{1}{2} + \sum_{l=1}^{N_{ions}+2} a_l \cos[\frac{\pi(2l-1)t}{t_T}]) + z_i, \tag{6.2.3}$$

is used to satisfy $N_{ions} + 2$ conditions for N_{ions} normal modes, and already has the property that $\dot{z}(0) = \dot{z}(t_T) = 0$. The constraint to eliminate coherent excitations is imposed by having each coefficient a_l proportional to the term

$$c_l(\omega_j) = -\frac{\pi(2l-1)}{t_T} \int_0^{t_T} \sin[\frac{\pi(2l-1)t}{t_T}] e^{i\omega_j t} dt, \tag{6.2.4}$$

and that $\sum_{l=1}^{N_{ions}+2} c_l(\omega_J) a_l = 0$. The linear system of equations to solve for the coefficients becomes

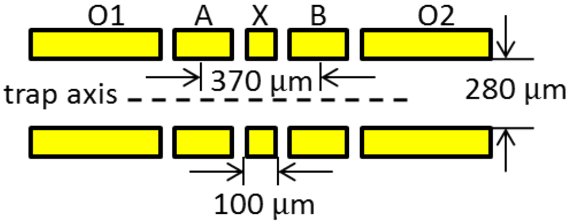

Figure 6.1: Schematic of the electrode structure for the diagonally-opposite DC electrodes of the quantum logic trap. During experiments, the ions are separated and recombined in zone X, and transported between zones A and B. The waveforms consist of time-varying potentials, with common potentials for each diagonally-opposite pair of electrodes.

$$\begin{bmatrix} 1 & 1 & 1 & \ldots & 1 \\ 1 & -1 & -1 & \ldots & -1 \\ 0 & c_1(\omega_1) & c_2(\omega_1) & \ldots & c_{N_{ions}+2}(\omega_1) \\ \vdots & \vdots & \vdots & \vdots & \vdots \\ 0 & c_1(\omega_{N_{ions}}) & c_2(\omega_{N_{ions}}) & \ldots & c_{N_{ions}+2}(\omega_{N_{ions}}) \end{bmatrix} \begin{bmatrix} 1/2 \\ a_1 \\ a_2 \\ \vdots \\ a_{N_{ions}+2} \end{bmatrix} = \begin{bmatrix} 0 \\ 1 \\ 0 \\ \vdots \\ 0 \end{bmatrix}. \tag{6.2.5}$$

This method assumes that the excitations during transport are small enough such that the ion motion remains in the harmonic regime, and does not lead to significant higher-order terms due to the Coulomb coupling.

6.3 Transport of ^{9}Be$^+$ Experiments and Results

Single-species ion transport experiments were carried out in the quantum logic trap (Fig.6.1). We initialized a single ^{9}Be$^+$ ion in zone A in a trap with an axial frequency of $\omega/(2\pi) \simeq 2\,\mathrm{MHz}$ with trap potentials $\{\mathrm{V_{O1}}, \mathrm{V_A}, \mathrm{V_X}, \mathrm{V_B}, \mathrm{V_{O2}}\}$ = {1.289, 0.327, 2.173, 0.310, 1.311} V). The axial motion was Raman sideband laser-cooled to initialize the motion to $\bar{n} \simeq 0.1$ and optically pumped and initialized to the qubit state $|F = 2, m_F = 1\rangle = |\downarrow\rangle$ of the ^{9}Be$^+$ $S_{1/2}$ manifold with magnetic field $B \simeq 11.9$ mT. It was then transported 370 μm in a total transport duration $t_T \approx 8\,\mu$s to zone B (A $\rightarrow$ B), with a velocity $v \simeq 46$ m/s, with a waveform that approximated the conditions for Eq. 6.2.2.

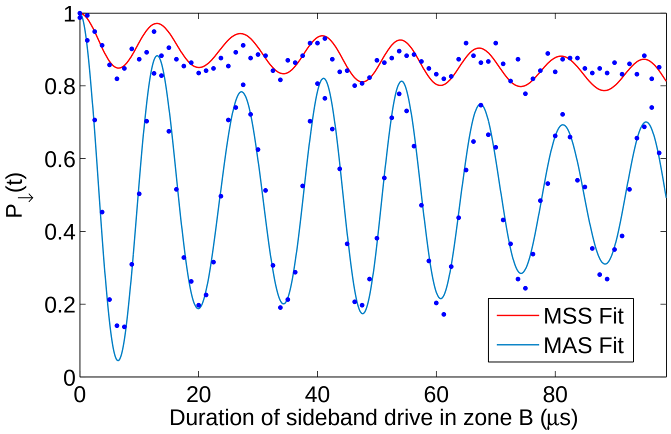

Figure 6.2: Rabi flopping trace on the MAS and MSS after transport from zone A to B. Here we fit to thermal distributions that give $\bar{n} = 0.19 \pm 0.02$ from the MAS fit and $\bar{n} = 0.17 \pm 0.01$ from the MSS fit. The axial frequency was $\omega/(2\pi) = 1.972(1)$ MHz with a Lamb-Dicke parameter $\eta = 0.479$. Reproduced from Ref.[66].

We varied ω by applying a single, universal scaling factor to our electrode voltages to optimize the transport and found $\omega_{Opt}/(2\pi) = 1.972(1)$ MHz to minimize coherent excitations.

Following A $\rightarrow$ B transport, qubit sideband transitions were driven in zone B on the $|2,1\rangle \longleftrightarrow |1,0\rangle$ transition. The ion was then transported back to zone A (B $\rightarrow$ A) to determine $P_{\downarrow}(t)$ through state-dependent resonance fluorescence [57]. As an approximation, we fit to the function

$$P_{\downarrow}(t) = \frac{1}{2}\left[1 + e^{-\gamma t}\sum_{n=0}^{\infty} P_n \cos(2\Omega_{n\pm1,n}t)\right], \tag{6.3.1}$$

which is the function from Chapter 3 Eq. 3.4.2 including a phenomenological decay rate γ. The final excitations were consistent with the trap's ambient heating rate, with a minimal final state measured as having $\bar{n} = 0.19 \pm 0.02$ from the MAS fit and $\bar{n} = 0.17 \pm 0.01$ from the MSS fit, corresponding approximately to $N = 16$ (Fig.6.2). Excitation was also minimized for values of $\omega/2\pi$ differing from ω_{Opt} by integer multiples of t_T^{-1}.

We also transported two $^{9}\mathrm{Be}^{+}$ ions (A $\rightarrow$ B) in the same well. If the potential well is maintained at constant frequency throughout the waveform, there is no differential force on same-mass ions, and the center-of-mass (COM) mode should be excited as for a single ion while the

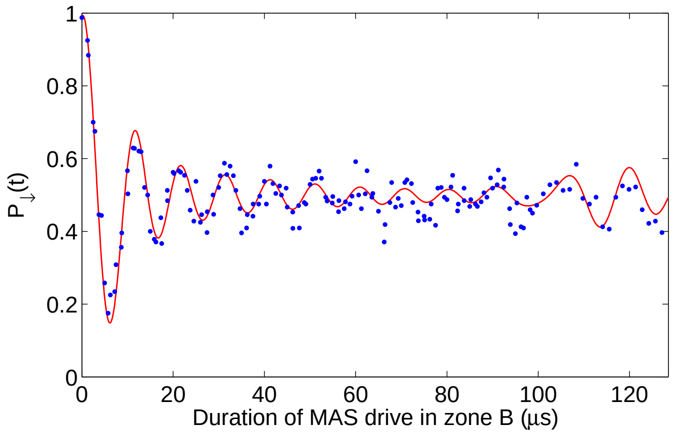

Figure 6.3: Rabi flopping trace on the MAS following transport in which $\alpha(t_T) \neq 0$. The figure shows a coherent state fit with $\bar{n} = 6.4 \pm 0.2$, corresponding to $|\alpha| = 2.53 \pm 0.04$. The axial frequency was $\omega/(2\pi) = 1.919(2)\,\mathrm{MHz}$ and the Lamb-Dicke parameter was $\eta = 0.486$. Reproduced from Ref.[66].

“stretch” mode of motion (the normal mode for out-of-phase amplitudes with frequency $\omega_{str} = \sqrt{3}\omega$) should not be excited. We initialized both modes to $\bar{n} \simeq 0.1$ and after transport, we observed $\bar{n}_{COM} = 0.35 \pm 0.1$ with negligible excitation of the stretch mode.

For non-optimal values of $\omega/(2\pi)$, $P_\downarrow(t)$ measurements showed that the populations of the final motional states were consistent with a coherent state of motion; however, these measurements do not verify the coherences between number states. To verify that the transport excites a coherent state, we implemented A → B transport in a well of frequency $\omega/(2\pi) = 1.919(2)$ MHz to try to maximize $\alpha(t_T)$ in zone B, corresponding to approximately $N = 15.5$ and a state with $\bar{n} = 6.4 \pm 0.2$ from a MAS fit (Fig.6.3). We then applied a uniform electric field $E_z = E_0 \cos(\omega t_\mathrm{E} + \phi_E)$ for a phase-space displacement α_E to remove the coherent excitation from diabatic transport as an RF de-excitation. This was followed by a MAS drive of duration t, and then B → A transport to determine $P_\downarrow(t)$. By adjusting E_0, t_E, and ϕ_E (relative to the time when transport started), we could make $\alpha_E = -\alpha(t_T)$. Under these conditions, we measured a final state at $\bar{n} = 0.19 \pm 0.02$, consistent with our heating rate and our best optimized cold transport.

When $\alpha(t_T) \neq 0$ in zone B, by waiting an appropriate delay time $T_d \pm N 2\pi/\omega$ in B, and then

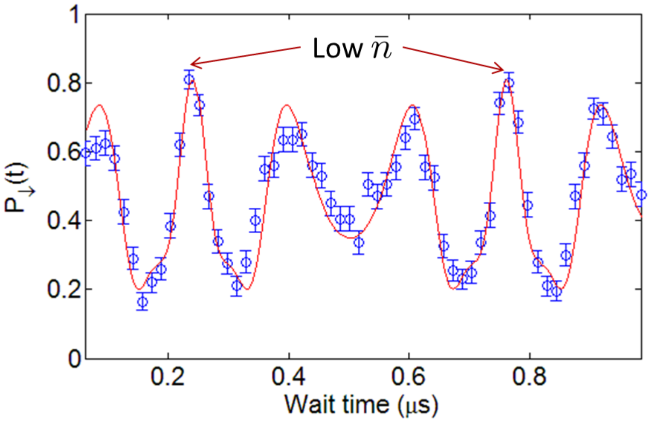

Figure 6.4: Fixed MSS drive time t after A $\rightarrow$ B $\rightarrow$ A “cold” transport for different wait times in zone B. The points at which $P_\downarrow(t)$ changes the least indicates a higher $n = 0$ component of the final motion. The difference in wait time between low $\bar{n}$ features is consistent with ω for our maximal coherent drive.

reversing transport B $\rightarrow$ A, the ion would be returned to its ground state in A (A $\rightarrow$ B $\rightarrow$ A "cold" transport). By varying the wait time T_d and applying a motion-subtracting sideband drive of fixed duration t_{MSS} set to the π/2 time for an ion with $\bar{n} = 0$, we could observe the interactions of the coherent states driven between A $\rightarrow$ B transport and B $\rightarrow$ A transport. The variation in $P_{\downarrow}(t_{MSS})$ as T_d is varied indicates a change in the final motional state in zone A, where the smallest change in $P_{\downarrow}$ corresponds to the ion returning to near its ground state, shown in 6.4.

It is necessary that qubit coherences are reliably maintained during transport, a feature demonstrated in Refs.[12, 15]. Under transport with minimal final excitation we can expect that since any number state receives the same phase-space displacement across the transport, initial motional states should maintain the same relative coherences before and after transport. To demonstrate this, we performed a Ramsey-type interference experiment in which the qubit and motion are entangled. After state initialization, a MAS $\pi/2$ pulse was applied to transform the initial state $|\downarrow, n = 0\rangle$ to the qubit-motion entangled state $\frac{1}{\sqrt{2}}(|\downarrow, n = 0\rangle + |\uparrow, n = 1\rangle)$. To establish a baseline reference, we performed a Ramsey experiment with free precession time approximately equal to the transport duration, but with the ion held stationary in zone A, with a measured a fringe contrast of 85(2)%, limited primarily by imperfect initial ground-state cooling and our relatively large Lamb-Dicke parameter. The Ramsey experiment with A $\rightarrow$ B $\rightarrow$ A transport between Ramsey pulses, both transport steps under optimized transport, resulted in a measured 86(2)% contrast, which was consistent with no loss in coherence of the qubit-motion entangled state (Fig. 6.5).

6.4 Ion Separation

The theoretical treatment to our approach to ion separation, which is an inherently adiabatic approach, was described in Ref. [86], including analysis of optimal potentials and ion trap geometries for separation. Some of the theoretical basis for separation was expanded upon in Ref. [87]. When separating multiple ions confined in a single zone into two separate zones, it is impossible to preserve the motional mode frequencies. To lowest order, the required external potential can be

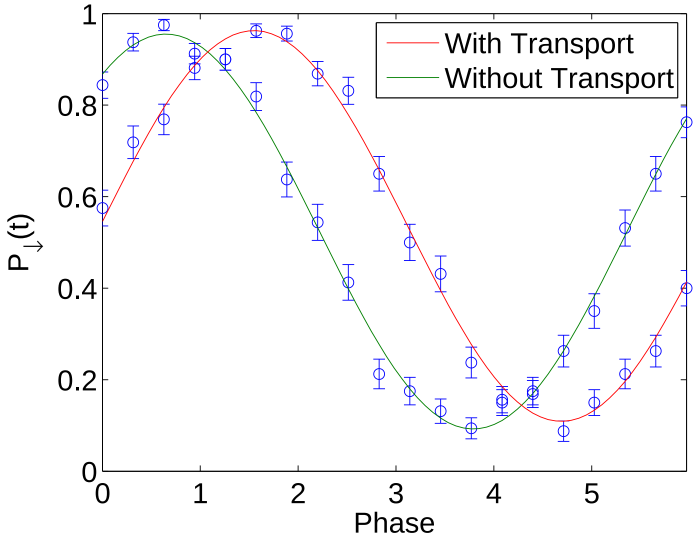

Figure 6.5: Ramsey-type interference experiment with MAS $\pi/2$ pulses in zone A. The contrasts without transport (contrast of 85(2)%) and with transport (contrast of 86(2)%) are consistent with no loss in coherence. The phase offset is due to imperfect matching of the delays between the two MAS pulses for the case with transport and the case without.

described as the sum of a quadratic and a quartic term for $0 \leq t \leq t_s$ for total separation duration of t_s, given by

$$U(z) = a(t)z^2 + b(t)z^4, \tag{6.4.1}$$

with $a(0) > 0$, $b(0) = 0$ and $a(t_s) < 0$, $b(t_s) > 0$. Due to the Coulomb repulsion between the ions, the normal modes remain harmonic throughout the separation for small excursions about each ion's local minimum. The inter-ion equilibrium distance $d(t)$ during the separation process is given by the real solution to [86]

$$b(t)d(t)^5 + 2a(t)d(t)^3 = \frac{q}{2\pi\varepsilon_0}. \tag{6.4.2}$$

Two same-species ions will have two axial frequencies, the COM and stretch modes, respectively given by

$$\omega_1^2 = (2a(t) + 3b(t)d(t)^2)q/m \tag{6.4.3}$$

$$\omega_2^2 = \omega_1^2(1+\varepsilon) \tag{6.4.4}$$

where $\varepsilon = q^2/(\pi\varepsilon_0 m\omega_1^2 d(t)^3)$ [86]. The COM and stretch normal mode frequencies go through their minima near the point when a vanishes, at which point the external potential is mostly quartic. For very large inter-ion distances, the two modes are equal; that is, the ions are in reasonably independent wells with frequencies $\omega_1 \simeq \omega_2$.

The separation waveform comprises two main segments. The ions began in a shared trap at the center of electrode X with respect to Fig. 6.1. For the first segment, $a(t)$ was decreased and $b(t)$ increased by lowering the potentials on electrodes A and B while simultaneously increasing the potentials on outer electrodes O1 and O2 until the mode frequencies approximately reach their minimum values. The potential for electrode X was also lowered to a value which was simulated to minimize the trap's potential curvature. In the second segment, the $a(t)$ term passes through a zero-crossing through the application of an increasing potential on electrode X to produce a separating wedge potential (or simply a “wedge”). The final value of electrode X for producing the wedge is the result of simulating a step-wise increase on electrode X, iterated until suitably-separated wells are found. The spatial extent and precision of the wedge is governed by the ion-to-electrode distances; therefore, smaller trap electrode sizes and ion-to-electrode distances can maintain stronger confinement and produce a narrower wedge, which could lead to reduced excitations. Higher maximum voltages on electrodes could also maintain stronger confinement.

During separation, diabatic changes in both the curvature and equilibrium ion positions of the axial potential can lead to coherent displacement of the motional states. Both the inter-ion distance and the frequencies have an inter-dependency, so controlling the rate of change in frequency also controls the relative velocities between the ions. The largest excitation during separation coincides with roughly the time at which the value for $a(t)$ changes sign. Initially, the waveform voltages during the first segment were ramped with $\sin^2(\pi t/2T)$ for duration T between initial and final values. The second segment linearly ramped the potential on electrode X to its final value. To suppress excitations, we approximated the adiabatic condition for ramping a harmonic well, $\frac{1}{\omega^2}\frac{d\omega}{dt} \ll 1$ [88], where ω here corresponds to ω_1 of Eq. 6.4.3. We numerically solved for $\frac{1}{\omega^2}\frac{d\omega}{dt}$ across the waveform and imposed a maximum value of $\frac{1}{\omega^2}\frac{d\omega}{dt} = 0.025$ for the COM mode during the ramp-down of the harmonic well and $\frac{1}{\omega^2}\frac{d\omega}{dt} = 0.015$ around the sign change of $a(t)$ in Eq. 6.4.1 to shape the waveform to a more adiabatic form, with the results shown in Fig. 6.6. Simulations for the ion positions and frequencies as a function of time are shown in Fig. 6.7.

6.5 Separation of Two ^{9}Be$^+$Experiments and Results

We ran a separation waveform (duration $\simeq 340\mu$s) to partition a linear chain of nine $^9\mathrm{Be}^+$ ions into two chains with all possible number combinations. We first Doppler cooled the chain in zone A and optically pumped to $|\downarrow_1, \downarrow_2, \cdots \downarrow_9\rangle$. It was then transported to zone X for separation into two groups in zones A and B. A variable offset potential V_{O2} applied to electrode O2 imposed a bias electric field in zone X that shifted the center of the ion chain relative to the separation

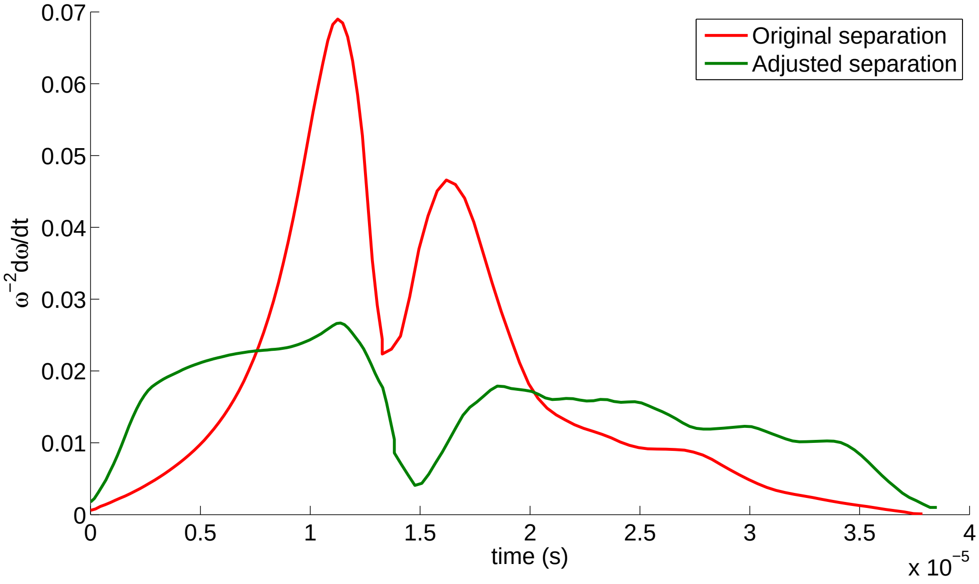

Figure 6.6: Calculations of $\frac{1}{\omega^2}\frac{d\omega}{dt}$ during the separation waveform. The original separation waveform corresponds to simulations producing a waveform where the potentials for the first segment were ramped with $\sin^2(\pi t/2T)$ for duration T between initial and final values, and the second segment linearly ramped the potential on electrode X to the final value. We imposed a maximum value of $\frac{1}{\omega^2}\frac{d\omega}{dt} = 0.025$ for the COM mode during the ramp-down of the harmonic well and $\frac{1}{\omega^2}\frac{d\omega}{dt} = 0.015$ around the sign change of $a(t)$ to produced the adjusted separation waveform. The local minimum in $\frac{1}{\omega^2}\frac{d\omega}{dt}$ during the waveform corresponds to a hand-off between the two waveform segments, which in practice takes several microseconds.

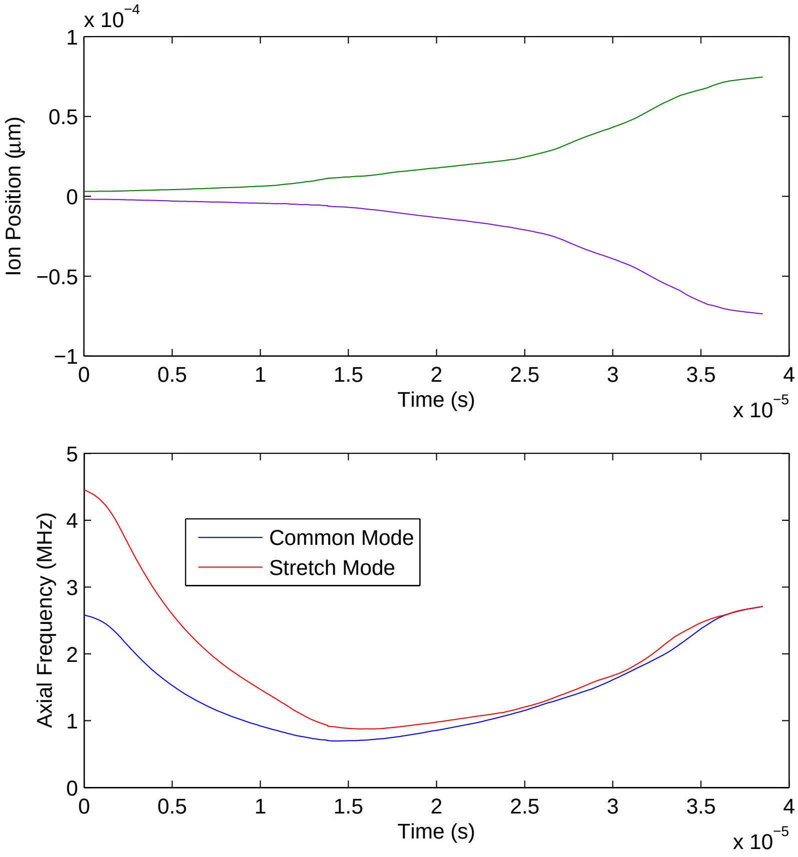

Figure 6.7: Change in ion position and normal mode frequency during separation for the two ions and the two normal modes. The normal mode frequencies converge as the ions are split into separate wells.

wedge to control the number of ions in each group. Ions in zone A were detected with resonance fluorescence, with the average photon counts approximately proportional to ion number. Following detection, all ions were recombined and transported to zone A where the total number of ions was rechecked to ascertain that no ions were lost during the waveform. As shown in Fig.6.8, increasing V_{O2} led to increased ion numbers in zone A. By adjusting V_{O2} to the center of a certain step, we could reliably partition the ions into two groups of predetermined number.

In a second experiment, two ^{9}Be$^+$ ions were initialized over zone X, whose center is defined as $z = 0$ relative to Eq.(6.4.1), which were initialized to $\bar{n} \simeq 0.1$ on both the COM and stretch modes with an initial well frequency of $\omega/(2\pi) \simeq$ 2.6 MHz ({$V_{O1}, V_A, V_X, V_B, V_{O2}$} = {2.433, -0.3763, -1.7089, -0.3831, 2.473} V) and optically pumped to $|\downarrow_1\downarrow_2\rangle$. Near the point of ion separation, simulation predicted that the minimum COM mode frequency was $\simeq$700 kHz, the minimum stretch mode frequency was $\simeq$880 kHz, and the inter-ion distance was $\sim 17\mu$m. The ions were separated into one ion in zone A and one ion in zone B, separated by $\sim 130\mu$m. The final motional frequencies were 2.85 MHz and 2.77 MHz respectively, for {$V_{O1}, ...V_{O2}$} = {4.441, -5.252, -0.649, -5.411, 5.952} V, with the total waveform duration of 55 μs. After separation, qubit MAS transitions of varying duration t were driven on either the ion in zone A or B followed by recombination in zone A where $P_\downarrow(t)$ was determined through state-dependent resonance fluorescence for each ion (Eq. 6.3.1). The first separation segment took $17\mu s$, during which it was necessary to ramp V_{O2} from 2.473 to 5.952 V to compensate for trap-geometry asymmetries and to keep the chain centered over the separation electrode, with the final value set by minimizing $\bar{n}$ for both ions.

In practice, the potential in Eq. 6.4.1 may have odd-order terms due to trap imperfections, leading to asymmetry during the separation process. During the second segment, we applied a constant relative difference between electrodes A and B to compensate for a “tilt” in the potential and to make the potential well as symmetric as possible about electrode X. We also obtained best results by applying a variable offset to the waveform potential to electrode X to tune the quartic component $b(t)$ in the potential. These parameters enabled a fine-tune balancing of the final excitation between the two ions. Experimentally, we found that near-equal excitations to both ions in their respective

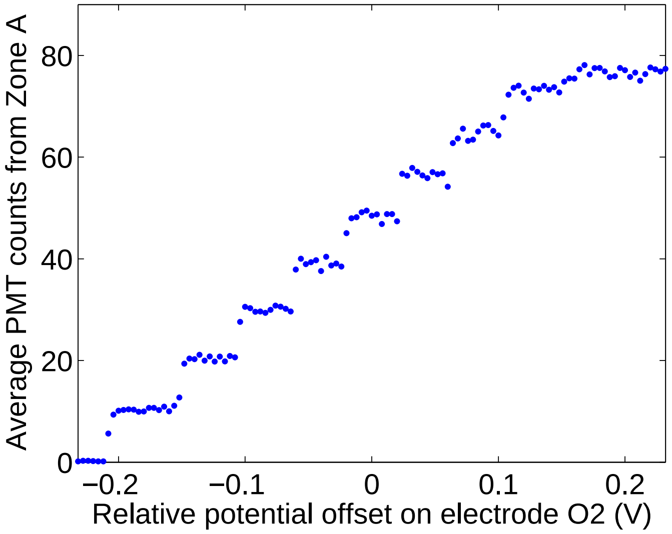

Figure 6.8: Ion fluorescence in zone A as a function of the offset potential on electrode O2 during separation relative to a central value. Each step increase of the fluorescence corresponds to the presence of an additional ion in zone A after separation. Fluorescence of a single ion led to approximately 10 average photomultiplier tube (PMT) counts in a 200 μs detection time, but as more ions were added in zone A the crystal was no longer uniformly illuminated by the detection beam and the total fluorescence dropped below 10 counts per ion. Reproduced from Ref.[66].

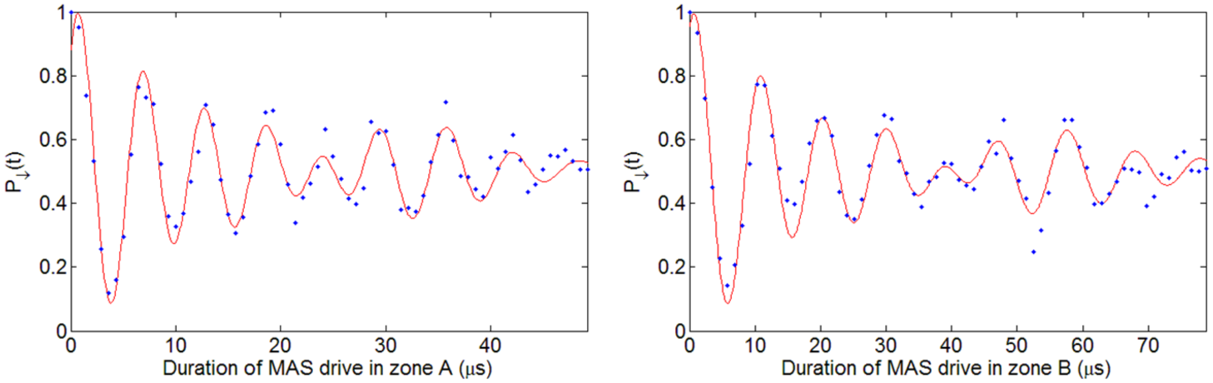

Figure 6.9: Rabi flopping trace of the MAS of the ion in zone A and zone B after separation. The fit to the MAS drive in zone B is to a coherent state with $\bar{n} = 1.9 \pm 0.1$, and $|\alpha| = 1.38 \pm 0.04$ ($\eta = 0.404$). The trace for the ion in zone A looks very similar giving $\bar{n} = 2.1 \pm 0.1$, or $|\alpha| = 1.45 \pm 0.03$ ($\eta = 0.399$).

final zones gave the lowest total excitation to both ions.

After separation, fits to MAS transitions were consistent with coherent states of $\bar{n} = 2.1 \pm 0.1$ in zone A and $\bar{n} = 1.9 \pm 0.1$ in zone B (Fig.6.9). With RF de-excitation of each ion, we could reduce $\bar{n}$ to 1.4 ± 0.1 and 1.6 ± 0.1 in zones A and B respectively, consistent with thermal distributions. The reductions indicated partial coherence in the final states, but the residual excitations could not be explained by ambient heating. Simulations of heating using measured values of heating vs. ω for a single ion only accounts for $\Delta\bar{n} \approx 0.2$. The fact that we couldn't reduce $\bar{n}$ further could be explained if the phase of the coherent states changed significantly from experiment to experiment. For example, for a change in V_{O2} of + 3 mV to shift the ions towards zone A, the motion of the ion in zone A had $\bar{n} \simeq 1.14 \pm 0.07$ while the ion in zone B had $\bar{n} > 15$, which after an RF de-excitation left the ion in zone B in a motional state consistent with a thermal distribution having $\bar{n} = 3.8 \pm 0.5$. With the additional bias field, the ion in zone B is closer to the maximum of the wedge during separation and so it would be expected to gain more kinetic energy as it falls towards the center of its respective well. Following the results in Ref. [66], it was reported in Ref. [89] that separation was achieved in 80 μs with $\bar{n} \sim 4$ quanta on each ion with similar procedures to that described here.

Chapter 7

Optimization of Multi-species Ion Transport via Feedback on Quantum Motion

For quantum information processing (QIP) based on trapped ions [5, 6], a large-scale processor might be achieved with an array of inter-connected trap zones where quantum information is transported by moving trapped ions between zones [7, 62]. Ion transport can be achieved by applying time-varying potentials, or "waveforms", to segmented trap electrodes. This multizone ion transport approach to QIP was demonstrated with a mixed-species linear chain of ions along the trap axis, where the ions were separated into two ^{9}Be$^+$-^{24}Mg$^+$ pairs (a ^{9}Be$^+$ "qubit" ion and a ^{24}Mg$^+$ "coolant" ion) accompanied by motional excitation that could be removed with sympathetic laser cooling to cool all of the normal modes of the axial motion [29, 27]. However, separation, transport, and laser cooling accounted for durations $\sim$100 times longer than for quantum logic gates. For harmonic traps, it's only necessary to cool the center-of-mass (COM) normal mode of motion for same-species chains of ions. Rapid ion transport with mitigated motional excitation was demonstrated in Refs. [90, 66] for same-species ions, but due to motional excitations from stray or fluctuating electric fields [24], it may still be necessary to implement sympathetic laser cooling. Thus, we must consider rapid ion transport for a qubit- and coolant-ion pair which mitigates excitations in all normal modes of motion.

In the work here, ions are confined in a multizone linear Paul trap, with the confinement along the trap axis characterized by an angular frequency ω. The transport waveforms are determined by simulations of the potentials from individual electrodes that form a segmented trap array, the results of which are linearly superposed. The waveforms are designed to transport ions along the trap axis while holding ω constant, and they are generated by electronics with an update rate of 50 MHz, which is much higher than the confining frequencies [74]. Unlike the case for rapid transport of a same-species ion chain as in Refs. [90, 66], different-species ions in a linear chain will experience different accelerations along the trap axis due to the unequal mass and thus non-COM modes of motion may be excited. Additionally, the transverse confinement depends inversely on the ion mass such that stray fields, those which can be difficult or impractical to simulate due to effects which may include electrode charging or electrode-geometry imperfections, can "twist" a two-species ion chain along directions which contain components of both transverse and axial motion and in turn can cause coupling between axial and transverse motion. Excitations in the transverse motion also have nonlinear couplings to the axial motion [91]. To compensate for excitations during transport, we produced a gradient-method algorithm to adjust compensating fields in our ion trap electrodes to experimentally feedback on the quantum motion of the qubit ion. We have observed that during rapid transport, axial motion can be highly excited beyond what we theoretically predict, and that this is due primarily to traversing stray fields that cause significant diabatic excitations of the transverse motion.

We investigated the dynamics of multiple ion species during transport between spatially distinct locations in multizone linear Paul traps. To account for imperfections in the transport, we implemented a gradient-method algorithm with feedback on the quantum motion of the ions using control parameters comprising trap-electrode potentials. This technique was implemented in two separate traps. A ^{9}Be^{+} and ^{24}Mg^{+} ion pair in a harmonic well was transported 370 μm within 32 μs with a peak velocity of ~ 26 m/s with an average gain of 0.2 motional quanta. A ^{9}Be^{+} and ^{25}Mg^{+} ion pair in a harmonic well was transported 340 μm within 18 μs with a peak velocity of ~ 42 m/s with an average gain of 0.1 motional quanta. This optimization method facilitates fast transport of multiple ion species that can significantly reduce the time overhead in certain architectures for scalable quantum information processing with trapped ions.

7.1 Methods for Optimizing Two-Species Transport

The qubit is formed from two 2s^{2}S$_{1/2}$ electronic ground-state hyperfine levels of $^9\mathrm{Be}^+$ $|F = 2, m_F = 1\rangle \equiv |\downarrow\rangle$ and $|F = 1, m_F = 0\rangle \equiv |\uparrow\rangle$, separated in frequency by $\omega_0/(2\pi) \simeq$ 1.2 GHz, where F and m_F are the ion's total angular momentum and its projection along the quantization magnetic field axis ($B \simeq 11.9$ mT). Ion motional quantum states can be described in the number basis $|n\rangle$ with energy $\hbar\omega(n+\frac{1}{2})$. To characterize the motional states experimentally, we use two laser beams which can be detuned from each other by $\omega_0+\omega$ or $\omega_0-\omega$ to drive motion adding sideband (MAS) spin-flip transitions $|\downarrow, n\rangle \rightarrow |\uparrow, n+1\rangle$ or motion subtracting sideband (MSS) transitions $|\downarrow, n\rangle \rightarrow |\uparrow, n-1\rangle$ on the axial normal mode of frequency ω via stimulated-Raman transitions. Since the corresponding Rabi rates are n-dependent, the populations of number states can be determined from the probability $P_\downarrow(t)$ of the state $|\downarrow\rangle$ as a function of drive time t, derived from state-dependent resonance fluorescence [57]. Due to the presence of more than one mode of motion for a ^{9}Be$^+$-^{24}Mg$^+$ ion chain, the probability $P_\downarrow(t)$ depends on both motional modes. We fit to the function

$$P_\downarrow(t) = \frac{1}{2}(1+e^{-\gamma t}\sum_{n=0}^{\infty}\sum_{m=0}^{\infty} P_n P_m \cos[2\Omega t|\langle m,n'|e^{i\eta_m(a_m+a_m^\dagger)}e^{i\eta_n(a_n+a_n^\dagger)}|m,n\rangle|]) \tag{7.1.1}$$

where number states $|n\rangle$ and $|m\rangle$ are for the two normal modes of motion with respective populations P_n and P_m, and γ is a phenomenological decay rate. This is the same as the equation in Chapter 3 Eq. 3.4.4, but with a phenomenological decay rate γ. In this case the mode with states $|n\rangle$ is driven as $n' = n+1$ for the MAS, $n' = n-1$ for the MSS, or $n' = n$ for a carrier transition, while the mode with states $|m\rangle$ is a "spectator" mode. The matrix elements $|\langle n'|e^{i\eta(a+a^\dagger)}|n\rangle|$ are given by

$$|\langle n'|e^{i\eta(a+a^\dagger)}|n\rangle| = e^{-\eta^2/2}(n_<!/n_>!)^{1/2}\eta^{|n'-n|}L_{n_<}^{|n'-n|}(\eta^2) \tag{7.1.2}$$

for each normal mode [6]. The populations of the number states for both normal modes can be determined by $P_\downarrow(t)$. For a two-ion chain, the two axial modes are the in-phase ($INPH$) and out-of-phase ($OOPH$) modes.

Our initial transport ansatz for the position profile is the error function, defined as erf$(t) = \frac{2}{\sqrt{\pi}}\int_0^t e^{-t'}\mathrm{d}t'$, to perform rapid transport that remains adiabatic with the respect to trap motion [79], though other possible functions which allow potentially faster adiabatic transport were investigated in Ref. [85] for a multi-species ion chain. The functional form we used for the position along the trap axis is given by

$$z(t) = (z_f - z_i)\frac{1+\text{erf}(4[t-t_T/2]/t_T)}{2} + z_i, \tag{7.1.3}$$

where z_i is the trap's initial position, z_f is the trap's final position, and t_T the total duration of the transport. The function is truncated at $t = 0$ and at $t = t_T$, though the trap potentials for the transport waveform with the position profile in Eq. 7.1.3 were constrained to match the trap position and velocity at the initial and final positions with cubic spline interpolation. As a baseline, a single ^{9}Be$^+$ had been transported with a waveform that transports the ion according to Eq. 7.1.3 with $\Delta\bar{n} \simeq 0.1$ for transport durations as low as $t_T \simeq 11\,\mu$s. However, when the waveform transported a two-species chain of ions according to Eq. 7.1.3, $\bar{n}_{OOPH}$ and $\bar{n}_{INPH}$ could be observed to incur as much as $\Delta\bar{n} \sim 10$ of excitation after transport.

To optimize the transport, the transport waveform was designed to move the ions with the position profile in Eq. 7.1.3, and the waveform was divided into discrete segments of evenly-spaced waveform durations for a total of N_{seg} segments, and each segment was sequentially optimized. The ions were transported across the distance up to the current segment's final position in a one-way transport, and then the transport was reversed to return the ions to the initial position in a round-trip transport. A carrier transition was then driven for a fixed drive duration set to the carrier π-time from Eq. 7.1.1 for the case when $\bar{n}_{INPH} = 0$ and $\bar{n}_{OOPH} = 0$, followed by resonance fluorescence to make a measurement that indicates the $|n_{INPH}\rangle = 0$ and $|n_{OOPH}\rangle = 0$ occupations. A basis-set of field-control parameters are independently varied for the current segment to feedback on the axial excitations, and after the results that minimize axial excitations for each parameter were found, they were then all applied to the current waveform segment. This procedure is iterated as needed for N_{it}

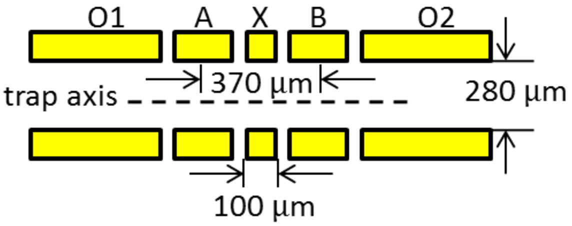

Figure 7.1: Schematic of the quantum logic trap structure showing the two diagonally opposite segmented DC electrodes (not to scale). The ions are initialized in zone A, and the transport waveform carries ions across 370 μm from zone A to zone B. Trap radio-frequency electrodes (not shown) are referenced to a common ground potential.

iterations for each segment, after which the next segment is concatenated and then optimized in the same fashion. This produces time-varying compensation fields across the entire transport that minimize axial excitations.

7.2 Transport of a Two-Species Ion Chain Experiments and Results

Our first implementation of the algorithm transported the ions in the quantum logic trap across a distance of 370 μm, the distance from zone A to zone B shown in Fig. 7.1, and t_T=32 μs with a peak velocity of ~ 26 m/s. Simulations calculate that during transport, each mode has a numerically estimated maximum coherent state displacement $|\alpha_{INPH}| \sim 0.53$ and $|\alpha_{OOPH}| \sim 0.04$ before returning to the ground state at the transport destination. Initially, a ^{9}Be$^+$-^{24}Mg$^+$ ion chain was prepared in zone A with electrode voltages {V$_{O1}$, V$_A$, V$_X$, V$_B$, V$_{O2}$}={2.433, 0.593, 4.124, 0.584, 2.473} V and Doppler cooled simultaneously with both Doppler cooling on ^{9}Be$^+$ and Doppler cooling on ^{24}Mg$^+$ for a 500 μs duration, which prepares transverse and axial motion in a thermal state [40, 36]; see Table 7.1 for the normal modes and Doppler-cooling limits. Modes with a larger amplitude for ^{24}Mg$^+$ are more efficiently cooled with the ^{24}Mg$^+$ Doppler cooling light, while modes with a larger amplitude for ^{9}Be$^+$ are more efficiently cooled with the ^{9}Be$^+$ Doppler cooling light. After Doppler cooling, the axial motion was Raman sideband laser-cooled to $\bar{n}_{INPH} \simeq 0.1$ and $\bar{n}_{OOPH} \simeq 0.1$ and the ^{9}Be$^+$ qubit ion was optically pumped to $|\downarrow\rangle$ before transport.

$\omega/2\pi$ (MHz)	$\hat{x}_{\text{Be}}$	$\hat{y}_{\text{Be}}$	$\hat{z}_{\text{Be}}$	$\hat{x}_{\text{Mg}}$	$\hat{y}_{\text{Mg}}$	$\hat{z}_{\text{Mg}}$	$\bar{n}_{limit}$
12.113	0.9998	0	0	0.0177	0	0	0.55
11.029	0	0.9997	0	0	0.0203	0	0.63
4.673	-0.0177	0	0	0.9998	0	0	4.78
4.035	0	0	-0.9258	0	0	0.3780	1.58
3.524	0	-0.0203	0	0	0.9997	0	6.49
1.902	0	0	0.3780	0	0	0.9258	8.67

Table 7.1: The normal modes for a ^{9}Be$^+$-^{24}Mg$^+$ chain with mass-weighted coordinates and the Doppler cooling limits $\bar{n}_{limit}$ for each mode. The x and y coordinates are those for the transverse motion and the z coordinate is that for the axial motion. Doppler cooling light lies along the direction $\hat{k} = \frac{\hat{x}+\hat{y}+\sqrt{2}\hat{z}}{2}$. The cooling limits are from Doppler-cooling light with both ^{24}Mg$^+$, which cools on a transition with linewidth $\Gamma \simeq 2\pi\times$41 MHz and is used to calculate $\bar{n}_{limit}$ for modes with a larger amplitude for ^{24}Mg$^+$, and Doppler cooling on ^{9}Be$^+$ which cools on a transition with linewidth $\Gamma \simeq 2\pi\times$19 MHz and is used to calculate $\bar{n}_{limit}$ for modes with a larger ampitude for ^{9}Be$^+$.

The waveform is designed with time-varying common voltages to diagonally-opposite electrodes. To optimize the transport, we used four field-control parameters, three of which were potentials generated by applying a differential "shim" voltage onto the diagonally-opposite electrode pairs A, X, and B in Fig. 7.1, given by $+V$ and $-V$ where V was varied over the range [-50,50] mV; the last parameter was from a bias voltage applied to a planar "biasboard" electrode 400 μm beneath the linear array electrode structure, varied over the range [-200,200] mV. After the optimization had completed, the ions were transported to zone B and a MAS sideband transition was driven, followed by transport back to zone A to determine $P_{\downarrow}(t)$ to ascertain the success of the algorithm. Acousto-optic deflectors (AODs) directed the laser beams to either zone A or B. The optimization algorithm was ran with $N_{seg} = 6$ and $N_{it} = 3$, which optimized to minimal final excitations of $\bar{n}_{INPH} = 0.27 \pm 0.03$ and $\bar{n}_{OOPH} = 0.31 \pm 0.04$ consistent with thermal distributions from fits to the MAS on the $INPH$ and $OOPH$ modes, respectively (Fig. 7.2). For comparison, a fit to a coherent state for either mode gives $\bar{n}_{INPH} = 0.22 \pm 0.02$ and $\bar{n}_{OOPH} = 0.23 \pm 0.02$, which are roughly the same for the results to the thermal fits.

Our second implementation of the algorithm transported the ions in the X-junction trap across a distance of 340 μm, the distance from zone A to zone B with respect to Fig. 7.3, and t_T=18 μs with a peak velocity of ~ 42 m/s. Simulations calculate that during transport, each mode has a maximum coherent state displacement $|\alpha_{INPH}| \sim 1.03$ and $|\alpha_{OOPH}| \sim 0.08$ before returning to the ground state at the transport destination. Initially, a ^{9}Be^{+}-^{25}Mg^{+} ion chain was prepared in zone A with electrode voltages {V_{O1}, V_A, V_X, V_B, V_{O2}}={1.379, -2.867, 0.639, 0.678, 0.124} V and the chain was Doppler cooled on ^{9}Be^{+} and ^{25}Mg^{+} for a 500 μs duration; see Table 7.2 for the normal modes and Doppler-cooling limits. Modes with a larger amplitude for ^{25}Mg^{+} are more efficiently cooled with the ^{25}Mg^{+} Doppler cooling light, while modes with a larger amplitude for ^{9}Be^{+} are more efficiently cooled with the ^{9}Be^{+} Doppler cooling light. After Doppler cooling, the axial motion was Raman sideband laser-cooled to $\bar{n}_{INPH} \simeq 0.1$ and $\bar{n}_{OOPH} \simeq 0.01$ and the ^{9}Be^{+} qubit ion was optically pumped to $|\downarrow\rangle$ before transport.

Four field-control parameters were used: shims applied to the diagonally-opposite electrode

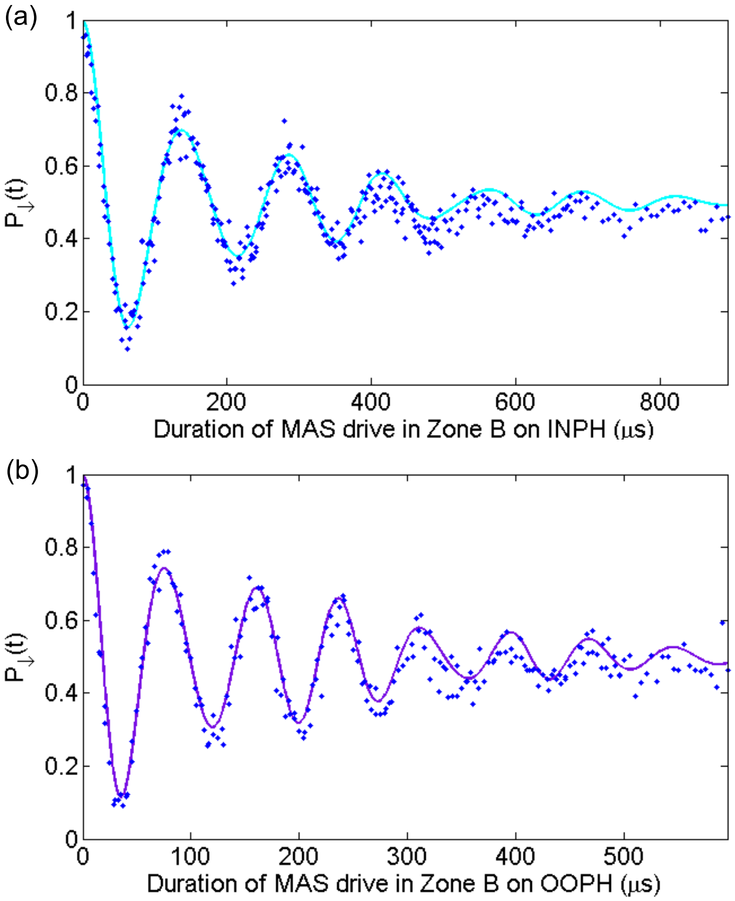

Figure 7.2: Rabi flopping traces on the MAS for each normal mode along the transport axis for transport from zone A to zone B following the optimization procedure. We fit to thermal distributions that are consistent with $\bar{n}_{INPH} = 0.27 \pm 0.03$ and $\bar{n}_{OOPH} = 0.31 \pm 0.04$. (a) Rabi flopping trace on the MAS for the $INPH$ mode with Lamb-Dicke parameter $\eta_{INPH} = 0.184$. (b) Rabi flopping trace on the MAS for the $OOPH$ mode with Lamb-Dicke parameter $\eta_{OOPH} = 0.310$.

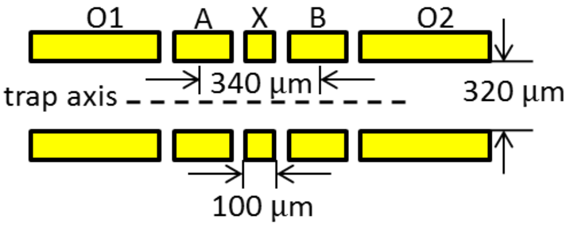

Figure 7.3: Schematic of the X-junction trap structure showing the two diagonally opposite segmented DC electrodes (not to scale). The ions are initialized in zone A, and the transport waveform carries ions across 340 μm from zone A to zone B. Trap radio-frequency electrodes (not shown) are referenced to a common ground potential.

$\omega/2\pi$ (MHz)	$\hat{x}_{\mathrm{Be}}$	$\hat{y}_{\mathrm{Be}}$	$\hat{z}_{\mathrm{Be}}$	$\hat{x}_{\mathrm{Mg}}$	$\hat{y}_{\mathrm{Mg}}$	$\hat{z}_{\mathrm{Mg}}$	$\bar{n}_{limit}$
13.091	0.9997	0	0	0.0261	0	0	0.48
11.560	0	0.9995	0	0	0.0312	0	0.59
5.364	0	0	-0.9299	0	0	0.3677	1.09
4.846	-0.0261	0	0	0.9997	0	0	4.59
3.142	0	-0.0312	0	0	0.9995	0	7.34
2.492	0	0	0.3677	0	0	0.9299	6.50

Table 7.2: The normal modes for a ^{9}Be^{+}-^{25}Mg^{+} chain with mass-weighted coordinates and the Doppler cooling limits $\bar{n}_{limit}$ for each mode. The x and y coordinates are those for the transverse motion and the z coordinate is that for the axial motion. Doppler cooling light lies along the direction $\hat{k} = \frac{\hat{x}+\hat{y}+\sqrt{2}\hat{z}}{2}$. The cooling limits are from Doppler-cooling light with both ^{25}Mg^{+}, which cools on a transition with linewidth $\Gamma \simeq 2\pi\times41$ MHz and is used to calculate $\bar{n}_{limit}$ for modes with a larger amplitude for ^{25}Mg^{+}, and Doppler cooling on ^{9}Be^{+} which cools on a transition with linewidth $\Gamma \simeq 2\pi\times19$ MHz and is used to calculate $\bar{n}_{limit}$ for modes with a larger ampitude for ^{9}Be^{+}.

pairs A, X, and B in Fig. 7.3, given by $+V$ and $-V$, where V was varied over the range [-30,30] mV, and a bias voltage applied to a planar electrode 500 μm beneath the linear array electrode structure varied over the range [-1,1] V. In this case, optical access to zone B was not possible, so following one-way transport, the transport was reversed by a highly-adiabatic return to zone A with t_T=60 μs with a peak velocity of ~ 13 m/s, where simulations calculate that during transport, the maximum coherent displacements are $|\alpha_{INPH}| \sim 0.09$ and $|\alpha_{OOPH}| \sim 0.007$. After round-trip transport, a MAS sideband transition was driven followed by detection to determine $P_{\downarrow}(t)$. In this experiment, two 2s^{2}S$_{1/2}$ electronic ground-state hyperfine levels of $^9\mathrm{Be}^+$ $|F=2, m_F=2\rangle \equiv |\downarrow\rangle$ and $|F=1, m_F=1\rangle \equiv |\uparrow\rangle$ were used. The optimization algorithm was ran with $N_{seg}=5$ and $N_{it}=2$ to converge on suitable results, which optimized to minimal final excitations of $\bar{n}_{INPH}=0.19 \pm 0.02$ and $\bar{n}_{OOPH}=0.06 \pm 0.01$ consistent with thermal states from fits to the MAS on the $INPH$ and $OOPH$ modes, respectively (Fig. 7.4). For comparison, a fit to a coherent state for either mode gives $\bar{n}_{INPH}=0.17 \pm 0.02$ and $\bar{n}_{OOPH}=0.12 \pm 0.01$, which are roughly the same for the results to the thermal fits.

In summary, we have demonstrated adiabatic transport of a qubit- and coolant-ion chain on $\sim$20-30 μs timescales, which approach those of quantum logic gate operations. When transporting two-species ions, we observed high motional excitations that could be prevented by experimentally optimizing the transport through feedback on the quantum motion. Following the optimized transport, the motion was comparable to the initial laser-cooled state. The methods described here should be straight-forward to extend to longer chains of multi-species ions. The optimization accounts for multiple normal modes of motion, and in principle, such a transport optimization should extend to very large collections of ions or atoms.

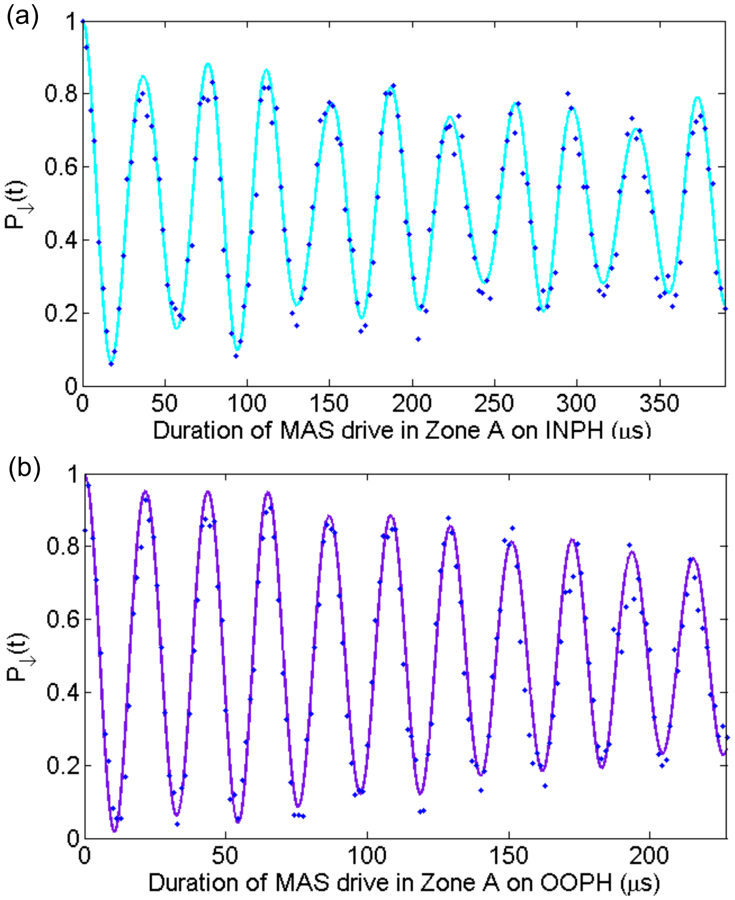

Figure 7.4: Rabi flopping traces on the MAS for each normal mode along the transport axis for transport from zone A to zone B with a highly adiabatic return to zone A following the optimization procedure. We fit to thermal distributions that are consistent with $\bar{n}_{INPH} = 0.19 \pm 0.02$ and $\bar{n}_{OOPH} = 0.06 \pm 0.01$. (a) Rabi flopping trace on the MAS for the $INPH$ mode with Lamb-Dicke parameter $\eta_{INPH} = 0.157$. (b) Rabi flopping trace on the MAS for the $OOPH$ mode with Lamb-Dicke parameter $\eta_{OOPH} = 0.270$.

Chapter 8

Conclusions and Outlook

Enormous amounts of work remain before scalable QIP with trapped ions (or any physical implementation) can be achieved. The improvements in ion transport described in this thesis should help progress towards a realization of of a multi-electrode ion-based quantum information processor. However, there are still many improvements on ion transport that remain.

Potentially, one of the biggest challenges to improve transport is to achieve ion separation with no residual excitation of ion motion. As of now, the state-of-the-art in separation has produced residual excitations on the order of 1 quantum that have proven difficult to suppress [66, 89]. A possible way to improve separation over former experiments would be to employ a feedback algorithm similar to that used for two-species ^{9}Be^{+}-^{24}Mg and ^{9}Be^{+}-^{25}Mg transport by using a set of electrode potentials to optimize the separation potential. An additional complication for separating the multi-species ^{9}Be^{+}-^{24}Mg^{+}-^{24}Mg^{+}-^{9}Be^{+} chain is that separation may require a field-compensation feedback algorithm to avoid transverse mode excitations as in the case for transport. A judicious selection of electrode parameters may be able to achieve near-ideal waveforms to mitigate excitations of axial and transverse normal modes throughout the separation process. There is a potential alternative that can avoid the need for combination and separation for each two-qubit entanglement step. By bringing ions in two separate wells sufficiently close to each other without combining into the same trap, the Coulomb interaction between ions can supply an information bus between separate wells [92, 93]. This method may circumvent the need to fully combine and separate ions in some cases.

When transporting a two-species ion crystal, we observed increasingly strong transverse excitations with increasing speeds, and this in turn made it more difficult to observe minima in excitations while optimizing the compensation fields for the waveform. Future experiments could perhaps first optimize the compensation fields and then apply the results of the field compensations to a faster waveform. There are alternative theoretical ideas for ways to move multi-species ions very rapidly and return to the ground state [85], which may lend to transport of a two-species crystal with similar low duration and excitation as those obtained in single-species transport of Refs. [66, 90]. By ground-state cooling the transverse motion before transport, there should be less overall excitation during transport. A possible way to cool the transverse motion could be to use the techniques for sympathetic electromagnetic-induced-transparency cooling with a twisted ^{9}Be$^+$-^{25}Mg$^+$ ion chain before transport [94]. Experiments for reducing the heating rates through ion-cleaning of surface traps has achieved a hundred-fold improvement in heating rates which also may reduce overall excitations during transport [25, 95].

Transporting a multi-species ion chain reliably through a junction remains an open problem. The pseudopotential near the junction differ for the two species due to different mass, which may lead to additional complications, such as requiring different waveforms for reliable transport. A possible solution to circumvent loss in the junction is to transport each ion species separately and then recombine qubit and coolant ions after transport through the junction. However, reducing the number of necessary coolant ions would alleviate some possible complications that might arise with difficulties for transporting ^{9}Be$^+$-^{25}Mg$^+$ through the RF junction. One solution to possible difficulties in transporting multiple species in the junction could be to restrict a single coolant ion to a dedicated “refrigerant” zone. When sympathetic cooling is required before an entangling gate, a coolant ion and two qubit ions would be combined to a ^{24}Mg$^+$-^{9}Be$^+$-^{9}Be$^+$ chain in a refrigerant zone, transporting the qubit ^{9}Be$^+$ ions through the junction as necessary. Asymmetry in such a crystal makes entanglement with the shared motion more desirable on a ^{9}Be$^+$-^{9}Be$^+$ chain, so following sympathetic cooling, the crystal could be separated into ^{24}Mg$^+$ and ^{9}Be$^+$-^{9}Be$^+$ to entangle the two qubit ions. In Ref. [66], it was demonstrated that it is possible to asymmetrize separation such that the motion is selectively excited in one well with less excitations in the other. Work in Ref. [22] had reliable low-excitations of the stretch mode of ^{9}Be^{+}-^{9}Be^{+} after separation of ^{9}Be^{+}-^{9}Be^{+}-^{9}Be^{+} into ^{9}Be^{+} and ^{9}Be^{+}-^{9}Be^{+}, which was the mode used for subsequent entanglement on the ^{9}Be^{+}-^{9}Be^{+} chain. Therefore, following separation into ^{24}Mg^{+} and ^{9}Be^{+}-^{9}Be, the stretch mode could be kept near the ground-state cooled motion and used for entanglement.

The ion transport experiments described in this thesis have demonstrated a high-degree of control over the motion for trapped ions during diabatic ion transport in multi-electrode ion traps. Ion transport has been demonstrated with significant speed-up in the operation times for transport, which can help reduce operation times for scalable ion-based QIP well-beneath qubit coherence times. The mitigated motional excitations alleviate the timescales for recooling before entangling gates as well. Our recent scalable QIP demonstrations had a distribution of operations which were dominated by transport and recooling, but by applying the methods described in this thesis in future QIP experiments, it is possible that the temporal distribution of tasks during an experiment could become dominated by quantum logic operations.

Bibliography

[1] R. P. Feynman, Int. J. Th. Phys. **21**, 467 (1982).

[2] S. Lloyd, Science **273**, 1073 (1996).

[3] P. W. Shor, IEEE SFCS , 124 (1994).

[4] L. K. Grover, STOC , 212 (1996).

[5] J. I. Cirac and P. Zoller, Phys. Rev. Lett. **74**, 4091 (1995).

[6] D. J. Wineland, C. Monroe, W. M. Itano, D. Leibfried, B. E. King, and D. M. Meekhof, J. Res. Natl. Inst. Stand. Technol. **103**, 259 (1998).

[7] J. I. Cirac and P. Zoller, Nature **404**, 579 (2000).

[8] D. Kielpinski, C. Monroe, and D. Wineland, Nature **417**, 709 (2002).

[9] D. Leibfried, B. DeMarco, V. Meyer, D. Lucas, M. Barrett, J. Britton, W. M. Itano, B. Jelenkovic, C. Langer, T. Rosenband, and D. J. Wineland, Nature **422**, 412 (2003).

[10] P. J. Lee, K.-A. Brickman, L. Deslauriers, P. C. Haljan, L.-M. Duan, and C. Monroe, J. Opt. B: Quantum Semiclass. Opt. **7**, S371 (2005).

[11] T. R. Tan, J. P. Gaebler, R. Bowler, Y. Lin, J. D. Jost, D. Leibfried, and D. J. Wineland, Phys. Rev. Lett. **110**, 263002 (2013).

[12] M. A. Rowe, A. Ben-Kish, B. DeMarco, D. Leibfried, V. Meyer, J. Beall, J. Britton, J. Hughes, W. M. Itano, B. Jelenković, C. Langer, T. Rosenband, and D. J. Wineland, Quantum Information and Computation **2**, 257 (2002).

[13] W. K. Hensinger, S. Olmschenk, D. Stick, D. Hucul, M. Yeo, M. Acton, L. Deslauriers, C. Monroe, and J. Rabchuk, Appl. Phys. Lett. **88**, 034101 (2006).

[14] J. Jost, Entangled Mechanical Oscillators, Ph.D. thesis, Department of Physics, University of Colorado, Boulder (2010).

[15] R. B. Blakestad, C. Ospelkaus, A. P. VanDevender, J. H. Wesenberg, M. J. Biercuk, D. Leibfried, and D. J. Wineland, Phys. Rev. A **84**, 032314 (2011).

[16] J. Chiaverini, R. B. Blakestad, J. Britton, J. D. Jost, C. Langer, D. Leibfried, R. Ozeri, and D. J. Wineland, Quantum Inf. Comput. **5**, 419 (2005).

[17] S. Seidelin, J. Chiaverini, R. Reichle, J. J. Bollinger, D. Leibfried, J. Britton, J. H. Wesenberg, R. B. Blakestad, R. J. Epstein, D. B. Hume, W. M. Itano, J. D. Jost, C. Langer, R. Ozeri, N. Shiga, and D. J. Wineland, Phys. Rev. Lett. **96**, 253003 (2006).

[18] J. M. Amini, H. Uys, J. H. Wesenberg, S. Seidelin, J. Britton, J. J. Bollinger, D. Leibfried, C. Ospelkaus, A. P. VanDevender, and D. J. Wineland, New J. Phys. **12**, 033031 (2010).

[19] D. Stick, K. M. Fortier, R. Haltli, C. Highstrete, D. L. Moehring, C. Tigges, and M. G. Blain, arXiv:1008.0990 (2010).

[20] D. T. C. Allcock, T. P. Harty, H. A. Janacek, N. M. Linke, C. J. Ballance, A. M. Steane, D. M. Lucas, R. L. Jarecki Jr., S. D. Habermehl, M. G. Blain, D. Stick, and D. L. Moehring, Applied Physics B **107**, 913 (2012).

[21] S. C. Doret, J. M. Amini, K. Wright, C. Volin, T. Killian, A. Ozakin, D. Denison, H. Hayden, C.-S. Pai, R. E. Slusher, and A. W. Harter, New J. Phys. **14**, 073012 (2012).

[22] M. D. Barrett, J. Chiaverini, T. Schätz, J. Britton, W. M. Itano, J. D. Jost, E. Knill, C. Langer, D. Leibfried, R. Ozeri, and D. J. Wineland, Nature **429**, 737 (2004).

[23] G. Huber, T. Deuschle, W. Schnitzler, R. Reichle, K. Singer, and F. Schmidt-Kaler, New J. Phys. **10**, 013004 (2008).

[24] Q. A. Turchette, D. Kielpinski, B. E. King, D. Leibfried, D. M. Meekhof, C. J. Myatt, M. A. Rowe, C. A. Sackett, C. S. Wood, W. M. Itano, C. Monroe, and D. J. Wineland, Phys. Rev. A **61**, 063418 (2000).

[25] D. A. Hite, Y. Colombe, A. C. Wilson, K. R. Brown, U. Warring, R. Jordens, J. D. Jost, K. S. McKay, D. P. Pappas, D. Leibfried, and D. J. Wineland, Phys. Rev. Lett. **109**, 103001 (2012).

[26] M. Brownnutt, M. Kumph, P. Rabl, and R. Blatt, arXiv:1409.6572 (2014).

[27] D. Hanneke, J. P. Home, J. D. Jost, J. M. Amini, D. Leibfried, and D. J. Wineland, Nature Physics **6**, 13 (2010).

[28] J. P. Gaebler, A. M. Meier, T. R. Tan, R. Bowler, Y. Lin, D. Hanneke, J. D. Jost, J. P. Home, E. Knill, D. Leibfried, and D. J. Wineland, Phys. Rev. Lett. **108**, 260503 (2012).

[29] J. P. Home, D. Hanneke, J. D. Jost, J. M. Amini, D. Leibfried, and D. J. Wineland, Science **325**, 1227 (2009).

[30] J. Chiaverini, D. Leibfried, T. Schaetz, M. D. Barrett, R. B. Blakestad, J. Britton, W. M. Itano, J. D. Jost, E. Knill, C. Langer, R. Ozeri, and D. Wineland, Nature **432**, 602 (2004).

[31] C. J. Foot, Atomic Physics (Oxford University Press, 2005).

[32] J. J. Bollinger, J. S. Wells, D. J. Wineland, and W. M. Itano, Phys. Rev. A **31**, 2711 (1985).

[33] D. J. Wineland, J. J. Bollinger, and W. M. Itano, Phys. Rev. Lett. **50**, 628 (1983).

[34] C. Langer, High fidelity quantum information processing with trapped ions, Ph.D. thesis, Department of Physics, University of Colorado, Boulder (2006).

[35] C. Langer, R. Ozeri, J. D. Jost, J. Chiaverini, B. DeMarco, A. Ben-Kish, R. B. Blakestad, J. Britton, D. B. Hume, W. M. Itano, D. Leibfried, R. Reichle, T. Rosenband, T. Schaetz, P. O. Schmidt, and D. J. Wineland, Phys. Rev. Lett. **95**, 060502 (2005).

[36] S. Stenholm, Rev. Mod. Phys. **58**, 699 (1986).

[37] D. J. Wineland, R. E. Drullinger, and F. L. Walls, Phys. Rev. Lett. **40**, 1639 (1978).

[38] W. Neuhauser, M. Hohenstatt, P. Toschek, and H. Dehmelt, Phys. Rev. Lett. **41**, 233 (1978).

[39] D. Leibfried, R. Blatt, C. Monroe, and D. Wineland, Rev. Mod. Phys. **75**, 281 (2003).

[40] W. M. Itano and D. J. Wineland, Phys. Rev. A **25**, 35 (1982).

[41] J. D. Jackson, Classical Electrodynamics (John Wiley & Sons, Inc., 1999).

[42] B. J. Dalton and P. L. Knight, J. Phys. B: At. Mol. Phys. **15**, 3997 (1982).

[43] L. Davidovich, M. Orszag, and N. Zagury, Phys. Rev. A **54**, 5118 (1996).

[44] D. J. Wineland, M. Barrett, J. Britton, J. Chiaverini, B. L. DeMarco, W. M. Itano, B. M. Jelenkovic, C. Langer, D. Leibfried, V. Meyer, T. Rosenband, and T. Schaetz, Phil. Trans. Royal Soc. London A **361**, 1349 (2003).

[45] H. G. Dehmelt, Bull. Am. Phys. Soc. **20**, 60 (1975).

[46] J. J. Bollinger, W. M. Itano, D. J. Wineland, and D. J. Heinzen, Phys. Rev. A **54**, R4649 (1996).

[47] H. Häffner, F. Schmidt-Kaler, W. Hänsel, C. F. Roos, T. Körber, M. Chwalla, M. Riebe, J. Benhelm, U. D. Rapol, C. Becher, and R. Blatt, Appl. Phys. B **81**, 151 (2005).

[48] J. Drees and W. Paul, Z. Phys. **180**, 340 (1964).

[49] P. K. Ghosh, Ion Traps (Oxford Science Publications, 1995).

[50] R. B. Blakestad, Transport of Trapped-Ion Qubits within a Scalable Quantum Processor, Ph.D. thesis, Department of Physics, University of Colorado, Boulder (2010).

[51] D. J. Berkeland, J. D. Miller, J. C. Bergquist, W. M. Itano, and D. J. Wineland, J. Appl. Phys. **83**, 5025 (1998).

[52] A. Steane, Appl. Phys. B **64**, 623 (1997).

[53] L. D. Landau and E. M. Lifshitz, Mechanics (Butterworth-Heinemann, 1976).

[54] B. King, C. Myatt, Q. Turchette, D. Leibfried, W. Itano, C. Monroe, and D. Wineland, Phys. Rev. Lett. **81**, 3631 (1998).

[55] J. D. Jost, J. P. Home, J. M. Amini, D. Hanneke, R. Ozeri, C. Langer, J. J. Bollinger, D. Leibfried, and D. J. Wineland, Nature (London) **459**, 683 (2009).

[56] J. P. Home, D. Hanneke, J. D. Jost, D. Leibfried, and D. J. Wineland, New J. Phys. **13**, 073026 (2011).

[57] D. M. Meekhof, C. Monroe, B. E. King, W. M. Itano, and D. J. Wineland, Phys. Rev. Lett. **76**, 1796 (1996), erratum Phys. Rev. Lett. 77, 2346 (1996).

[58] W. P. Schleich, Quantum Optics in Phase Space (Wiley-VCH, 2001).

[59] K. E. Cahill and R. J. Glauber, Phys. Rev. **177**, 1857 (1969).

[60] D. J. Wineland and W. M. Itano, Phys. Rev. A **20**, 1521 (1979).

[61] C. Monroe, D. M. Meekhof, B. E. King, S. R. Jefferts, W. M. Itano, D. J. Wineland, and P. Gould, Phys. Rev. Lett. **75**, 4011 (1995).

[62] D. Kielpinski, B. E. King, C. J. Myatt, C. A. Sackett, Q. A. Turchette, W. M. Itano, C. Monroe, D. J. Wineland, and W. H. Zurek, Phys. Rev. A **61**, 032310 (2000).

[63] Y. Lin, J. P. Gaebler, F. Reiter, T. R. Tan, R. Bowler, A. S. Sørensen, D. Leibfried, and D. J. Wineland, Nature **504**, 415 (2013).

[64] G. Morigi, J. Eschner, and C. H. Keitel, Phys. Rev. Lett. **85**, 4458 (2000).

[65] A. Kramida, Y. Ralchenko, and J. Reader, (2014).

[66] R. Bowler, J. Gaebler, Y. Lin, T. R. Tan, D. Hanneke, J. D. Jost, J. P. Home, D. Leibfried, and D. J. Wineland, Phys. Rev. Lett. **109**, 080502 (2012).

[67] R. B. Blakestad, C. Ospelkaus, A. P. VanDevender, J. M. Amini, J. Britton, D. Leibfried, and D. J. Wineland, Phys. Rev. Lett. **102**, 153002 (2009).

[68] P. Huang and D. Leibfried, Proc. SPIE 5524, Novel Optical Systems Design and Optimization VII **125** (2004).

[69] A. C. Wilson, C. Ospelkaus, A. P. VanDevender, J. A. Mlynek, K. R. Brown, D. Leibfried, and D. J. Wineland, Appl. Phys. B **105**, 741 (2011).

[70] G. D. Boyd and D. A. Kleinman, J. Appl. Phys. **39**, 3597 (1968).

[71] A. Steinbach, M. Rauner, F. C. Cruz, and J. C. Bergquist, Optics Comm. **123**, 207 (1996).

[72] T. W. Hansch and B. Couillaud, Optics Communications **35**, 441 (1980).

[73] Y. Colombe, D. H. Slichter, A. C. Wilson, D. Leibfried, and D. J. Wineland, Opt. Express **22**, 19783 (2014).

[74] R. Bowler, U. Warring, J. W. Britton, and J. M. Amini, Rev. Sci. Instrum. **84**, 033108 (2013).

[75] J. P. Home, private communication.

[76] C. Ospelkaus, U. Warring, Y. Colombe, K. R. Brown, J. M. Amini, D. Leibfried, and D. J. Wineland, Nature **476**, 181 (2011).

[77] J. Preskill, Proc. R. Soc. A **454**, 385 (1998).

[78] E. Knill, Nature **463**, 441 (2010), news and Views Q&A.

[79] R. Reichle, D. Leibfried, R. B. Blakestad, J. Britton, J. D. Jost, E. Knill, C. Langer, R. Ozeri, S. Seidelin, and D. J. Wineland, Fortschr. Phys. **54**, 666 (2006).

[80] S. Schulz, U. Poschinger, K. Singer, and F. Schmidt-Kaler, Fortschr. Phys. **54**, 648 (2006).

[81] J. P. Home, D. Hanneke, J. D. Jost, J. M. Amini, D. Leibfried, and D. J. Wineland, Science **325**, 1227 (2009).

[82] E. Torrontegui, S. Ibanez, X. Chen, A. Ruschhaupt, D. Guery-Odelin, and J. G. Muga, Phys. Rev. A **83**, 013415 (2011).

[83] H.-K. Lau and D. F. V. James, Phys. Rev. A **83**, 062330 (2011).

[84] A. Couvert, T. Kawalec, G. Reinaudi, and D. Guery-Odelin, Europhys. Lett. **83**, 13001 (2008).

[85] M. Palmero, R. Bowler, J. P. Gaebler, D. Leibfried, and J. G. Muga, Phys. Rev. A **90**, 053408 (2014).

[86] J. P. Home and A. M. Steane, Quantum Information and Computation **6**, 289 (2006).

[87] H. Kaufmann, T. Ruster, C. T. Schmiegelow, F. Schmidt-Kaler, and U. G. Poschinger, New J. Phys. **16**, 073012 (2014).

[88] X. Chen, A. Ruschhaupt, S. Schmidt, A. del Campo, D. Guery-Odelin, and J. G. Muga, Phys. Rev. Lett. **104**, 063002 (2010).

[89] T. Ruster, C. Warschburger, H. Kaufmann, C. T. Schmiegelow, A. Walther, M. Hettrich, A. Pfister, V. Kaushal, F. Schmidt-Kaler, and U. G. Poschinger, Phys. Rev. A **90**, 033410 (2014).

[90] A. Walther, F. Ziesel, T. Ruster, S. T. Dawkins, K. Ott, M. Hettrich, K. Singer, F. Schmidt-Kaler, and U. Poschinger, Phys. Rev. Lett. **109**, 080501 (2012).

[91] C. F. Roos, T. Monz, K. Kim, M. Riebe, H. Häffner, D. F. V. James, and R. Blatt, Phys. Rev. A **77**, 040302 (2008).

[92] K. R. Brown, C. Ospelkaus, Y. Colombe, A. C. Wilson, D. Leibfried, and D. J. Wineland, Nature **471**, 197 (2011).

[93] A. Wilson, Y. Colombe, K. R. Brown, E. Knill, D. Leibfried, and D. Wineland, Nature **512**, 57 (2014).

[94] Y. Lin, J. P. Gaebler, T. R. Tan, R. Bowler, J. D. Jost, D. Leibfried, and D. J. Wineland, Phys. Rev. Lett. **110**, 153002 (2013).

[95] N. Daniilidis, S. Gerber, G. Bolloten, M. Ramm, A. Ransford, E. Ulin-Avila, I. Talukdar, and H. Häffner, Phys. Rev. B **89**, 245435 (2014).

[96] D. Leibfried, E. Knill, C. Ospelkaus, and D. J. Wineland, Phys. Rev. A **76**, 032324 (2007).

[97] K. Mølmer and A. Sørensen, Phys. Rev. Lett. **82**, 1835 (1999).

[98] A. Sørensen and K. Mølmer, Phys. Rev. Lett. **82**, 1971 (1999)

Appendix A

Transport Gate

A possible approach to reduce the resources required for QIP experiments with a multi-electrode trap architecture is to have dedicated regions where beams are always turned on, which alleviates issues due to duty cycle by having continuous beam position and intensity stabilization. Ions then can be transported through the beam to perform qubit rotations or entanglement without the need for switching on or off beams or redirecting beams to different zones [96]. The precise control achieved over ion transport described in this thesis allows the ion velocity to be easily set to convenient values for our laser beam parameters. This section assumes that ions travel at approximately constant velocity.

The proposal in Ref. [96] includes using the Doppler shift in the frame of the ions between two Raman beams as a detuning from a shared normal mode of motion to drive an entangling gate during adiabatic ion transport. Our desirable velocities are on the order of $v \gtrsim 10$ m/s to reduce gate durations to acceptable values. For $v = 30$ m/s and for a laser beam at an angle γ with respect to the transport axis, the Doppler shift is $\Delta\omega = |k||v|\cos(\gamma) \simeq 2\pi \times 68$ MHz, which is too large for a practical gate detuning from a ~ 5 MHz normal mode. Instead, we can achieve rapid transport with Doppler shifts that can be canceled by shifting the laser beam frequencies with AOMs and thus allow us the freedom to set an ideal detuning δ_0 in the beams and maintain a fixed angle $\gamma = \pi/4$. Typical AOMs in our lab have a bandwidth of ~ 100 MHz, allowing a sufficient range of tuning to account for relevant Doppler shifts.

For a Gaussian laser beam field, traversing a beam at constant velocity would be equivalent to a Gaussian-shaped temporal laser pulse. For a beam propagating along $\hat{z}$ and with transverse radial direction $\hat{r}$, the electric field is given by

$$E(r,t) = \frac{E_0}{2}\frac{w_0}{w(z)}\exp\left(\frac{-r^2}{w(z)^2}\right)\exp\left[-i(kz-\omega t+\phi-arctan(z/z_r)+\frac{kr^2}{2R(z)}\right]+h.c., \quad \text{(A.0.1)}$$

where the beam waist is w_0, $w(z) = w_0\sqrt{1+(z/z_r)^2}$, $R(z) = z[1+(z_r/z)^2]$, and $z_r = kw_0^2/2$. For ions near the beam's focus, such that $|z/z_r| \ll 1$, we can make the approximations that $w(z) \simeq w_0$, $arctan(z/z_r) \simeq 0$, and $kr^2/2R(z) \simeq 0$. Then, the field simplifies to

$$E(r,t) = \frac{E_0}{2}\exp\left(\frac{-r^2}{w_0^2}\right)\exp\left[-i(kz-\omega t+\phi)\right]+h.c. \quad \text{(A.0.2)}$$

For the case of single-qubit rotations, we assume that a Raman transition is driven by co-propagating laser beams (Chapter 2). The Rabi rate is proportional to the square of the electric field, and so for a maximum Rabi rate Ω_m at the center of the beam with the substitution $\tau = w_0/\sqrt{2}v\sin(\gamma)$ in Eq. A.0.2 for an ion moving with velocity v across a beam of waist w_0, the Rabi rate varies as

$$\Omega(t) = \Omega_m \exp\left[-(t/\tau)^2\right]. \quad \text{(A.0.3)}$$

The qubit rotation angle is then given by

$$\theta = \int_{-t_T}^{t_T}\Omega(t)dt = \Omega_m\tau\sqrt{\pi}\,\text{erf}\left[t_T/\tau\right] \quad \text{(A.0.4)}$$

for a transport time $2t_T$. As an example for a π-rotation, assuming that an ion has $v = 30$ m/s and traverses a beam with $w_0 = 30\mu$m at 45° to the transport axis, then $\tau = 1\mu$s. Taking the approximation $t_T \rightarrow \infty$ gives that we need a beam with $\Omega_m \simeq 2\pi \times 282$ kHz, which is typical for our systems.

Entangling two qubit ions can be achieved when traversing beams in a 90°-degree angle from each other, each 45° to the transport axis, to drive motion-sensitive transitions. This requires that the inter-ion distance is much less than twice the beam waist so that both ions have approximately the same interaction while traversing the beams. For two ^{9}Be$^+$ ions in a well with $\omega_z = 2\pi \times 3.6$ MHz, the ion distance is $d = (2k_e q^2/k_z)^{1/3} \simeq 3.92\mu$m (from Chapter 3), approximately an order of magnitude less than w_0. One gate scheme requires the ability to simultaneously drive a transition detuned from the red- and blue-sideband transitions on the qubit ions [97, 98]. This can be achieved, for example, by using an electro-optic modulator (EOM) such that the modulation due to the EOM suppresses the carrier and has two sidebands detuned from the stretch mode of motion for two ^{9}Be$^+$ ions. For the work in Ref. [28], we used two AOMs to shift the frequencies of two beams which were then combined to have co-propagating sidebands. The entangling-gate Hamiltonian is given by

$$H_I = \Omega(t)\left[(\sigma_{+1}+\sigma_{+2})\otimes a e^{-i\delta_0 t} + (\sigma_{+1}+\sigma_{+2})\otimes a^\dagger e^{i\delta_0 t}\right] + h.c. \tag{A.0.5}$$

where σ_{+i} is the usual Pauli spin operator for qubit $i = 1,2$ and δ_0 is the detuning from a normal mode. Consider the stretch mode $\omega_{stretch} = \sqrt{3}\omega_z \simeq 2\pi \times 6.2$ MHz, which would not be excited during ion transport. Nominally, there is no residual motion following the entangling gate. A state-dependent coherent state is driven by the gate, which is proportional to

$$\alpha(t) \propto \int_{-t_T}^{t_T} \exp[-(t/\tau)^2] e^{i\delta_0 t} dt, \tag{A.0.6}$$

which gives that if the Fourier transform vanishes at δ_0, then the motion and spins are disentangled after the transport. Taking the approximation that $t_T \to \infty$, and that $\alpha(-\infty) = 0$, and with the substitution $p = \delta_0\tau/2$, the coherent state evolution during the entangling gate is given by [96]

$$\alpha(t) = \frac{\sqrt{\pi}(\mathrm{erf}\,[t/\tau - ip] + 1)}{2\sqrt{\mathrm{erfi}\left[\sqrt{2}p\right]}}, \tag{A.0.7}$$

where erfi$[z] = -i$erf$[iz]$. This expression vanishes for large p. For example, if $p = 4$, then $\delta_0 \simeq 2\pi\times$1.273 MHz. With that detuning, simulations show that for $\Omega_m = 2\pi\times$250 kHz, the final entanglement error is $\varepsilon \simeq 3.13 \times 10^{-7}$, well beneath the fault-tolerant threshold of $\sim 10^{-4}$, and that $\alpha(\infty) \simeq 3.15 \times 10^{-7}$. It may also be convenient to consider performing an entangling gate with the same considerations using Gaussian-shaped laser pulses incident on stationary ions, as precision timing for starting and stopping the gate interaction is replaced with asymptotic behavior for disentangling the qubit and motion states at the end of the entagling gate.

Appendix B

AWG Spec Sheets

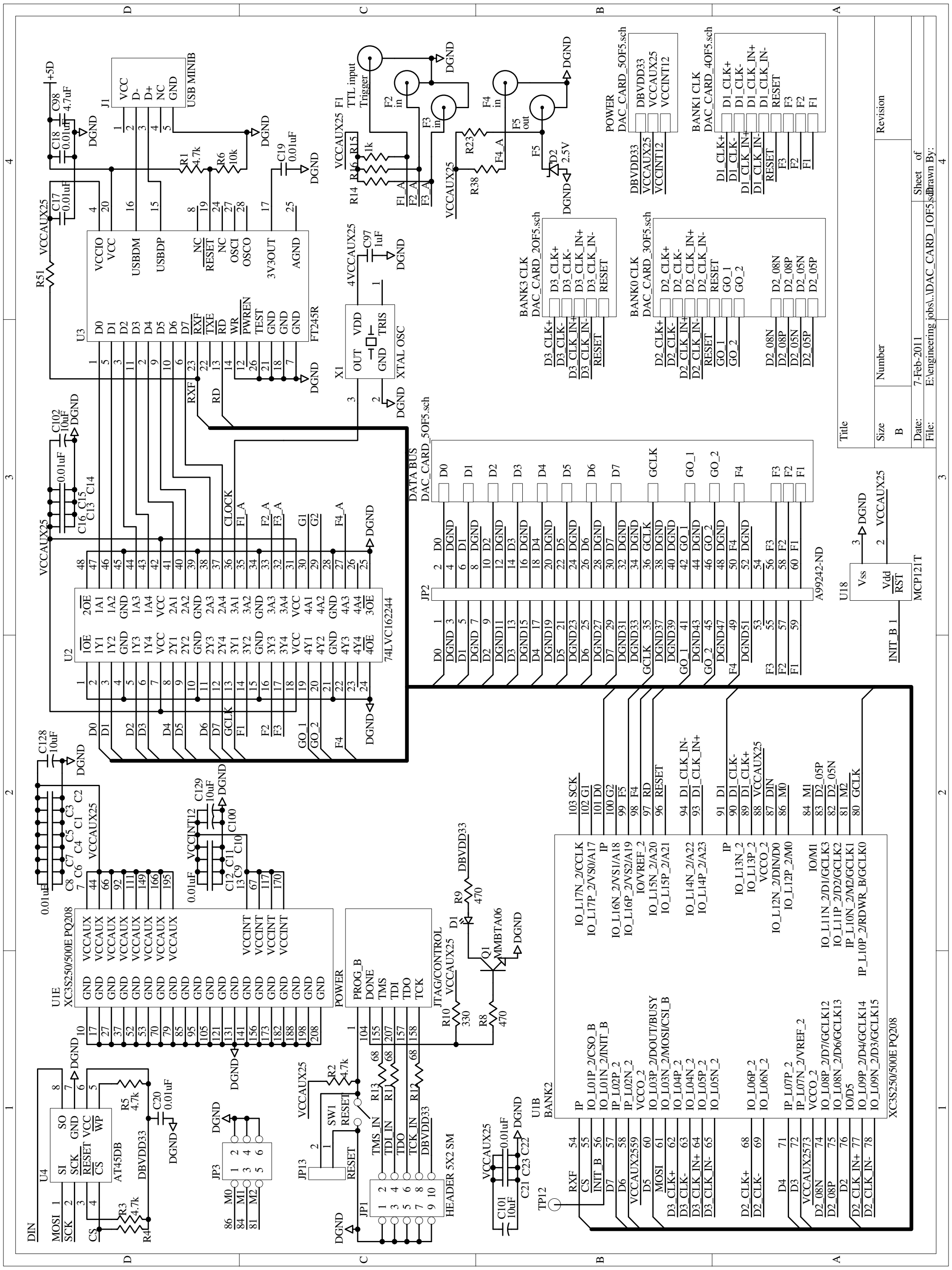
U3
FT245R
J1
USB MINIB
U2
74LVC162244
U1E
XC3S250/500E PQ208
U1B
BANK2
XC3S250/500E PQ208
U4
AT45DB
X1
XTAL OSC
JP2
A99242-ND
U18
MCP121T
JP1
HEADER 5X2 SM
JP3
JP13
SW1
RESET
TP12
Q1
MMBTA06
D1
D2
2.5V
DATA BUS
DAC_CARD_5OF5.sch
POWER
DAC_CARD_5OF5.sch
BANK1 CLK
DAC_CARD_4OF5.sch
BANK3 CLK
DAC_CARD_2OF5.sch
BANK0 CLK
DAC_CARD_3OF5.sch
JTAG/CONTROL
TTL input
Trigger
VCCAUX25
VCCINT12
DBVDD33
DGND
+5D
Title
Size
B
Number
Revision
Date: 7-Feb-2011
File: E:\engineering jobs\..\DAC_CARD_1OF5.sch
Sheet of
Drawn By:

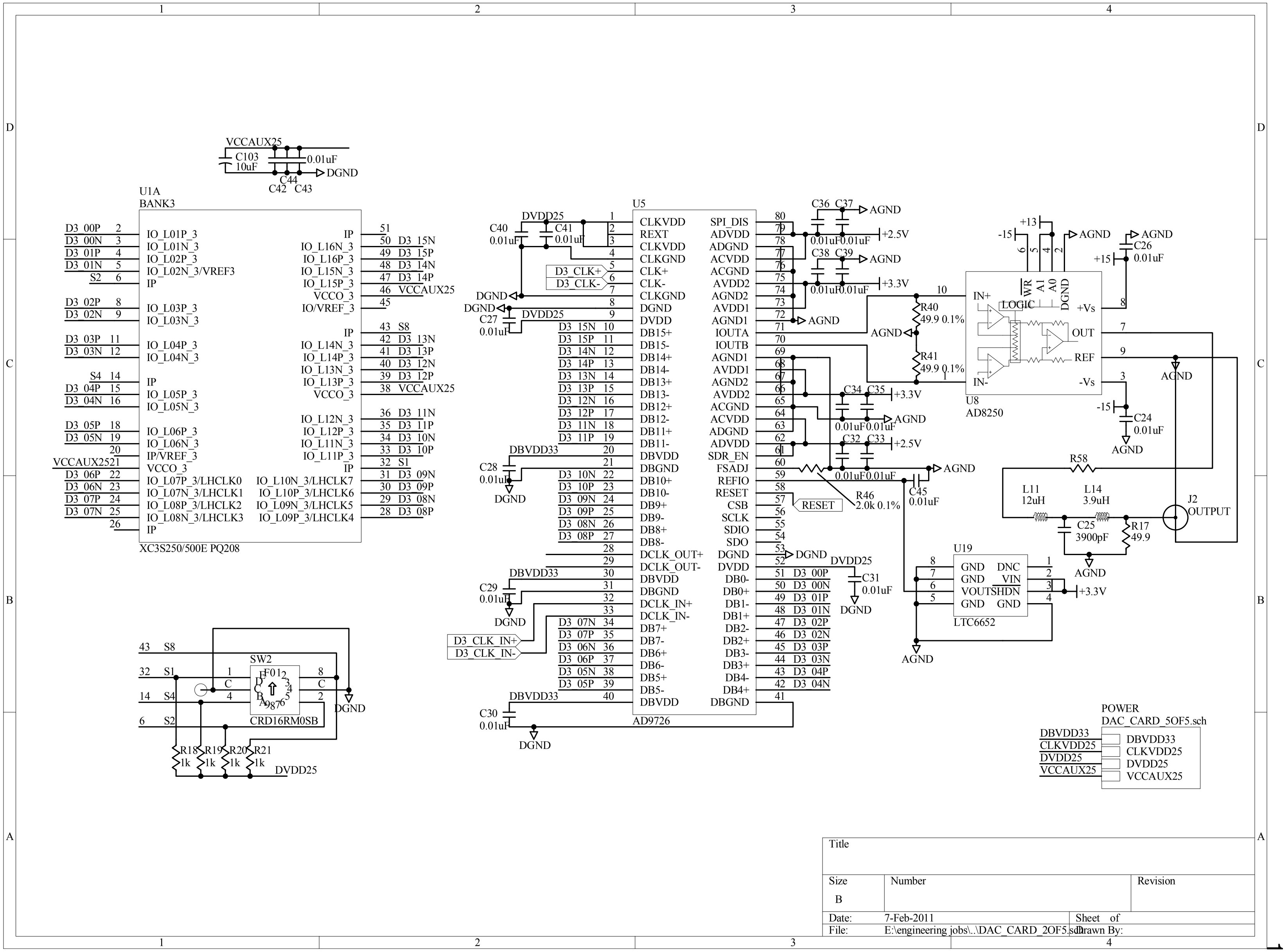
U1A
BANK3
XC3S250/500E PQ208
VCCAUX25
C103
10uF
0.01uF
C44
C42 C43
DGND
IO_L01P_3
IO_L01N_3
IO_L02P_3
IO_L02N_3/VREF3
IP
IO_L03P_3
IO_L03N_3
IO_L04P_3
IO_L04N_3
IO_L05P_3
IO_L05N_3
IO_L06P_3
IO_L06N_3
IP/VREF_3
VCCO_3
IO_L07P_3/LHCLK0
IO_L07N_3/LHCLK1
IO_L08P_3/LHCLK2
IO_L08N_3/LHCLK3
IO_L16N_3
IO_L16P_3
IO_L15N_3
IO_L15P_3
IO/VREF_3
IO_L14N_3
IO_L14P_3
IO_L13N_3
IO_L13P_3
IO_L12N_3
IO_L12P_3
IO_L11N_3
IO_L11P_3
IO_L10N_3/LHCLK7
IO_L10P_3/LHCLK6
IO_L09N_3/LHCLK5
IO_L09P_3/LHCLK4
VCCAUX2521
SW2
CRD16RM0SB
S8
S1
S4
S2
R18 1k
R19 1k
R20 1k
R21 1k
DVDD25
U5
AD9726
CLKVDD
REXT
CLKGND
CLK+
CLK-
DGND
DVDD
DB15+
DB15-
DB14+
DB14-
DB13+
DB13-
DB12+
DB12-
DB11+
DB11-
DBVDD
DBGND
DB10+
DB10-
DB9+
DB9-
DB8+
DB8-
DCLK_OUT+
DCLK_OUT-
DCLK_IN+
DCLK_IN-
DB7+
DB7-
DB6+
DB6-
DB5+
DB5-
SPI_DIS
ADVDD
ADGND
ACVDD
ACGND
AVDD2
AGND2
AVDD1
AGND1
IOUTA
IOUTB
SDR_EN
FSADJ
REFIO
RESET
CSB
SCLK
SDIO
SDO
DB0-
DB0+
DB1-
DB1+
DB2-
DB2+
DB3-
DB3+
DB4-
DB4+
D3_CLK+
D3_CLK-
D3_CLK_IN+
D3_CLK_IN-
DBVDD33
C40 0.01uF
C41 0.01uF
C27 0.01uF
C28 0.01uF
C29 0.01uF
C30 0.01uF
C31 0.01uF
C36 C37
C38 C39
C34 C35
C32 C33
C45 0.01uF
R46 2.0k 0.1%
+2.5V
+3.3V
AGND
U8
AD8250
IN+
IN-
LOGIC
WR
A1
A0
+Vs
-Vs
OUT
REF
+13
-15
+15
C26 0.01uF
C24 0.01uF
R40 49.9 0.1%
R41 49.9 0.1%
R58
L11 12uH
L14 3.9uH
C25 3900pF
R17 49.9
J2
OUTPUT
U19
LTC6652
DNC
VIN
SHDN
VOUT
GND
POWER
DAC_CARD_5OF5.sch
CLKVDD25
Title
Size
B
Number
Revision
Date: 7-Feb-2011
Sheet of
File: E:\engineering jobs\..\DAC_CARD_2OF5.sch
Drawn By:

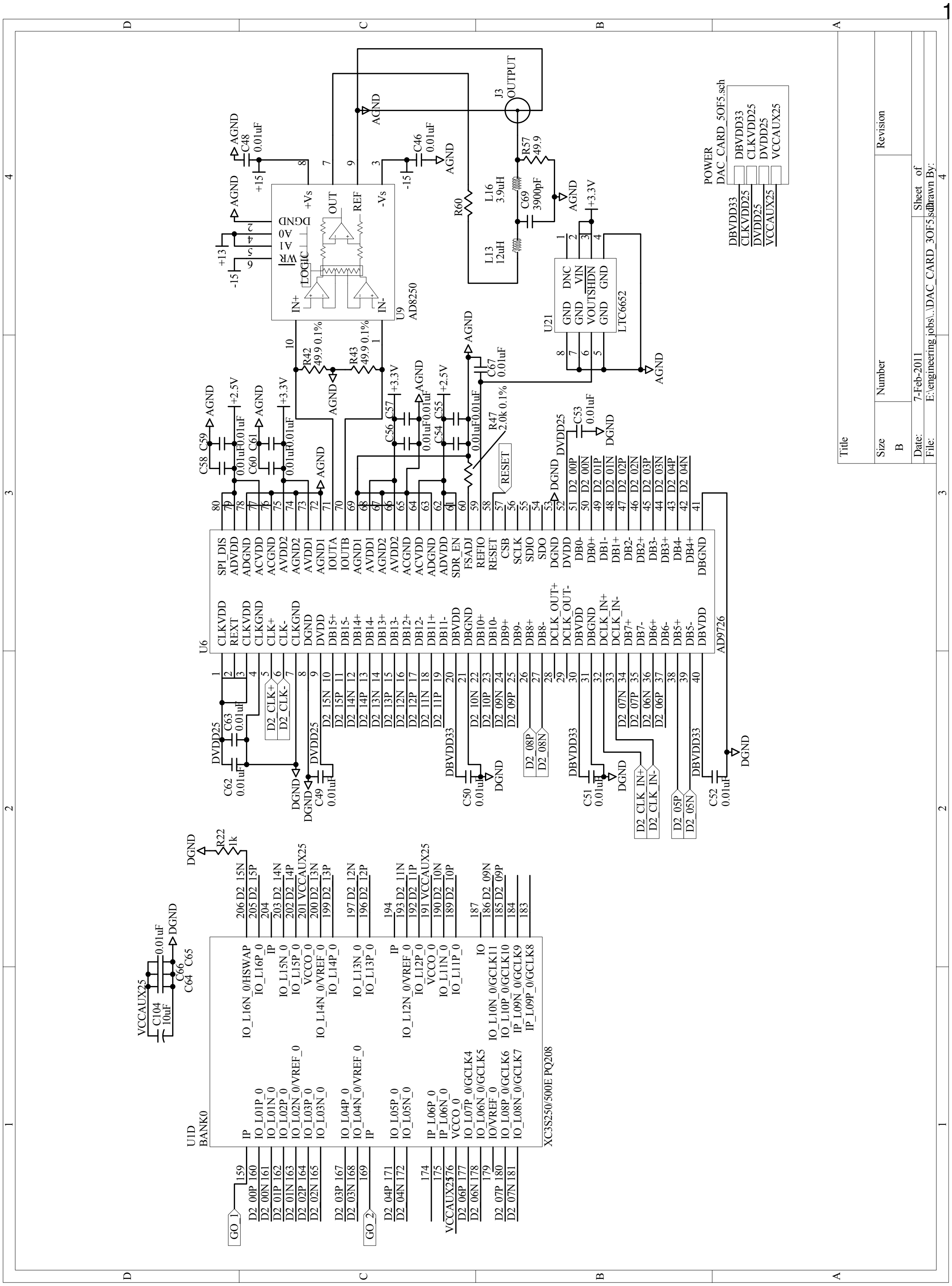
U6
AD9726
U9
AD8250
U21
LTC6652
U1D
BANK0
XC3S250/500E PQ208
J3
OUTPUT
R57
49.9
L16
3.9uH
C69
3900pF
L13
12uH
R60
R42
49.9 0.1%
R43
49.9 0.1%
R47
2.0k 0.1%
R22
1k
C48
0.01uF
C46
0.01uF
C67
0.01uF
C53
0.01uF
C62
C63
C49
C50
C51
C52
C104
10uF
C64
C65
C66
AGND
DGND
+3.3V
+2.5V
+15
-15
+13
DVDD25
DBVDD33
VCCAUX25
RESET
GO_1
GO_2
D2_CLK+
D2_CLK-
D2_CLK_IN+
D2_CLK_IN-
D2_08P
D2_08N
D2_05P
D2_05N
POWER
DAC_CARD_5OF5.sch
DBVDD33
CLKVDD25
DVDD25
VCCAUX25
Title
Size
B
Number
Revision
Date:
7-Feb-2011
Sheet of
File:
E:\engineering jobs\..\DAC_CARD_3OF5.sch
Drawn By:
A
B
C
D
1
2
3
4

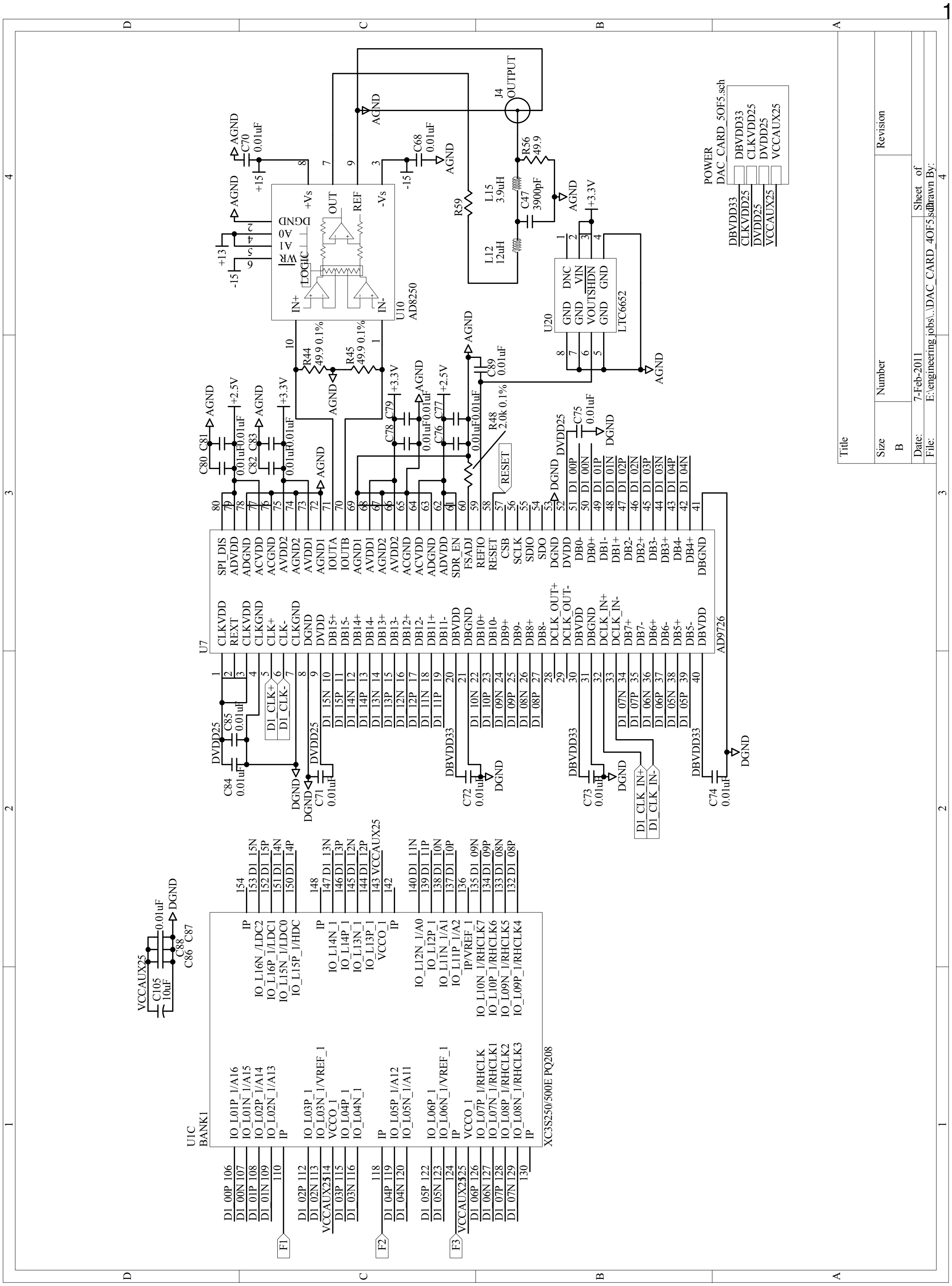
U7
AD9726
U10
AD8250
U20
LTC6652
U1C
BANK1
XC3S250/500E PQ208
J4
OUTPUT
R44
49.9 0.1%
R45
49.9 0.1%
R48
2.0k 0.1%
R56
49.9
R59
L12
12uH
L15
3.9uH
C47
3900pF
C105
10uF
0.01uF
AGND
DGND
+3.3V
+2.5V
+15
-15
+13
DVDD25
DBVDD33
VCCAUX25
RESET
D1_CLK+
D1_CLK-
D1_CLK_IN+
D1_CLK_IN-
F1
F2
F3
POWER
DAC_CARD_5OF5.sch
DBVDD33
CLKVDD25
DVDD25
VCCAUX25
Title
Size
B
Number
Revision
Date:
7-Feb-2011
Sheet of
File:
E:\engineering jobs\..\DAC_CARD_4OF5.sch
Drawn By:
A
B
C
D
1
2
3
4

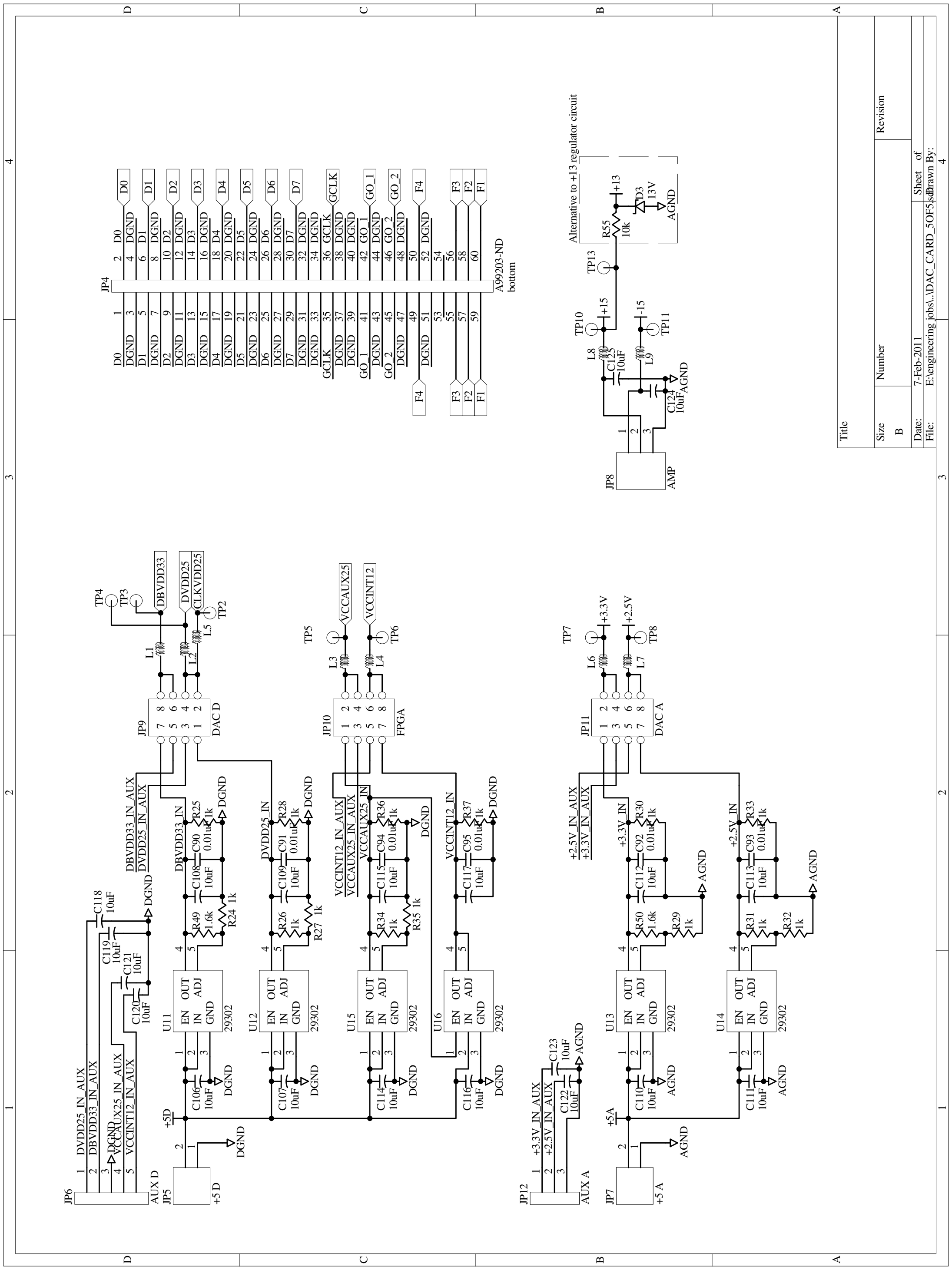
Alternative to +13 regulator circuit
JP4
A99203-ND
bottom
JP9
DAC D
JP10
FPGA
JP11
DAC A
JP8
AMP
JP5
+5 D
JP6
AUX D
JP7
+5 A
JP12
AUX A
U11
U12
U15
U16
U13
U14
29302
DVDD25_IN_AUX
DBVDD33_IN_AUX
VCCAUX25_IN_AUX
VCCINT12_IN_AUX
+3.3V_IN_AUX
+2.5V_IN_AUX
DGND
AGND
+5D
+5A
Title
Size
B
Number
Revision
Date:
7-Feb-2011
Sheet of
File:
E:\engineering jobs\..\DAC_CARD_5OF5.sch
Drawn By: